A photometric analysis of Abell 1689: two-dimensional multistructure decomposition, morphological classification and the Fundamental Plane

E. Dalla Bontà,[1,2]★ R. L. Davies,[3] R. C. W. Houghton,[3] F. D'Eugenio[4,5] and J. Méndez-Abreu[6,7,8]

[1]*Dipartimento di Fisica e Astronomia 'G. Galilei', Università degli Studi di Padova, Vicolo dell'Osservatorio 3, I-35122 Padova, Italy*
[2]*INAF Osservatorio Astronomico di Padova, Vicolo dell'Osservatorio 5, I-35122 Padova, Italy*
[3]*Physics Department, University of Oxford, Denys Wilkinson Building, Keble Road, Oxford OX1 3RH, UK*
[4]*Research School of Astronomy and Astrophysics, Australian National University, Canberra, ACT 2611, Australia*
[5]*ARC Centre of Excellence for All-Sky Astrophysics (CAASTRO)*
[6]*School of Physics and Astronomy, University of St Andrews, SUPA, North Haugh, St Andrews KY16 9SS, UK*
[7]*Instituto de Astrofísica de Canarias, E-38200 La Laguna, Tenerife, Spain*
[8]*Department Astrofísica, Universidad de La Laguna, E-38206 La Laguna, Tenerife, Spain*

ABSTRACT

We present a photometric analysis of 65 galaxies in the rich cluster Abell 1689 at $z = 0.183$, using the *Hubble Space Telescope* Advanced Camera for Surveys archive images in the rest-frame V band. We perform two-dimensional multicomponent photometric decomposition of each galaxy adopting different models of the surface-brightness distribution. We present an accurate morphological classification for each of the sample galaxies. For 50 early-type galaxies, we fit both a de Vaucouleurs law and a Sérsic law; S0s are modelled by also including a disc component described by an exponential law. Bars of SB0s are described by the profile of a Ferrers ellipsoid. For the 15 spirals, we model a Sérsic bulge, exponential disc and, when required, a Ferrers bar component. We derive the Fundamental Plane (FP) by fitting 40 early-type galaxies in the sample, using different surface-brightness distributions. We find that the tightest plane is that derived by Sérsic bulges. We find that bulges of spirals lie on the same relation. The FP is better defined by the bulges alone rather than the entire galaxies. Comparison with local samples shows both an offset and rotation in the FP of Abell 1689.

Key words: galaxies: clusters: individual: Abell 1689 – galaxies: elliptical and lenticular, cD – galaxies: fundamental parameters – galaxies: photometry – galaxies: spiral.

1 INTRODUCTION

The discovery of the Fundamental Plane (FP) three decades ago (Djorgovski & Davis 1987; Dressler et al. 1987; Faber et al. 1987) constituted an important milestone on understanding galaxy evolution. Stellar velocity dispersion, $\sigma_\star$, effective radius, r_e, and average surface brightness within r_e, $\langle I \rangle_e$, of early-type galaxies (ETGs) define a remarkably tight plane in the form $r_e \propto \sigma_\star^b \langle I \rangle_e^c$. Under the assumptions of structural homology and uniform mass-to-light ratio, the virial theorem predicts $b = 2$ and $c = -1$; because the best-fitting values of b and c deviate from this prediction, the FP is said to be 'tilted' (Burstein et al. 1997; Trujillo, Burkert & Bell 2004). The FP remains a potentially powerful tool to investigate galaxy mass assembly and luminosity evolution with redshift, by comparing the values of the FP coefficients over time. However, there is little

uniformity in the details of how the observables are measured, which makes direct comparisons difficult or inappropriate. Differences in the derived FP coefficients can be due to the algorithm used, whether the fit is direct or orthogonal, choice of the dependent variable (e.g. Sheth & Bernardi 2012), passband (e.g. Bernardi et al. 2003) and sample selection (e.g. Nigoche-Netro, Ruelas-Mayorga & Franco-Balderas 2008). In this contribution, we will focus on the photometric parameters that enter the FP and investigate whether or not possible discrepancies can arise with the change of photometric models. Indeed, originally r_e and $\langle I \rangle_e$ of galaxies were measured by fitting a de Vaucouleurs law to the growth curve (see Paper I for a description). Later on Sérsic profile to the growth curve was adopted (e.g. Caon, Capaccioli & D'Onofrio 1993; La Barbera et al. 2002). A de Vaucouleurs bulge plus exponential disc decomposition has also been used (e.g. Saglia et al. 1997; Fritz et al. 2005), as have two-dimensional surface-brightness decompositions (e.g. Simard et al. 2002; Tran et al. 2003; Fritz, Böhm & Ziegler 2009; Fernández Lorenzo et al. 2011).

★ E-mail: elena.dallabonta@unipd.it

Abell 1689 (Abell 1958) is a richness class 4 cluster at redshift $z = 0.183$ (Struble & Rood 1999). As a Coma cluster analogue, it provides an opportunity to study the evolution of galaxies in dense environments over the last 2.26 Gyr. It is a dynamically active, merging system with discrete mass components as revealed by substructure in X-ray, lensing and near-infrared maps of this cluster (Haines et al. 2010). The galaxy alignment appears to be stronger towards the centre and is mostly present among the fainter galaxies, whereas bright galaxies are unaligned (Hung et al. 2010). The luminosity function shows a steep red faint end upturn, suggesting that the least massive galaxies are just being quenched at this epoch (Bañados et al. 2010). Moreover, the cluster population shows two distinct populations: two-thirds are unremarkable blue, late-type spirals; the remainder, found only in the cluster outskirts, are dusty red-sequence galaxies whose star formation is heavily obscured. There is also an excess of 100-µm-selected galaxies that extend ∼6 Mpc in length along an axis that runs NE–SW through the cluster centre (Balogh et al. 2002; Haines et al. 2010).

This is the third paper in a series on Abell 1689, and a fourth one is in preparation. Houghton et al. (2012, hereafter Paper I) present the imaging and spectroscopy of the cluster and analyse the Faber–Jackson, Kormendy and colour–magnitude relations, based on data from the Advanced Camera for Surveys (ACS) on the *Hubble Space Telescope (HST)* and the Gemini Multi-Object Spectrograph on the Gemini North telescope (GMOS-N). D'Eugenio et al. (2013, hereafter Paper II) present integral field spectroscopy of a sample of galaxies observed with the Fibre Large Array Multi Element Spectrograph (FLAMES) at the Very Large Telescope, European Southern Observatory (ESO), and investigate their internal kinematics. In this paper, we analyse the photometry of 65 galaxies at the centre of Abell 1689, perform two-dimensional multicomponent surface-brightness decompositions, provide a morphological classification and derive the FP relationship for the ETGs (i.e. ellipticals or lenticulars) using different photometric models. In Paper IV (in preparation), we will provide a deep interpretation of the FP by measuring accurate dynamical masses of the sample galaxies observed with FLAMES and ACS.

This work is organized as follows. The sample selection is presented in Section 2. The photometric analysis is described in Section 3. The morphological classification is discussed in Section 4. In Section 5, the FP is derived, and the results are compared to the local FP. In Section 6, we draw our conclusions. We assume $H_0 = 71 \, \mathrm{km \, s^{-1} \, Mpc^{-1}}$, $\Omega_\mathrm{m} = 0.27$ and $\Omega_\Lambda = 0.73$, following the seven-year *Wilkinson Microwave Anisotropy Probe* (WMAP7) cosmology (Komatsu et al. 2011), as in Paper I.

2 SAMPLE

In this investigation, we used images from *HST* ACS. We downloaded the data, originally obtained for program GO-9289 (PI: H. Ford), from MAST.[1] The images are from the Wide Field Channel (WFC) with the *F625W* filter, which approximates the Sloan Digital Sky Survey (SDSS)-*r* filter and is nearly equivalent to rest-frame *V* band at the redshift of Abell 1689 ($z = 0.183$). Our data reduction procedures are described in Paper I.

We performed a photometric analysis of 65 galaxies, i.e. 54 galaxies from the spectroscopic sample and 11 from the ancillary sample, as described below.

[1] Mikulsi Archive for Space Telescopes at the Space Telescope Science Institute.

The primary sample we selected are galaxies from Paper I that were observed with GMOS-N plus those that were observed with FLAMES from Paper II. The field of view of the ACS/WFC/*F625W* image contains 43 galaxies from Paper I and 29 galaxies from Paper II. The two samples have 18 galaxies in common, so our entire spectroscopic sample consists of 54 individual galaxies.

We performed a two-dimensional photometric decomposition of the spectroscopic sample. This also required photometric analysis of 11 additional galaxies that affect the surface-brightness distribution of some of the spectroscopic sample galaxies on account of their proximity (Section 3.2). These 11 galaxies were therefore modelled with the aim of subtracting their two-dimensional surface-brightness distributions to improve the fits for the primary sample. We provide the derived parameters of our photometric decomposition as ancillary data.

Visual inspection of the images of the spectroscopy sample reveals that 41 are ETGs and 13 are late-type galaxies (LTGs; i.e. spirals). We list galaxy names, coordinates, morphological classification and central stellar velocity dispersions $\sigma_\star$ (see Section. 5.1) of the spectroscopic sample in Table 1. Our visual inspection of the contaminating galaxies forming the ancillary sample reveals that nine galaxies are ETGs and two are LTGs (Table 2).

3 TWO-DIMENSIONAL SURFACE-BRIGHTNESS FITS

To perform a photometric decomposition of each galaxy, we used the code GASP2D, which is described in detail by Méndez-Abreu et al. (2008, 2014). Briefly, GASP2D assumes that the surface-brightness distribution of elliptical galaxies consists of a single bulge component, and that disc galaxies are the sum of a bulge, a disc and, if necessary, a bar component. Each structure has elliptical and concentric isophotes with constant ellipticity, $\epsilon = 1 - q$, and constant position angle (PA). This algorithm has been used successfully to model ellipticals and brightest cluster galaxies (e.g. Ascaso et al. 2011), unbarred and barred disc galaxies (e.g. Morelli et al. 2012), active galaxies with an unresolved component (e.g. Benítez et al. 2013), high-z galaxies (Zanella et al. 2016) and, more recently, the large sample of galaxies from the Calar Alto Legacy Integral Field Area Data Release 3 (CALIFA-DR3, Méndez-Abreu et al. 2017).

3.1 Photometric model

For ellipticals and bulge components, we adopt the Sérsic (1963) law, i.e.

$$I_\mathrm{b}(r) = I_\mathrm{e} \, e^{-b_n \left[(r/r_\mathrm{e})^{1/n} - 1 \right]}, \qquad (1)$$

where r_e, I_e and n are the effective (or half-light) radius, the surface brightness at r_e and a shape parameter describing the curvature of the surface-brightness profile, respectively. The value of b_n is coupled to n so that half of the total luminosity of the bulge is within r_e and can be approximated as $b_n = 2n - 0.324$ (Ciotti 1991). The total luminosity of the bulge is

$$L_\mathrm{bulge} = 2\pi I_{0,\mathrm{bulge}} \, n \, r_\mathrm{e}^2 \frac{\Gamma(2n)}{b_n^{2n}} \, q_\mathrm{bulge}, \qquad (2)$$

where $I_{0,\mathrm{bulge}} = I_\mathrm{e} \, 10^{b_n}$ is the central surface brightness of the bulge, q_bulge is the bulge axial ratio and Γ is the Euler gamma function.

We consider as a special case the de Vaucouleurs (1948) law, which is essentially equation (1) with a fixed value of the Sérsic index $n = 4$.

Table 1. Spectroscopic sample.

Galaxy ID		RA (h m s)	Dec. (° ′ ″)	Type	Data	$\sigma_\star$ (km s^{-1})	FP sample
(1)	(2)	(3)	(4)	(5)	(6)	(7)	(8)
S01	286, –	13 11 23.09	−1 21 17.1	Late	G	150.7 ± 2.9	No
S02	341, 28	13 11 24.47	−1 21 10.9	Early	G,F	190.5 ± 3.6	Yes
S03	368, –	13 11 25.39	−1 20 36.8	Late	G	167.1 ± 3.3	No
S04	371, –	13 11 25.41	−1 20 17.0	Early	G	166.9 ± 6.5	Yes
S05	390, 30	13 11 25.96	−1 19 51.7	Early	G,F	171.5 ± 3.3	Yes
S06	398, 14	13 11 26.24	−1 19 56.3	Early	G,F	280.2 ± 4.7	Yes
S07	433, –	13 11 26.93	−1 19 40.5	Early	G	67.7 ± 11.8	Yes
S08	435, 16	13 11 26.94	−1 19 36.6	Early	G,F	151.7 ± 4.1	Yes
S09	463, 13	13 11 27.43	−1 20 2.3	Early	G,F	182.7 ± 3.6	Yes
S10	476, –	13 11 27.86	−1 20 7.5	Early	G	260.4 ± 5.1	Yes
S11	481, –	13 11 27.94	−1 21 36.5	Early	G	143.8 ± 4.1	Yes
S12	501, –	13 11 28.25	−1 20 43.3	Late	G	149.1 ± 4.8	No
S13	508, –	13 11 28.39	−1 19 58.3	Late	G	126.9 ± 5.5	No
S14	514, 29	13 11 28.48	−1 20 24.9	Early	G,F	179.5 ± 2.3	Yes
S15	531, –	13 11 28.78	−1 19 2.4	Late	G	101.5 ± 6.8	No
S16	549, 10	13 11 29.04	−1 21 16.6	Early	G,F	220.3 ± 2.9	Yes
S17	567, 17	13 11 29.35	−1 19 16.4	Early	G,F	250.4 ± 3.8	No
S18	584, 12	13 11 29.52	−1 20 27.8	Early	G,F	270.2 ± 5.0	Yes
S19	593, –	13 11 29.79	−1 21 0.5	Early	G	131.9 ± 3.2	Yes
S20	601, –	13 11 29.91	−1 20 14.9	Early	G	109.3 ± 6.7	Yes
S21	610, 9	13 11 30.02	−1 20 39.9	Late	G,F	122.1 ± 2.3	No
S22	635, –	13 11 30.42	−1 20 45.2	Early	G	255.0 ± 3.6	Yes
S23	636, –	13 11 30.43	−1 20 34.7	Early	G	152.6 ± 5.5	Yes
S24	645, –	13 11 30.62	−1 20 43.5	Early	G	175.9 ± 4.5	Yes
S25	655, –	13 11 30.84	−1 20 30.5	Early	G	151.5 ± 3.4	Yes
S26	670, 25	13 11 31.14	−1 21 27.6	Early	G,F	240.9 ± 4.4	Yes
S27	677, –	13 11 31.17	−1 21 24.9	Early	G	185.8 ± 5.9	Yes
S28	690, 5	13 11 31.45	−1 19 32.5	Early	G,F	285.0 ± 2.4	Yes
S29	698, –	13 11 31.57	−1 19 24.4	Late	G	94.0 ± 5.6	No
S30	717, 18	13 11 32.04	−1 19 24.1	Early	G,F	182.5 ± 3.9	Yes
S31	723, 24	13 11 32.14	−1 21 37.9	Early	G,F	183.4 ± 3.8	Yes
S32	724, –	13 11 32.14	−1 19 36.0	Late	G	37.2 ± 13.1	No
S33	726, –	13 11 32.16	−1 19 46.5	Late	G	218.0 ± 2.6	No
S34	753, 6	13 11 32.71	−1 19 58.3	Early	G,F	312.6 ± 2.6	Yes
S35	755, –	13 11 32.72	−1 20 58.2	Early	G	92.8 ± 6.5	Yes
S36	756, 19	13 11 32.76	−1 19 31.4	Early	G,F	266.9 ± 3.1	Yes
S37	814, –	13 11 34.10	−1 21 1.7	Late	G	130.1 ± 3.9	No
S38	816, –	13 11 34.13	−1 21 18.4	Early	G	114.8 ± 3.4	Yes
S39	848, 22	13 11 34.81	−1 20 59.0	Early	G,F	185.7 ± 3.4	Yes
S40	852, 21	13 11 34.91	−1 20 4.2	Early	G,F	116.7 ± 3.1	Yes
S41	874, –	13 11 35.40	−1 21 33.0	Early	G	205.9 ± 2.7	Yes
S42	883, –	13 11 35.65	−1 20 12.0	Late	G	49.2 ± 8.2	No
S43	906, –	13 11 36.68	−1 19 42.5	Late	G	37.2 ± 9.3	No
S44	–, 1	13 11 28.14	−1 19 31.4	Early	F	236.8 ± 6.6	Yes
S45	–, 2	13 11 28.07	−1 18 43.6	Early	F	93.8 ± 4.8	Yes
S46	–, 3	13 11 29.44	−1 18 34.4	Early	F	198.9 ± 5.6	Yes
S47	–, 4	13 11 31.92	−1 18 53.5	Early	F	101.5 ± 6.3	Yes
S48	–, 7	13 11 34.82	−1 19 24.3	Early	F	129.1 ± 4.3	Yes
S49	–, 8	13 11 30.32	−1 20 29.0	Early	F	223.7 ± 3.3	Yes
S50	–, 11	13 11 27.88	−1 21 12.7	Late	F	112.3 ± 4.0	No
S51	–, 15	13 11 25.14	−1 19 30.8	Early	F	161.1 ± 5.9	Yes
S52	–, 23	13 11 31.12	−1 20 52.4	Early	F	181.4 ± 5.6	Yes
S53	–, 26	13 11 30.10	−1 20 42.6	Early	F	250.0 ± 5.9	Yes
S54	–, 27	13 11 30.07	−1 20 28.3	Early	F	231.7 ± 6.1	Yes

Note. Column (1): galaxy ID from this paper. Column (2): galaxy ID from Paper I and/or from Paper II. Column (3): right ascension (J2000.0). Column (4): declination (J2000.0). Column (5): Early-/late-type classification. Column (6): spectroscopic data available, GMOS-N (G) and/or FLAMES (F). Column (7): central stellar velocity dispersion and its 1σ error. Column (8): sample adopted in FP analysis.

Table 2. Ancillary sample.

Galaxy ID (1)	RA (h m s) (2)	Dec. (° ′ ″) (3)	Type (4)
A01	13 11 27.27	−1 20 09.7	Late
A02	13 11 30.26	−1 20 51.6	Early
A03	13 11 31.03	−1 21 27.6	Early
A04	13 11 28.38	−1 18 44.6	Early
A05	13 11 28.08	−1 19 28.1	Early
A06	13 11 24.21	−1 21 07.4	Late
A07	13 11 30.95	−1 20 27.6	Early
A08	13 11 30.05	−1 20 17.1	Early
A09	13 11 29.81	−1 20 19.6	Early
A10	13 11 28.65	−1 20 26.3	Early
A11	13 11 29.20	−1 21 20.5	Early

Note. Column (1): galaxy ID (Fig. 1). Column (2): right ascension (J2000.0). Column (3): declination (J200.0). Column (4): Early-/Late-type classification.

We describe the surface brightness of the disc component by an exponential law (Freeman 1970),

$$I_d(r) = I_{0,\text{disc}} \, e^{-r/h}, \tag{3}$$

where $I_{0,\text{disc}}$ and h are the central surface brightness and scalelength of the disc, respectively. The total luminosity of the disc is

$$L_{\text{disc}} = 2\pi I_{0,\text{disc}} \, h^2 q_{\text{disc}}, \tag{4}$$

where q_{disc} is the disc axial ratio.

We adopt the radial surface-brightness profile of a Ferrers (1877) ellipsoid to describe bar components,

$$I_{\text{bar}}(r) = \begin{cases} I_{0,\text{bar}} \left[1 - \left(\frac{r}{r_{\text{bar}}} \right)^2 \right]^{n_{\text{bar}}+0.5} & r \leq r_{\text{bar}} \\ 0 & r > r_{\text{bar}}, \end{cases} \tag{5}$$

where $I_{0,\text{bar}}$, r_{bar} and n_{bar} are the central surface brightness, length and shape parameter of the surface-brightness profile of the bar, respectively. The total luminosity of the bar is

$$L_{\text{bar}} = \pi \, I_{0,\text{bar}} \, r_{\text{bar}}^2 \frac{\Gamma(n_{\text{bar}} + 1.5)}{\Gamma(n_{\text{bar}} + 2.5)} \, q_{\text{bar}}, \tag{6}$$

where q_{bar} is the bar axial ratio. We chose to fix the n_{bar} parameter at $n_{\text{bar}} = 2$, following Laurikainen, Salo & Buta (2005). The total luminosity of the bar for $n_{\text{bar}} = 2$ is

$$L_{\text{bar}} = \pi \, I_{0,\text{bar}} r_{\text{bar}}^2 \frac{\Gamma(7/2)}{\Gamma(9/2)} \, q_{\text{bar}}. \tag{7}$$

3.2 Fitting procedure

We performed multiple fits of the sky-subtracted images of the galaxies. Specifically, each ETG was fitted as follows:

(i) as a single bulge component following a de Vaucouleurs profile (fits hereafter referred to as deVauc);

(ii) as a single bulge component following a Sérsic profile, (hereafter Sérsic);

(iii) as a sum of a bulge following a Sérsic profile, and a disc component (hereafter SeDisc);

(iv) when a bar is present, also as a sum of a bulge following a Sérsic profile, a disc and a bar component (hereafter SeDiBar).

Each LTG was fitted with a SeDisc model, or a SeDiBar model in cases where a bar was detected.

Since GASP2D accounts for seeing effects, for each galaxy we used an appropriate PSF, whose details are given in Paper I.

The choice of the region in which we perform the χ^2 minimization (see Méndez-Abreu et al. 2008 for details on the minimization algorithm) is a crucial issue. After extensive testing with mock galaxies, we concluded that the most-suitable maximum fitting radius, $r_{\max}$, is where $I(r_{\max}) = 1.5 \, \sigma_{\text{sky}}$. Indeed, we created artificial galaxies as described in Section 3.3, and performed photometric decompositions to a limit surface brightness of $0.1 \, \sigma_{\text{sky}}$, $0.25 \, \sigma_{\text{sky}}$, $0.50 \, \sigma_{\text{sky}}$, $0.75 \, \sigma_{\text{sky}}$, $1.0 \, \sigma_{\text{sky}}$,..., and $4.5 \, \sigma_{\text{sky}}$. We then analysed the distribution of the errors on the parameters (as in Section 3.3). Extending the fitting area to pixels where the sky noise dominates over the surface brightness of the galaxy leads to significant systematic errors in the fitted photometric parameters. In particular, it leads to an overestimate of r_e and Sérsic index n, if a single Sérsic component is fitted, and an overestimate of r_e, n, and also the scalelength h, if a sum of Sérsic and exponential components are fitted. In both cases, the size of the galaxy is overestimated. On the other hand, if the fit is performed within a region that is too restricted, the size of the galaxy derived from the photometric decomposition is underestimated. We find that thorough testing to identify the optimal maximum fitting radius is essential for avoiding potentially severe systematic errors in scaling relations involving galaxy sizes.

It is challenging to fit the surface-brightness distributions of galaxies that overlap. Each of these galaxies consequently has an underlying surface-brightness gradient that is due to its neighbours, and cannot be neglected. It must be treated as extra background light that must be removed. Although GASP2D is able to fit multiple galaxies simultaneously, dealing with more than two galaxies at once leads to degeneracy in the fit parameters. Therefore, for each galaxy, we took into account contamination due to the neighbours by subtracting their surface-brightness models in an iterative way.

The proximity problem is particularly onerous in two dense regions of the cluster, marked 'A' and 'B' in Fig. 1. Region A, which is the centre of the cluster with a surface area of ∼0.5 arcmin², includes 13 of our galaxies. As noted in Section 2, we fitted 11 ancillary galaxies in the field of view whose surface brightness affects the sample galaxies and whose photometric decomposition is presented in this paper. Five of these additional galaxies are in region A. We thus modelled the central 18 galaxies in the following iterative fashion:

(i) Fit the central cD galaxy (galaxy S18) and subtract its model.

(ii) Fit the outer less contaminated galaxies and subtract their models.

(iii) Proceeding inwards, fit the less contaminated galaxies and subtract their models.[2]

(iv) Repeat the previous step until the sample is complete.

(v) Repeat steps (i)–(iv) for each galaxy. Each fit is performed on the observed image from which the models of the surrounding galaxies from the most recent iteration are subtracted, leaving a final image that contains only the galaxy currently being modelled.

Step (v) is repeated until consistent values of fitted parameters for the whole central sample are obtained. For region A, we performed step (v) six times to obtain convergence. The comparison between the observed surface-brightness distributions of the 18 galaxies in the centre of Abell 1689 and their models is shown in Fig. 2.

---

[2] For each galaxy, we fitted a Sérsic, SeDisc, and, in cases where a bar is present, SeDiBar, and then chose the model that best describes the surface-brightness distribution of the galaxy, particularly in its outer regions, by visual inspection of the residuals images.
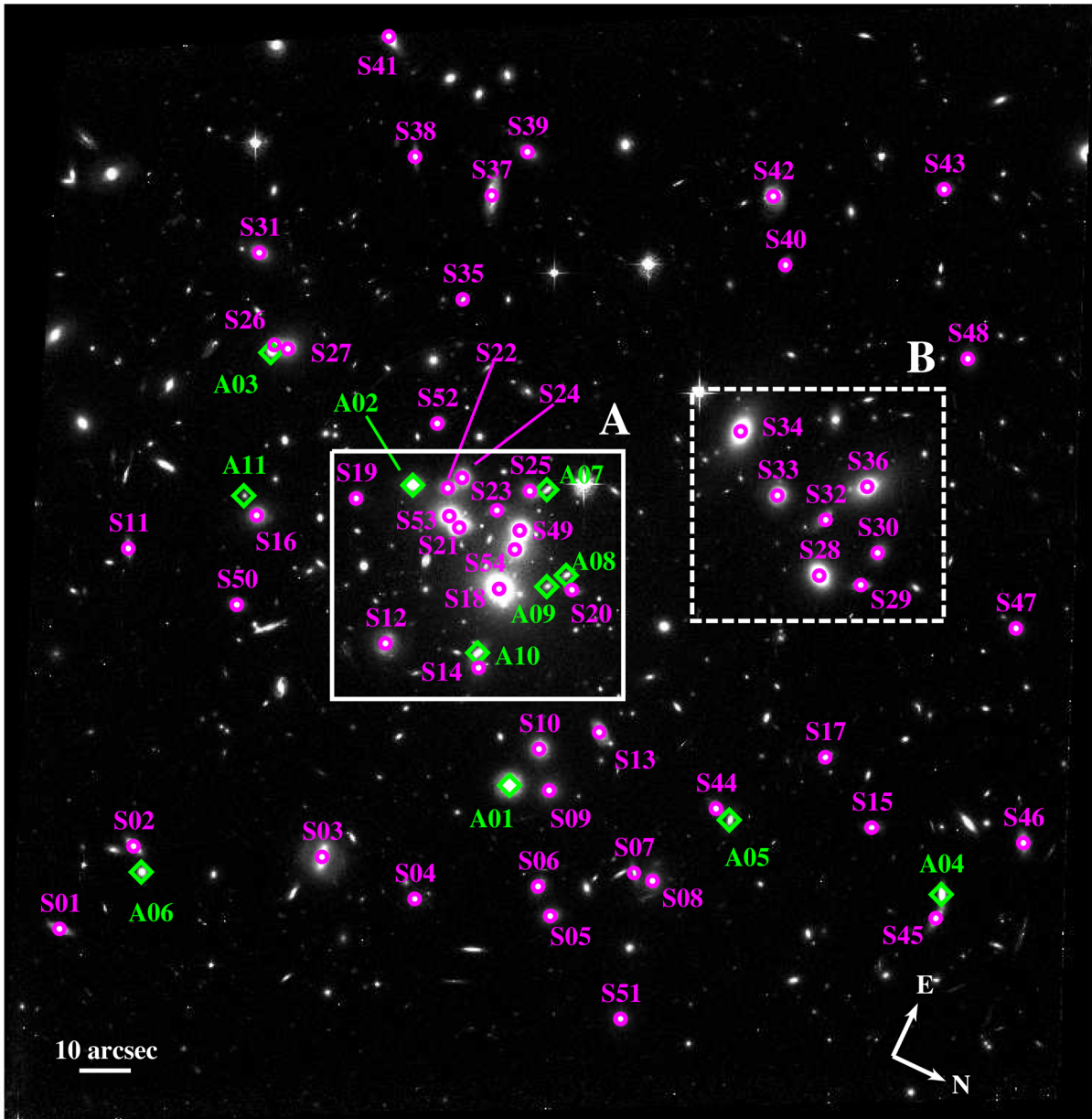
Figure 1. ACS/WFC/*F625W* image of Abell 1689. The white continuous and dashed frames highlight the regions A and B where the photometric decomposition was particularly challenging due to the light contamination of the crowded galaxies. Magenta circles mark the spectroscopic sample and green diamonds mark the ancillary sample. The linear scale and orientation are shown.
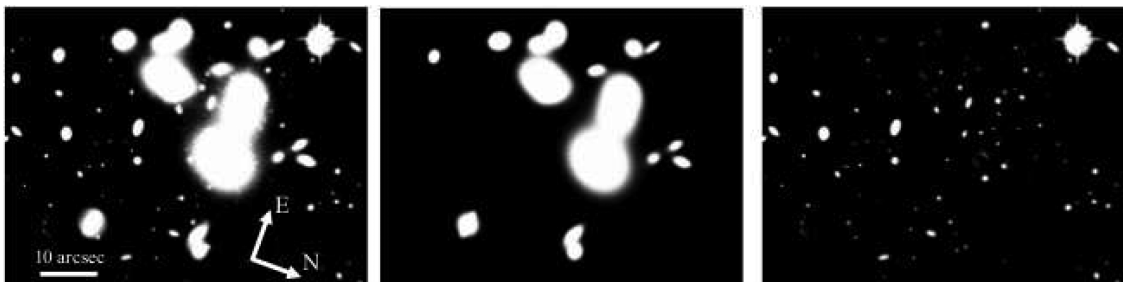

Figure 2. Left-hand panel: centre of Abell 1689, corresponding to region A of Fig. 1. Centre panel: synthetic image of region A, resulting from the composition of the modelled surface-brightness distribution of the 18 brightest galaxies. Right-hand panel: residual (observed − modelled) image of region A. The grey-scale, linear scale and orientation used for the panels are kept the same. Linear scale and orientation are shown on the left-hand panel.

We then subtracted from the whole observed ACS/WFC/*F625W* image the models of the 18 galaxies and used the resulting image to fit the seven galaxies in region B. We used the same iterative method described above, starting with the most extended galaxy (galaxy S34).

Finally, we subtracted from the original observed image the models of the 25 galaxies fitted in regions A and B, and used the resulting image to fit the rest of the sample galaxies. We adopted the iterative method described above for a few sub-groups of three or four galaxies. When the iterative process converged, we cut a frame for each sample galaxy and used it for the final fits. In all cases, the individual frames were large enough to include the entire region defined by r_{max}.

We were able to fit all the galaxies with the exception of S17. In this case, inspection reveals the presence of an edge-on disc, for which a thick-disc model is required. GASP2D is not yet able to fit a thick-disc model, so only deVauc and Sérsic fits of S17 were performed.

3.3 Error estimates

To estimate the errors on the fitted parameters, we ran a series of Monte Carlo simulations. For every fit type – deVauc, Sérsic, SeDisc and SeDiBar – we created 250 artificial galaxies characterized by parameters appropriate to the specific model. Simulations were carried out in one-magnitude bins, and five bins were required to cover the luminosity range of our sample. Thus, for each fit type, about 1250 artificial galaxies were created. Each parameter p_i was randomly chosen in the range $p_{min} - 0.3p_{min} < p_i < p_{max} + 0.3p_{max}$, where p_{min} and p_{max} are the minimum and maximum values of the fitted parameter on the real images in that particular magnitude bin.

The size of each artificial frame is 700×700 pixel^2, equivalent to 21×21 arcsec^2 (pixel scale = 0.03 arcsec pixel^{-1}). This is large enough to enclose r_{max} for all fits. We separately produced 250 mock galaxies in frames of 1600×1600 pixel^2, equivalent to 48×48 arcsec^2, to run simulations for the central cD galaxy. All the synthetic galaxies were convolved with a PSF that was randomly chosen from those produced for the fits to the observed image. The pixel scale, CCD gain and read-out-noise of the artificial images match those of the real *HST*/ACS/*F625W* image. In addition, we added photon noise in order to obtain a signal-to-noise ratio consistent with that of the original image.

We then ran the GASP2D two-dimensional parametric decomposition as described above to analyse the images of the mock galaxies. We studied the distribution of the relative errors on the parameters as $(p_{output}/p_{input} - 1)$. For PAs and axis ratios, we derived the absolute errors, $(p_{output} - p_{input})$. All the distributions appear to be nearly Gaussian. We measured the median and absolute deviation of each distribution and applied 5σ-clipping to reject outliers. Median values were used to detect the possible presence of systematic errors, and the absolute deviations were used to derive the errors on the single parameters. We did not identify any systematic errors, as all median values are consistent with zero.

In Table A1, we present the best-fitting observed parameters with their errors for the whole sample, adopting Sérsic, SeDisc and SeDiBar models according to the morphological classification presented in Section 4. In Figs A1–A64, we show the corresponding GASP2D fits. We give the results of the photometric decomposition of the ETGs of the spectroscopic sample with deVauc and Sérsic models in Tables A2 and A3, respectively.

4 MORPHOLOGICAL CLASSIFICATION

We were able to distinguish between ETGs and LTGs by visual inspection, as mentioned in Section 2, because the presence of spiral arms is clearly detectable, given the high signal-to-noise ratio and spatial resolution of the data.

Nevertheless, on the basis of visual inspection alone, it is not always possible to distinguish among ellipticals (E), unbarred lenticulars (S0) and possibly barred lenticulars (SB0), or to distinguish between spirals (S) and barred spirals (SB). This necessitates a more sophisticated and quantitative approach. We therefore made use of the multicomponent photometric decompositions and use the isophotal parameters derived in our fits to check for signatures of bars and discs. Barred galaxies are characterized by the presence of a local maximum in the ellipticity radial profile and constant PA in the bar region (e.g. Aguerri, Méndez-Abreu & Corsini 2009). A disc component is characterized by an exponential surface-brightness radial profile with constant ellipticity and PA.

By the combination of visual inspection and analysis of the isophotal parameters, we are able to detect with confidence the presence of a bar and therefore classify a galaxy as spiral (S), barred spiral (SB) or barred lenticular (SB0).

A more difficult problem arises when we need to distinguish between an E and S0, i.e. detect the presence of a disc. We note that for an E or S0, a Sérsic model is always a poorer fit than a SeDisc model, as the former has seven free parameters (i.e. I_e, r_e, n, ϵ_b, PA$_b$, and the centre x_0, y_0) and the latter has four more (I_0, h, ϵ_d, PA$_d$). We therefore conservatively classify a galaxy as an S0 only if we can associate the fitted exponential component to a real structure of the galaxy and not use it just as a mathematical expedient (see also Fritz et al. 2005; Méndez-Abreu et al. 2017).

For each candidate E or S0 galaxy, we visually examined the ellipse-averaged radial profile of the surface brightness, ellipticity and PA. We also compared the Sérsic and SeDisc fits, and closely inspected the modelled and residual images, as the latter are particularly useful for detection of any structured residual of the galaxy. If an outer exponential component is present, the galaxy is classified as S0. If no outer exponential is detected or the result is ambiguous, the galaxy is classified as S0 if both the ellipticity and PA radial profiles are better fitted with a SeDisc, otherwise the galaxy is classified as E. No additional spiral galaxies were detected from the analysis of the residuals of the photometric decomposition.

The method used to classify the galaxies is shown in the flowchart in Fig. 3. We further subclassified the ellipticals as En, where n is the integer approximating the value $10 \times (1 - q_{bulge})$ and $0 < n < 6$, following the van den Bergh (1976) classification. For unbarred and barred S0s and spirals, we also used the subclasses 'a, b and c' (van den Bergh 1976) on the basis of the disc-to-bulge luminosity ratio (Kormendy & Bender 2012, Kormendy, private communication).

Galaxy S18 is a cD, a giant elliptical with a typical extended envelope that is very well fit by an exponential component. Thus, its total surface-brightness distribution is best fitted by a SeDisc model.

The morphological classification of the galaxies and the features that allow us to discriminate among the different classes are shown in Table 3. Ellipticals are better fitted by a Sérsic model, S0s and Ss by a SeDisc model, and SB0s and SBs by a SeDiBar model. The deVauc model provides poorer fits of our ETGs than the Sérsic model, given that typically, Sérsic indices $n \neq 4$.

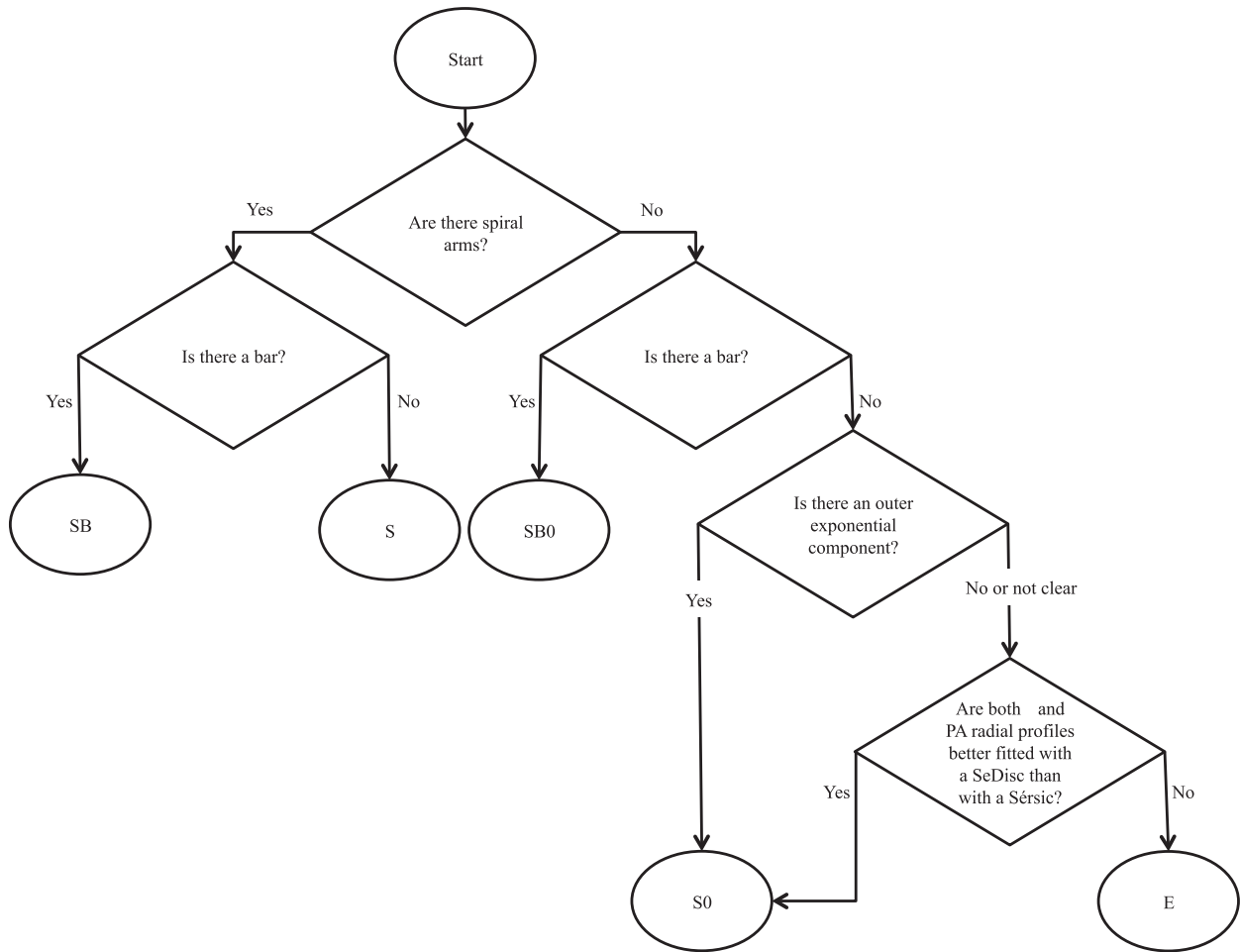**Figure 3.** Flowchart describing the method applied to classify the galaxies.

5 FP ANALYSIS

The sample analysed to determine the FP coefficients for Abell 1689 is composed of the ETGs of the spectroscopic sample with successful photometric decomposition. Only galaxy S17 is excluded from this analysis on account of its edge-on disc component (Section 3.2), so the total sample used in the FP analysis consists of the 40 galaxies listed in Table 1.

5.1 Central stellar velocity dispersions

We use central stellar velocity dispersions $\sigma_\star$ from Paper I, which are already corrected to a standard projected aperture of 1.62 kpc, equivalent to 3.4 arcsec at the distance of the Coma galaxy cluster (Jorgensen, Franx & Kjaergaard 1995b). Stellar velocity dispersions of the sample galaxies from Paper II were re-extracted for this study from the FLAMES/GIRAFFE spectra using a synthetic circular aperture that projects to 1.62kpc and adjusting the seeing to that of the GMOS-N data (FWHM $\approx$ 1 arcsec). For the 18 galaxies for which we have both GMOS-N and re-extracted FLAMES measurements, we take $\sigma_\star$ to be the weighted mean of the two values. The comparison between GMOS-N, re-extracted FLAMES, and mean velocity dispersions is shown in Fig. 4. The average difference between GMOS-N and FLAMES stellar velocity dispersion values, $\langle \sigma_{\text{GMOS-N}, i} - \sigma_{\text{FLAMES}, i} \rangle = 4.3 \, \text{km s}^{-1}$, that is within the mean 1σ error in the velocity dispersion ($\langle 1\sigma_{\text{FLAMES}} \rangle = 5.9 \, \text{km s}^{-1}$

and $\langle 1\sigma_{\text{GMOS-N}} \rangle = 4.4 \, \text{km s}^{-1}$). For this reason, we conclude that the two sets of data are consistent. The values of $\sigma_\star$ adopted for this analysis are given in Table 1.

5.2 FP fits of Abell 1689 ETGS

We use the fitting algorithm `LTS_PLANEFIT` described by Cappellari et al. (2013), which combines the robust Least Trimmed Squares technique of Rousseeuw & van Driessen (2006) with a least-squares fitting algorithm that allows for errors in all variables as well as intrinsic scatter. The best-fitting plane is defined as $z = a + b(x - x_0) + c(y - y_0)$, where x_0 and y_0 are the median of the measured values x_j and y_j, respectively. The intrinsic scatter, ϵ_z, is in the z-coordinate and defined in section 3.2.1 of Cappellari et al. (2013, equation 7 and following paragraph). The observed scatter, Δ, is defined as the standard deviation of $[a + b(x_j - x_0) + c(y_j - y_0) - z_j]$, where x_j, y_j and z_j are the fitted data values. In all our fits, we set the clipping parameter to 5σ, which results in no rejections of galaxies. Our choice of a large clipping parameter is driven by two considerations: (i) we have carefully checked each individual galaxy while performing the photometric decomposition and find no physical reason to exclude any galaxy, and (ii) for a direct comparison of the FP fits for different photometric models, we want the sample of galaxies to be the same in each case. The central cD galaxy S18 could be considered an 'outlier' for

Table 3. Morphological classification of the sample galaxies.

Galaxy ID	Type	Spiral arms	Bar	Exp. component	ε	PA
(1)	(2)	(3)	(4)	(5)	(6)	(7)
Spectroscopic sample						
S01	Sb	Y	N			
S02	S0b	N	N	Y		
S03	SBbc	Y	Y			
S04	E2	N	N	N	N	N
S05	E2	N	N	N	N	N
S06	E4	N	N	N	Y	N
S07	S0b	N	N	Y		
S08	S0ab	N	N	not clear	Y	Y
S09	S0ab	N	N	Y		
S10	S0ab	N	N	Y		
S11	S0b	N	N	Y		
S12	SBb	Y	Y			
S13	Sb	Y	N			
S14	S0ab	N	N	Y		
S15	SBbc	Y	Y			
S16	S0ab	N	N	Y		
S17	S0	N	N	Y		
S18	cD	N	N	Y		
S19	S0ab	N	N	Y		
S20	SB0bc	N	Y			
S21	SBbc	Y	Y			
S22	S0ab	N	N	Y		
S23	S0ab	N	N	not clear	Y	Y
S24	S0b	N	N	Y		
S25	SB0ab	N	Y			
S26	S0ab	N	N	Y		
S27	E1	N	N	not clear	Y	N
S28	E2	N	N	N	N	N
S29	Sbc	Y	N			
S30	S0a	N	N	Y		
S31	E3	N	N	N	N	N
S32	Sb	Y	N			
S33	Sb	Y	N			
S34	S0ab	N	N	Y		
S35	S0ab	N	N	Y		
S36	S0ab	N	N	Y		
S37	SBc	Y	Y			
S38	S0ab	N	N	Y		
S39	SB0ab	N	Y			
S40	S0b	N	N	Y		
S41	S0b	N	N	Y		
S42	Sc	Y	N			
S43	SBc	Y	Y			
S44	S0b	N	N	Y		
S45	S0b	N	N	Y		
S46	S0ab	N	N	Y		
S47	S0ab	N	N	Y		
S48	SB0ab	N	Y			
S49	S0ab	N	N	not clear	Y	Y
S50	SBb	Y	Y			
S51	S0a	N	N	not clear	Y	Y
S52	S0b	N	N	Y		
S53	S0b	N	N	Y		
S54	S0b	N	N	not clear	Y	Y
Ancillary sample						
A01	Sc	Y	N			
A02	S0b	N	N	Y		
A03	S0ab	N	N	not clear	Y	Y
A04	S0bc	N	N	Y		
A05	E5	N	N	N	N	N
A06	Sab	Y	N			
A07	S0b	N	N	Y		
A08	S0ab	N	N	Y		
A09	E2	N	N	not clear	N	N
A10	S0ab	N	N	Y		
A11	S0bc	N	N	Y		

Note. Column (1): galaxy ID (Fig. 1). Column (2): morphological type. Column (3): presence of spiral arms. Column (4): presence of a bar. Column (5): presence of an outer exponential component. Column (6): ϵ radial profile better fitted with a SeDisc rather than a Sérsic. Column (7): PA radial profile better fitted with a SeDisc rather than a Sérsic.
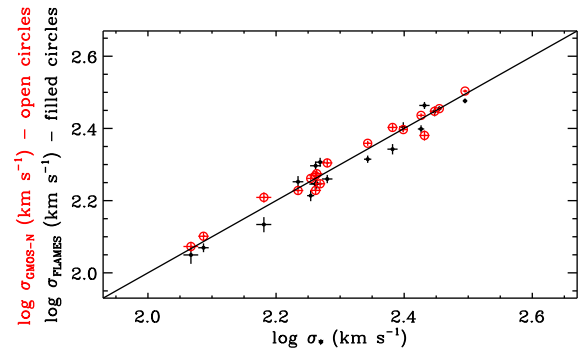
Figure 4. Central stellar velocity dispersions from GMOS-N (red open circles) and FLAMES (black filled circles) versus the adopted $\sigma_\star$ values. The continuous line defines the one-to-one relation.

its peculiar surface-brightness distribution, but we find consistent results regardless of whether or not S18 is included in the sample.

5.2.1 $\log \mathcal{R}_e$ as the dependent variable

We first fitted the FP in the classical form (Djorgovski & Davis 1987),

$$\log \mathcal{R}_e = a + b \log \sigma_\star + c \log \langle I \rangle_e, \qquad (8)$$

where $\mathcal{R}_e = r_e (q_{bulge})^{1/2}$ is the circularized effective radius in kpc, $\sigma_\star$ is the central stellar velocity dispersion in km s^{-1} (Section 5.1) and $\langle I \rangle_e = I_e \exp(b_n) \, n \, \Gamma(2n) \, b_n^{-2n}$ is the average surface brightness within the effective radius, in L$_\odot$ pc^{-2}. The conversion to L$_\odot$ pc^{-2} is obtained from $I = 10^{-0.4(\mu - \mu_\odot)}$, where $\mu_\odot = 26.222$ mag arcsec^{-2} is a constant depending on the absolute magnitude of the Sun in the observed passband. Each magnitude and surface brightness is corrected for Galactic extinction following Schlegel, Finkbeiner & Davis (1998), adopting an absorption $A = 0.073$ mag for the coordinates of Abell 1689 in the SDSS-*r* band. In each case, the surface brightness is also corrected for cosmological $(1 + z)^4$ dimming (Tolman 1930).

With the aim of comparing the FP coefficients derived by using different fits for the surface-brightness distributions of the galaxies, we perform the following fits, in which $\mathcal{R}_e$ and $\langle I \rangle_e$ are derived from the following:

(1) a deVauc model for all the galaxies;

(2) a Sérsic model for all the galaxies; and

(3) a Sérsic model for all galactic bulges, i.e. taken from a Sérsic model for Es, a SeDisc model for S0s and a SeDiBar model for SB0s.

We present FP coefficients along with intrinsic and observed scatter for the three fits in Table 4, and the corresponding plots are shown in Fig. 5. We note that the FP coefficients for different photometric models are not consistent.

We specify that we derived the FP corresponding to a deVauc model because it is usually done in literature, but with the warning that the deVauc model is not a good representation of the ETGs and does not provide very reliable values of $\mathcal{R}_e$ and $\langle I \rangle_e$. The FP derived by using a Sérsic model for all galactic bulges is the tightest, having a smaller intrinsic and observed scatter than the FP derived by adopting a Sérsic model.[3] From this, we conclude that the FP

---

[3] We exclude from this comparison the FP derived by using a deVauc model, for the reasons explained above.

Table 4. FP COEFFICIENTS OF ABELL 1689 FOR DIFFERENT DEPENDENT VARIABLES AND PHOTOMETRIC MODELS.

$z = a + b\,(x - x_0) + c\,(y - y_0)$						
a (1)	b (2)	c (3)	ϵ_z (4)	Δ (5)	x_0 (6)	y_0 (7)
$\log \mathcal{R}_e = a + b\,(\log \sigma_\star - \log \sigma_{\star,0}) + c\,(\log \langle I \rangle_e - \log \langle I \rangle_{e,0})$					$\log \sigma_{\star,0}$	$\log \langle I \rangle_{e,0}$
`deVauc` $\mathcal{R}_e$						
0.468 ± 0.012	1.092 ± 0.084	-0.817 ± 0.039	0.072	0.073	2.262	2.576
`Sérsic` $\mathcal{R}_e$						
0.532 ± 0.015	1.057 ± 0.104	-0.680 ± 0.033	0.091	0.091	2.262	2.475
`Sérsic` $\mathcal{R}_e$ of bulges						
0.065 ± 0.013	1.239 ± 0.089	-0.714 ± 0.024	0.070	0.079	2.262	3.054
$\log \sigma_\star = a + b\,(\log \mathcal{R}_e - \log \mathcal{R}_{e,0}) + c\,(\log \langle I \rangle_e - \log \langle I \rangle_{e,0})$					$\log \mathcal{R}_{e,0}$	$\log \langle I \rangle_{e,0}$
`deVauc` $\mathcal{R}_e$						
2.209 ± 0.010	0.756 ± 0.060	0.635 ± 0.054	0.060	0.060	0.3996	2.576
`Sérsic` $\mathcal{R}_e$						
2.243 ± 0.012	0.704 ± 0.069	0.490 ± 0.051	0.074	0.076	0.5064	2.475
`Sérsic` $\mathcal{R}_e$ of bulges						
2.227 ± 0.010	0.705 ± 0.050	0.504 ± 0.039	0.053	0.059	0.01504	3.054

Note. Column (1), column (2), and column (3): FP coefficients. Column (4): intrinsic scatter. Column (5): observed scatter (dex). Column (6) and column (7): median of the fitted x_i and y_i values, respectively. Values of $\mathcal{R}_e$ used to fit the FP are in kpc, $\sigma_{\star,0}$ in km s^{-1}, and $\langle I \rangle_{e,0}$ in $L_\odot$ pc^{-2}.

is defined by the bulges alone, rather than by the entire galaxies. This conclusion is strengthened by adding the bulges of the LTG sample; they all lie on the FP, with the exception of three galaxies (namely S32, S42, and S43) out of 13. These outliers are the galaxies with the lowest value of $\sigma_\star \sim 40$ km s^{-1}. According to Kormendy & Kennicutt (2004), they could be pseudo-bulges, which are similar to small discs (and therefore rotation supported) and made by slow evolution internal to galaxy discs. Indeed, the FP relation for elliptical and classical bulges holds till very low values of velocity dispersion (Costantin et al. 2017) and refers to pressure supported systems.

5.2.2 *log $\sigma_\star$ as the dependent variable*

In the FP fits to the three models described above, only $\sigma_\star$ is a fixed parameter common to all three. We therefore repeat the fits using $\log \sigma_\star$ as the dependent variable, to see whether the minimization process leads to consistent best-fitting planes. We present the results in Table 4 and show the results in Fig. 6. Only the fits obtained by using `Sérsic` photometric models and Sérsic models of bulges are consistent. We confirm that, with $\log \sigma_\star$ as the dependent variable, the tightest FP is that derived by the Sérsic bulges. Again, the bulges of LTGs also lie on the FP, with the exception of the three galaxies with $\sigma_\star < 50$ km s^{-1}.

5.3 Comparison with local FPs

5.3.1 *Coma cluster*

We first compare the FP we find for Abell 1689 with that derived for the Coma cluster by Jorgensen, Franx & Kjaergaard (1996, hereafter JFK96), which is based on an orthogonal fit. This is a classic comparison generally found in literature. For the sake of uniformity, we fit the Coma data with `LTS_PLANEFIT` and use $\log \mathcal{R}_e$ as the dependent variable, as in JFK96. We take $\sigma_\star$ from Jorgensen et al. (1995b) and photometric parameters in the Gunn-*r* from Jorgensen, Franx & Kjaergaard (1995a) that were derived from fitting a de Vaucouleur's law to the observed growth

curve. Our best-fitting FP is

$$\log \mathcal{R}_e = 0.432\,(\pm 0.012) + 1.263\,(\pm 0.073) \log \sigma_\star$$
$$- 0.810\,(\pm 0.037) \log \langle I \rangle_e, \tag{9}$$

which has *a*, *b* and *c* values consistent with those of JFK96 to within 1σ (we note that the zero-point of the FP in JFK96 corresponds to $(a - b \log \sigma_{\star,0} - c \log \langle I \rangle_{e,0})$.

The ACS/WFC/*F625W* image of Abell 1689 at $z = 0.183$ corresponds approximately to the rest-frame *V* band. We compute an average colour within the effective radius $(V - R)_{\text{Gunn}} = 1.22$ mag from a sample of 14 Coma cluster galaxies from Jorgensen et al. (1995a) and use this value to derive $\langle \mu \rangle_e$ in *V* band. We verified that we could use a common colour within the effective radius for E and S0 galaxies, deriving $(V - R)_{\text{Gunn}}$ for the two classes of galaxies (the morphological type was taken from Dressler 1980). We found consistent values. As a further test to increase the sample, we derived the average colour within the effective radius $(B_{\text{Johnson}} - R_{\text{Gunn}}) = 1.15$ mag for 31 ETGs (from Jorgensen et al. 1995a) and again colours for Es and S0s were in agreement. We then fit the Coma data to obtain the FP in the *V* band (hereafter FP$_{\text{Coma}}$), which is consistent with the Gunn-*r* FP. We present all our derived FP$_{\text{Coma}}$ values in Table 5. We compare FP$_{\text{Coma}}$ with our derived FP for Abell 1689 by adopting a `deVauc` model for $\mathcal{R}_e$ and $\langle I \rangle_e$ and adopting $\log \mathcal{R}_e$ as the dependent variable, for the sake of consistency. We find that from the local Coma cluster to Abell 1689, there is a decrease in the parameter *b*, from 1.279 ± 0.012 for Coma to 1.092 ± 0.084 for Abell 1689. The parameter *c* is consistent for the two clusters. We show the edge-on view of FP$_{\text{Coma}}$ together with the Abell 1689 data in Fig. 7. We also plot the values of parameters *b* and *c* for the two clusters.

5.3.2 *WINGS survey*

We can also compare our FP with that derived from the WIde-field Nearby Galaxy-cluster Survey (WINGS, Fasano et al. 2006; D'Onofrio et al. 2008). We took spectroscopic and *V*-band photometric data of the 'WINGS/W+S' sample of 282 galaxies
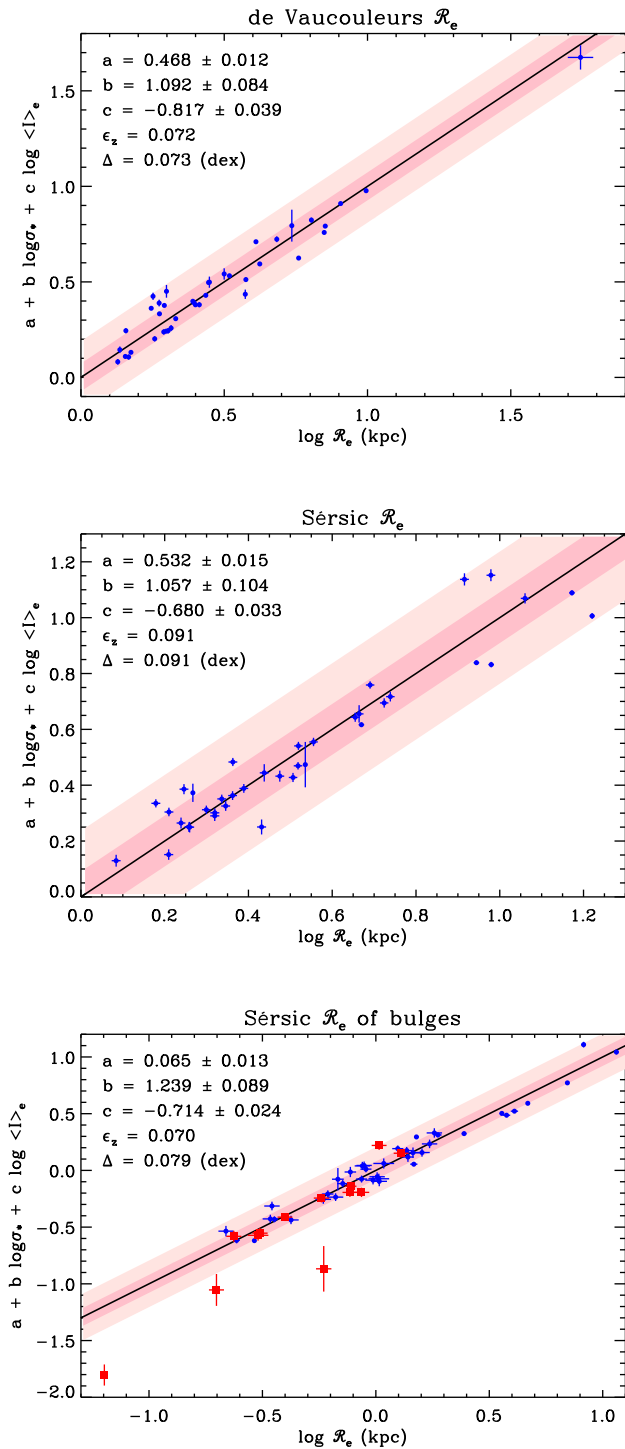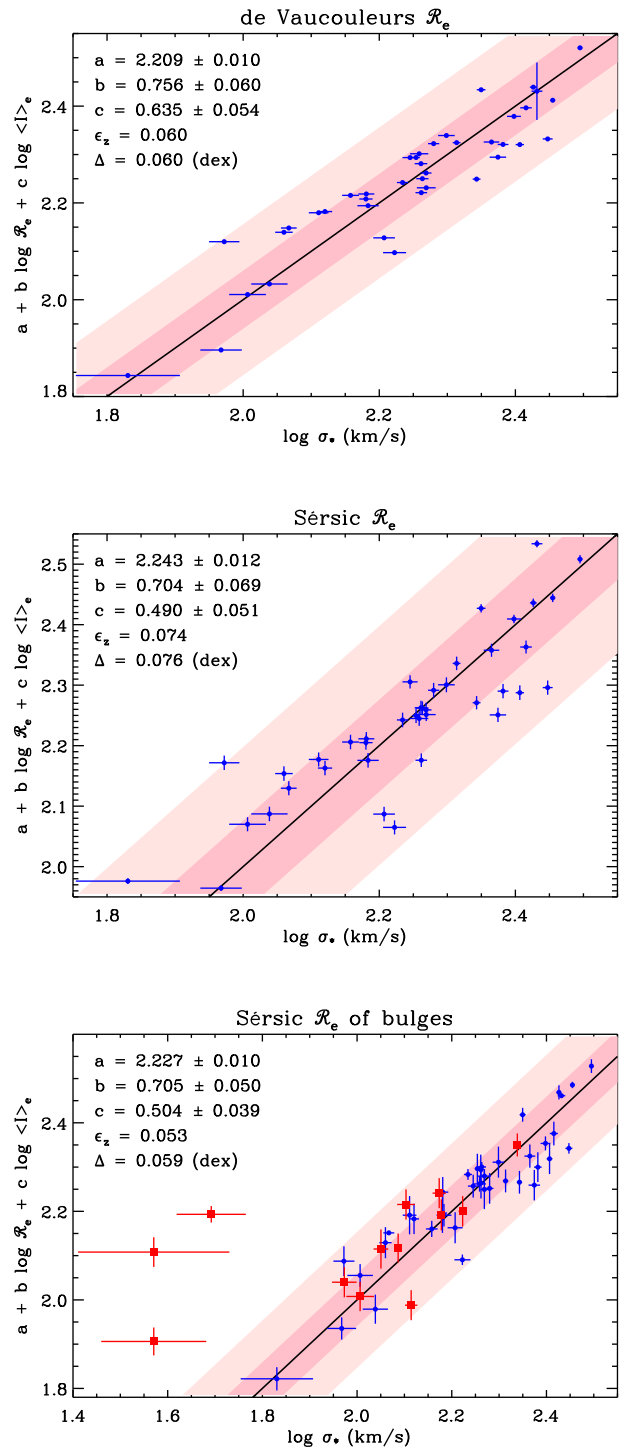
Figure 5. Edge-on view of the FP with $\log \mathcal{R}_e$ as dependent variable and using $\mathcal{R}_e$ and $\langle I \rangle_e$ from deVauc photometric model (top panel); Sérsic model (middle panel) and Sérsic model of bulges (bottom panel), as described in the text. Blue filled circles: ETG sample; red filled squares: bulges of the LTG sample. The LTG sample is not used for the fit and plotted to show how it lies on the FP. The dark- and light-pink shaded regions enclose the 1σ (equivalent to 68 per cent of the values for a Gaussian distribution) and 2.6σ (99 per cent) observed scatter, respectively.

Figure 6. Edge-on view of the FP with $\log \sigma$ as dependent variable and using $\mathcal{R}_e$ and $\langle I \rangle_e$ from different photometric models. For a description of panels and symbols see Fig. 5.

(D'Onofrio et al. 2008, private communication[4]), which are ETGs belonging to 13 nearby clusters in the redshift range $0.04 < z < 0.07$. We obtain values for $\mathcal{R}_e$ and $\langle I \rangle_e$ by fitting a Sérsic law to a growth curve.

---

[4] We note that the values of $\sigma_\star$ are corrected to the uniform aperture $\mathcal{R}_e/8$.

Table 5. Coma and WINGS FP coefficients.

$\log \mathcal{R}_e = a + b\,(\log \sigma_\star - \log \sigma_{\star,0}) + c\,(\log \langle I \rangle_e - \log \langle I \rangle_{e,0})$						
a	b	c	ϵ_z	Δ	$\log \sigma_{\star,0}$	$\log \langle I \rangle_{e,0}$
(1)	(2)	(3)	(4)	(5)	(6)	(7)
		Coma $-$ $\mathcal{R}_e$ from de Vaucouleurs law				
0.432 ± 0.012	1.279 ± 0.068	-0.804 ± 0.034	0	0.081	2.219	2.645
		WINGS $-$ $\mathcal{R}_e$ from Sérsic law				
0.4262 ± 0.0056	1.345 ± 0.050	-0.769 ± 0.020	0.076	0.100	2.166	2.408

Note. Column (1), column (2) and column (3): FP coefficients. Column (4): intrinsic scatter. Column (5): observed scatter (dex). Column (6) and column (7): median of the fitted x_i and y_i values, respectively. Values of $\mathcal{R}_e$ used to fit the FP are in kpc, $\sigma_{\star,0}$ in $\mathrm{km\,s^{-1}}$, and $\langle I \rangle_{e,0}$ in $\mathrm{L_\odot/pc^{-2}}$.
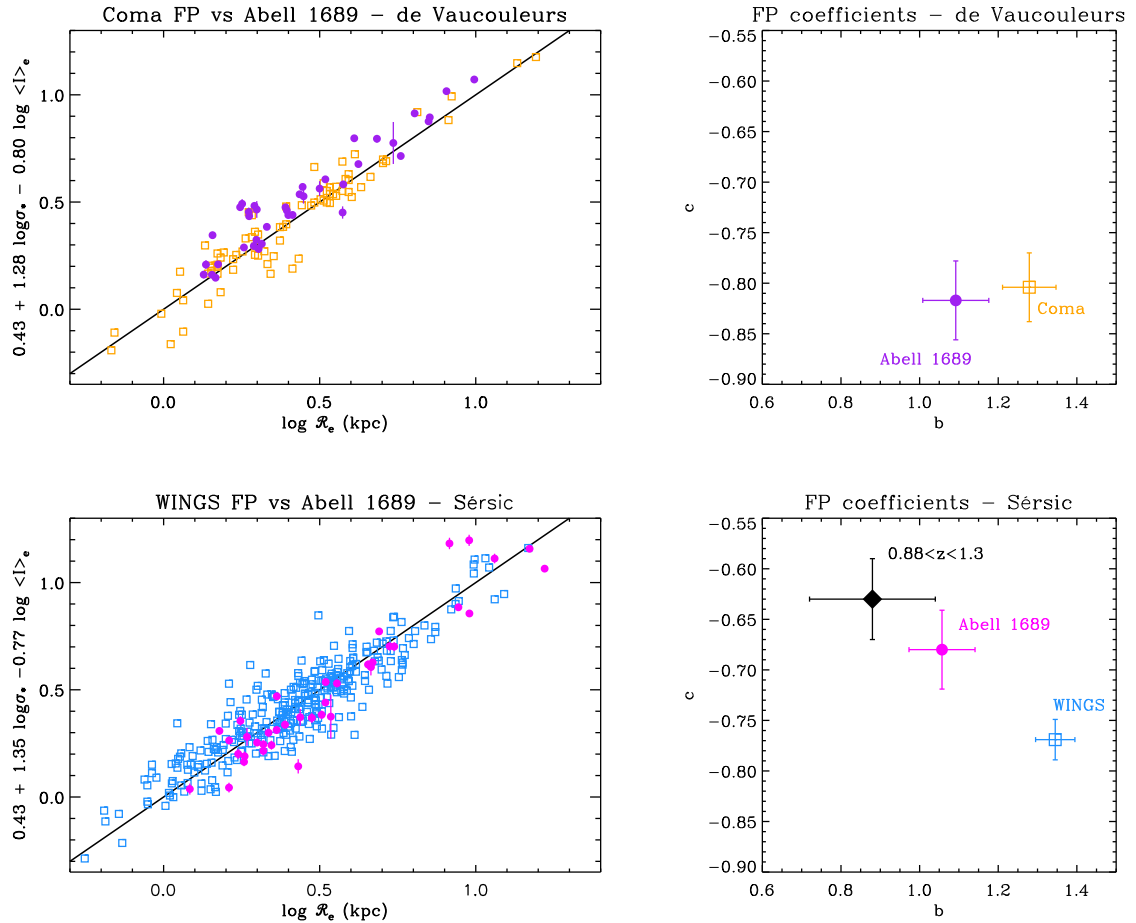
Figure 7. Top left-hand panels: edge-on-view of $\mathrm{FP_{Coma}}$ (black line) obtained for the Coma galaxies (orange squares); the Abell 1689 ETGs sample, whose photometric parameters are obtained with a `deVauc` model, is shown (purple circles). Top right-hand panel: *b* and *c* FP parameters obtained for the Coma (orange square) and Abell 1689 ETGs (purple circle) samples, both shown in the top left-hand panel. Bottom left-hand panels: edge on view of $\mathrm{FP_{WINGS}}$ (black line) obtained for the WINGS galaxies (light-blue squares); the Abell 1689 ETGs sample, whose photometric parameters are obtained with a `Sérsic` model, is shown (magenta circles). Bottom right-hand panels: *b* and *c* FP parameters obtained for the WINGS (light-blue square) and Abell 1689 ETGs (magenta circle) samples, both shown in the bottom left-hand panel; the FP parameters are plotted also for the sample of di Serego Alighieri et al. (2005) (black diamond).

For a more appropriate comparison, we fit the WINGS data with `LTS_PLANEFIT`, and use $\log \mathcal{R}_e$ as the dependent variable, as did D'Onofrio et al. (2008). The derived FP coefficients (hereafter, $\mathrm{FP_{WINGS}}$) are presented in Table 4. They are in agreement with those of D'Onofrio et al. (2008), which are based on an orthogonal fit. We compare the $\mathrm{FP_{WINGS}}$ with that derived for Abell 1689 with $\mathcal{R}_e$ as the dependent variable and use a `Sérsic` photometric model. The edge-on view of the WINGS FP and Abell 1689 data is shown in Fig. 7. We see a decrease in the value of the parameter *b* and an increase in the parameter *c* from the local WINGS FP to the that of

Abell 1689.[5] The parameters *b* and *c* for the two samples are plotted in Fig. 7.

---

[5] As a second caveat, the WINGS sample has values of $\sigma_\star < 95\,\mathrm{km\,s^{-1}}$. In our Abell 1689 analysis, only three galaxies do not strictly obey this selection criterion, since S07, S35 and S45 have $\sigma_\star = 67.7$, 92.8 and $93.8\,\mathrm{km\,s^{-1}}$, respectively. However, if we derive the Abell 1689 FP excluding these galaxies, our conclusions do not change.

6 DISCUSSION AND CONCLUSIONS

We perform a careful photometric analysis of 65 galaxies, specifically 50 ETGs and 15 LTGs, in the cluster Abell 1689 using rest-frame *V*-band ACS images. A two-dimensional multistructure photometric decomposition of each galaxy provides a complete morphological classification. For our sample, a `Sérsic` model of Es provides a better fit than a `deVauc` model, as on average, Sérsic indices $n \neq 4$. This is true also for the bulges of S0s, which are also well fit by a Sérsic profile, and S0s are well represented by a `SeDisc` model. For Ss, we present `SeDisc` models, and for SBs and SB0s, we provide `SeDiBar` models.

We use a sample of 40 ETGs to derive the FP by adopting $\mathcal{R}_e$ and $\langle I \rangle_e$ from different photometric models, i.e. a `deVauc` model, a `Sérsic` model and a Sérsic model for galaxy bulges. We find that the corresponding FP coefficients are not consistent within 1σ if we choose $\log \mathcal{R}_e$ as the dependent variable. This is partially confirmed if we choose $\log \sigma_\star$ as the dependent variable, in which case only FPs derived from `Sérsic` models and Sérsic models of bulges are in agreement. In both cases, the bulges of LTGs follow the FP, with the exception of 3 galaxies, out of 13, all with $\sigma_\star < 50 \, \mathrm{km \, s^{-1}}$. The tightest FP is the one derived by using a Sérsic model of the galactic bulges, thus the FP is better defined by the bulges alone rather than the entire galaxies.

Similar studies have already been published, e.g. Kelson et al. (2000a) compare the photometric parameters derived by fitting their sample, at $z = 0.33$, with a pure de Vaucouleurs law, a Sérsic law and a combination of a de Vaucouleurs bulge plus exponential disc; while they find large uncertainties on $\mathcal{R}_e$, they conclude that this does not affect the FP analysis (in Kelson et al. 2000b), because the product $\mathcal{R}_e \langle I \rangle_e^{-c}$, which enters the FP, remains stable. This result was confirmed by Fernández Lorenzo et al. (2011), who analysed ETGs in the redshift range $0.2 < z < 1.2$. Our investigation differs in that we perform a Sérsic bulge plus exponential disc (plus a Ferrers ellipsoid, in case a bar is present) decomposition, and discriminate between Es and S0s (Section 5.2.1).

We compare the FP for Abell 1689 with the FP derived for local samples. We first perform the classic comparison with $\mathrm{FP_{Coma}}$, where $\mathcal{R}_e$ and $\langle I \rangle_e$ are based on a de Vaucouleurs law fitting procedure. We find a hint of evolution in the *b* parameter, in the sense of decreasing with redshift. The evolution is more evident if we make the comparison with $\mathrm{FP_{WINGS}}$, where the photometric parameters were derived with a Sérsic model. The FP of Abell 1689 shows both an offset and rotation, given that *b* decreases and *c* increases with redshift. Interestingly enough, this trend is in agreement with di Serego Alighieri et al. (2005), who studied a sample of galaxies in the range $0.88 < z < 1.3$, in the rest-frame *B* band, and adopting a two-dimensional Sérsic model for the surface-brightness distribution. This study is based on field galaxies, but di Serego Alighieri, Lanzoni & Jørgensen (2006a,b) show that ETGs are the same in the field (using the sample of di Serego Alighieri et al. 2005) and in the clusters (using two clusters at $z = 0.8$–0.9 from Jørgensen et al. 2006, 2007). We use the comparison with di Serego Alighieri et al. (2005) for consistency in adopting a Sérsic model to derive the photometric parameters that enter the FP. We show their result in Fig. 7 (bottom right-hand panel). In our two comparisons, two things diverge: (i) the photometric model, and (ii) the local sample. As for (i), we find in our analysis that a `deVauc` model is poorer than a `Sérsic` model in reproducing the surface-brightness distribution of ETGs; as for (ii) we think that the WINGS survey, including data for thirteen clusters, is more representative of the global behaviour of local galaxies than the Coma cluster alone. For

these reasons, we conclude that the FP of Abell 1689 shows an evolution in both the *b* and *c* coefficients, in the sense described above. A comparison with a local sample in which Es, S0s and SB0s are fitted with multiple component surface-brightness distributions will be required to confirm this.

For 29 galaxies in our sample, we measure spatially resolved kinematics from FLAMES data (Paper II). In a future paper (Paper IV, in preparation), we will use the two-dimensional kinematic maps, alongside ACS photometry to fit dynamical models and measure accurate dynamical masses (Cappellari et al. 2007). We will therefore investigate the systematic variation of the stellar and dynamical mass-to-light ratios, and compare these measurements to the prediction of the FP.

REFERENCES

Abell G. O., 1958, ApJS, 3, 211
Aguerri J. A. L., Méndez-Abreu J., Corsini E. M., 2009, A&A, 495, 491
Ascaso B., Aguerri J. A. L., Varela J., Cava A., Bettoni D., Moles M., D'Onofrio M., 2011, ApJ, 726, 69
Balogh M. L., Couch W. J., Smail I., Bower R. G., Glazebrook K., 2002, MNRAS, 335, 10
Bañados E., Hung L.-W., De Propris R., West M. J., 2010, ApJ, 721, L14
Benítez E. et al., 2013, ApJ, 763, 136
Bernardi M. et al., 2003, AJ, 125, 1866
Burstein D., Bender R., Faber S., Nolthenius R., 1997, AJ, 114, 1365
Caon N., Capaccioli M., D'Onofrio M., 1993, MNRAS, 265, 1013
Cappellari M. et al., 2007, MNRAS, 379, 418
Cappellari M. et al., 2013, MNRAS, 432, 1709
Ciotti L., 1991, A&A, 249, 99
Costantin L., Méndez-Abreu J., Corsini E. M., Morelli L., Aguerri J. A. L., Dalla Bontà E., Pizzella A., 2017, A&A, 601, A84
D'Eugenio F., Houghton R. C. W., Davies R. L., Dalla Bontà E., 2013, MNRAS, 429, 1258 (Paper II)
D'Onofrio M. et al., 2008, ApJ, 685, 875-896
de Vaucouleurs G., 1948, Ann. Astrophys., 11, 247
di Serego Alighieri S. et al., 2005, A&A, 442, 125
di Serego Alighieri S., Lanzoni B., Jørgensen I., 2006a, ApJ, 647, L99

di Serego Alighieri S., Lanzoni B., Jørgensen I., 2006b, ApJ, 652, L145

Djorgovski S., Davis M., 1987, ApJ, 313, 59

Dressler A., 1980, ApJS, 42, 565

Dressler A., Lynden-Bell D., Burstein D., Davies R. L., Faber S. M., Terlevich R., Wegner G., 1987, ApJ, 313, 42

Faber S. M., Dressler A., Davies R. L., Burstein D., Lynden-Bell D., 1987, Nearly Normal Galaxies: From the Planck time to the Present. Springer-Verlag, New York, p. 175

Fasano G. et al., 2006, A&A, 445, 805

Fernández Lorenzo M., Cepa J., Bongiovanni A., Pérez García A. M., Ederoclite A., Lara-López M. A., Pović M., Sánchez-Portal M., 2011, A&A, 526, A72

Ferrers N. M., 1877, An Elementary Treatise on Spherical Harmonics and Subjects Connected With Them. Macmillan and Co, London, p. 108

Freeman K. C., 1970, ApJ, 160, 811

Fritz A., Ziegler B. L., Bower R. G., Smail I., Davies R. L., 2005, MNRAS, 358, 233

Fritz A., Böhm A., Ziegler B. L., 2009, MNRAS, 393, 1467

Haines C. P., Smith G. P., Pereira M. J., Egami E., Moran S. M., Hardegree-Ullman E., Rawle T. D., Rex M., 2010, A&A, 518, L19

Houghton R. C. W., Davies R. L., Dalla Bontà E., Masters R., 2012, MNRAS, 423, 256 (Paper I)

Hung L.-W., Bañados E., De Propris R., West M. J., 2010, ApJ, 720, 1483

Jorgensen I., Franx M., Kjaergaard P., 1995a, MNRAS, 273, 1097

Jorgensen I., Franx M., Kjaergaard P., 1995b, MNRAS, 276, 1341

Jorgensen I., Franx M., Kjaergaard P., 1996, MNRAS, 280, 167 (JFK96)

Jørgensen I., Chiboucas K., Flint K., Bergmann M., Barr J., Davies R., 2006, ApJ, 639, L9

Jørgensen I., Chiboucas K., Flint K., Bergmann M., Barr J., Davies R., 2007, ApJ, 654, L179

Kelson D. D., Illingworth G. D., van Dokkum P. G., Franx M., 2000a, ApJ, 531, 137

Kelson D. D., Illingworth G. D., van Dokkum P. G., Franx M., 2000b, ApJ, 531, 184

Komatsu E. et al., 2011, ApJS, 192, 18

Kormendy J., Bender R., 2012, ApJS, 198, 2

Kormendy J., Kennicutt R. C., Jr, 2004, ARA&A, 42, 603

La Barbera F., Busarello G., Merluzzi P., Massarotti M., Capaccioli M., 2002, ApJ, 571, 790

Laurikainen E., Salo H., Buta R., 2005, MNRAS, 362, 1319

Maybhate A. et al., 2010, ACS Instrument Handbook, Version 10.0. STScI, Baltimore, MD

Méndez-Abreu J., Aguerri J. A. L., Corsini E. M., Simonneau E., 2008, A&A, 478, 353

Méndez-Abreu J., Debattista V. P., Corsini E. M., Aguerri J. A. L., 2014, A&A, 572, A25

Méndez-Abreu J. et al., 2017, A&A, 598, A32

Morelli L., Corsini E. M., Pizzella A., Dalla Bontà E., Coccato L., Méndez-Abreu J., Cesetti M., 2012, MNRAS, 423, 962

Nigoche-Netro A., Ruelas-Mayorga A., Franco-Balderas A., 2008, A&A, 491, 731

Rousseeuw P., van Driessen K., 2006, Data Min. Knowl. Discovery, 12, 29

Saglia R. P., Bertschinger E., Baggley G., Burstein D., Colless M., Davies R. L., McMahan R. K., Jr, Wegner G., 1997, ApJS, 109, 79

Schlegel D. J., Finkbeiner D. P., Davis M., 1998, ApJ, 500, 525

Sérsic J. L., 1963, Boletin Asociacion Argentina Astron. La Plata Argentina, 6, 41

Sheth R. K., Bernardi M., 2012, MNRAS, 422, 1825

Simard L. et al., 2002, ApJS, 142, 1

Sirianni M. et al., 2005, PASP, 117, 1049

Struble M. F., Rood H. J., 1999, ApJS, 125, 35

Tolman R. C., 1930, Proc. Natl. Acad. Sci. USA, 16, 511

Tran K.-V. H., Simard L., Illingworth G., Franx M., 2003, ApJ, 590, 238

Trujillo I., Burkert A., Bell E. F., 2004, ApJ, 600, L39

van den Bergh S., 1976, ApJ, 206, 883

Zanella A. et al., 2016, ApJ, 824, 68

APPENDIX A: ADDITIONAL FIGURES AND TABLES
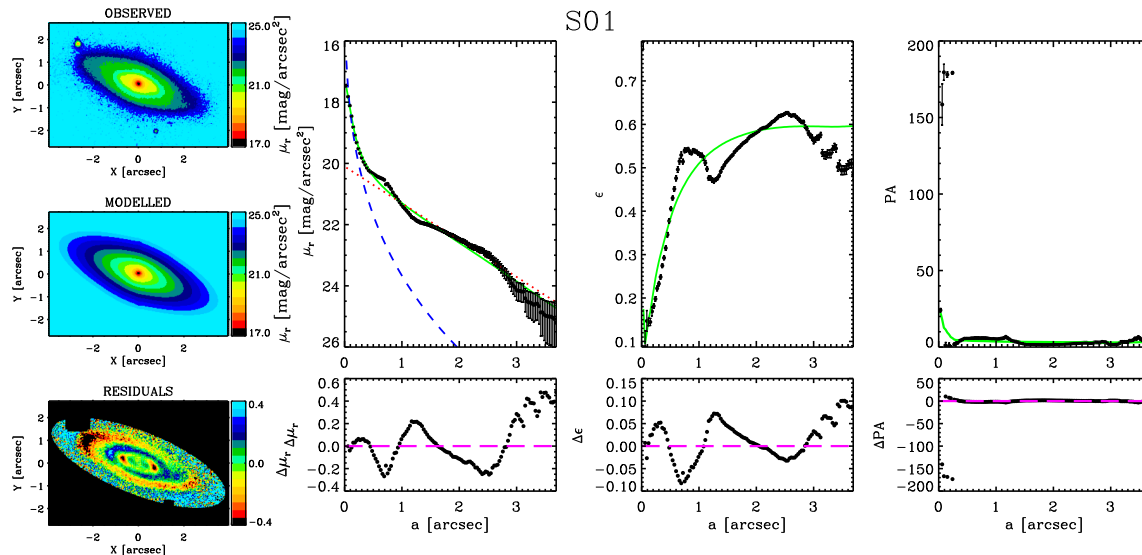
Figure A1. Two-dimensional photometric decomposition of the spiral galaxy S01 fitted with a `SeDisc`. Left-hand maps from top to bottom: observed, modelled and residual (observed–modelled) surface-brightness distribution of the galaxy. The mask applied to the image, containing the pixels rejected in the fit, is highlighted in black. Images are oriented as in Fig. 1, i.e. PA of *Y*-axis is 115°.12. Right-hand panels from left- to right-hand side and top to bottom: ellipse-averaged radial profile of surface-brightness, ellipticity and PA, measured in the observed (black dots with error-bars) and modelled image (green solid line). The dashed blue and dotted red lines represent the intrinsic surface-brightness radial profiles of the bulge and disc, respectively, along their semi major axis. The difference between the ellipse-averaged radial profiles extracted from the modelled and observed images is also shown.
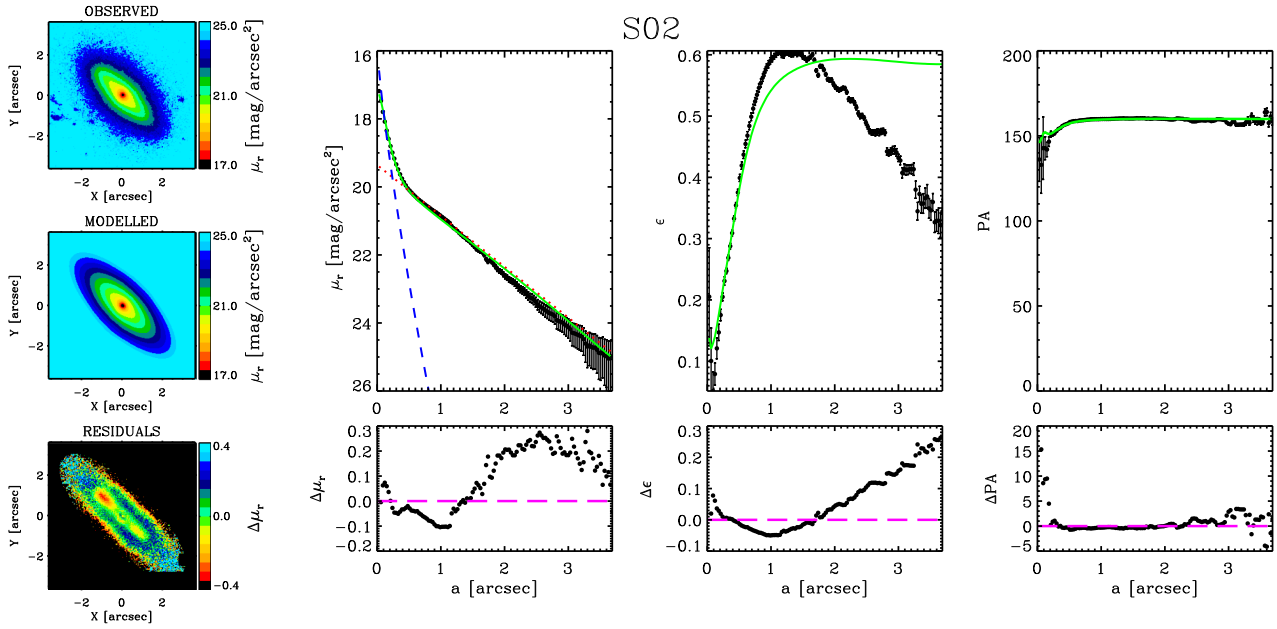
Figure A2. As in Fig. A1 but for galaxy S02 (`SeDisc` model).
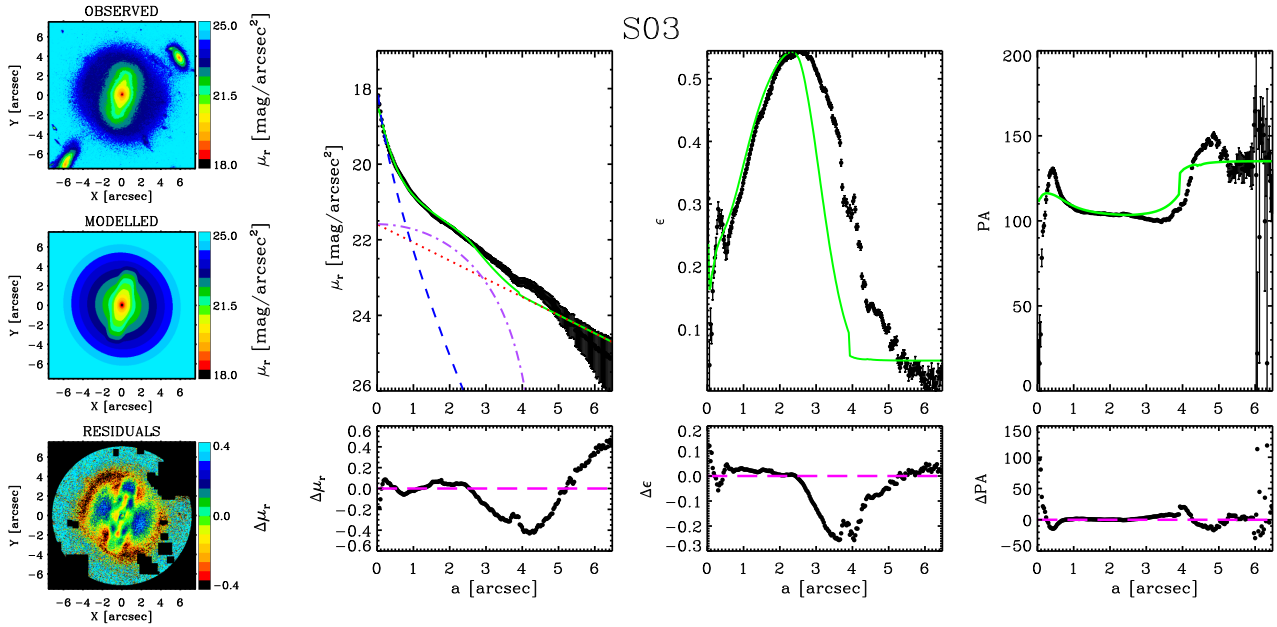
Figure A3. As in Fig. A1 but for galaxy S03 fitted with a `SeDiBar` model. The dash-dotted purple line represents the intrinsic surface-brightness radial profile of the bar along its semi major axis.
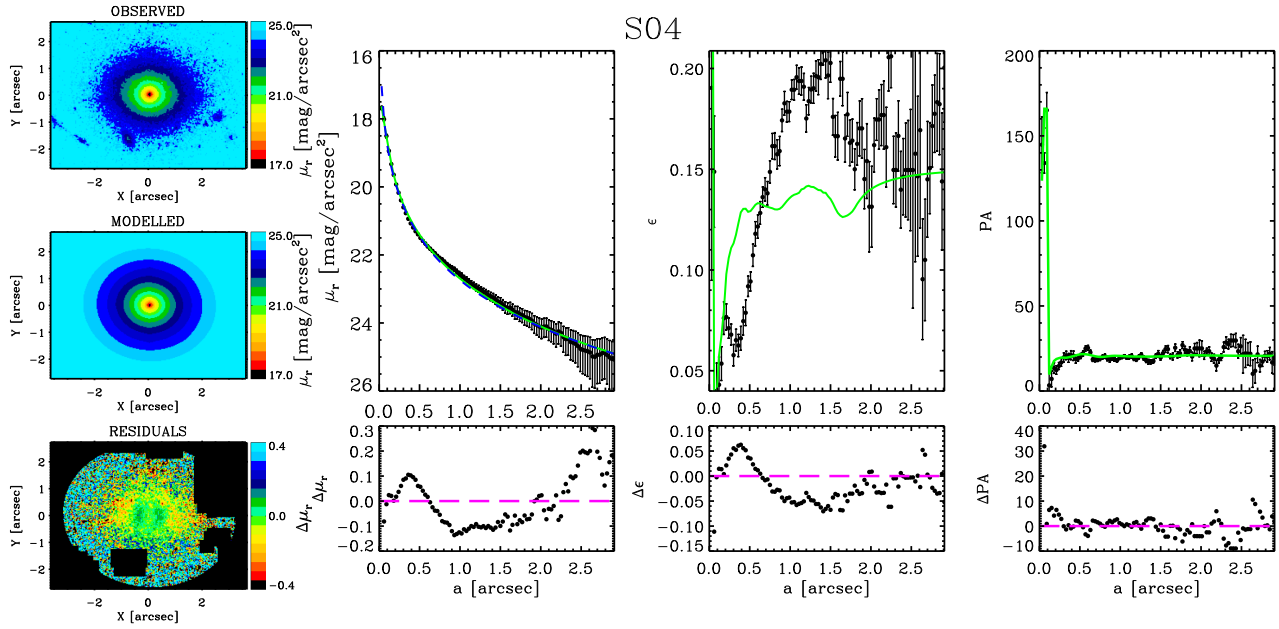
S04

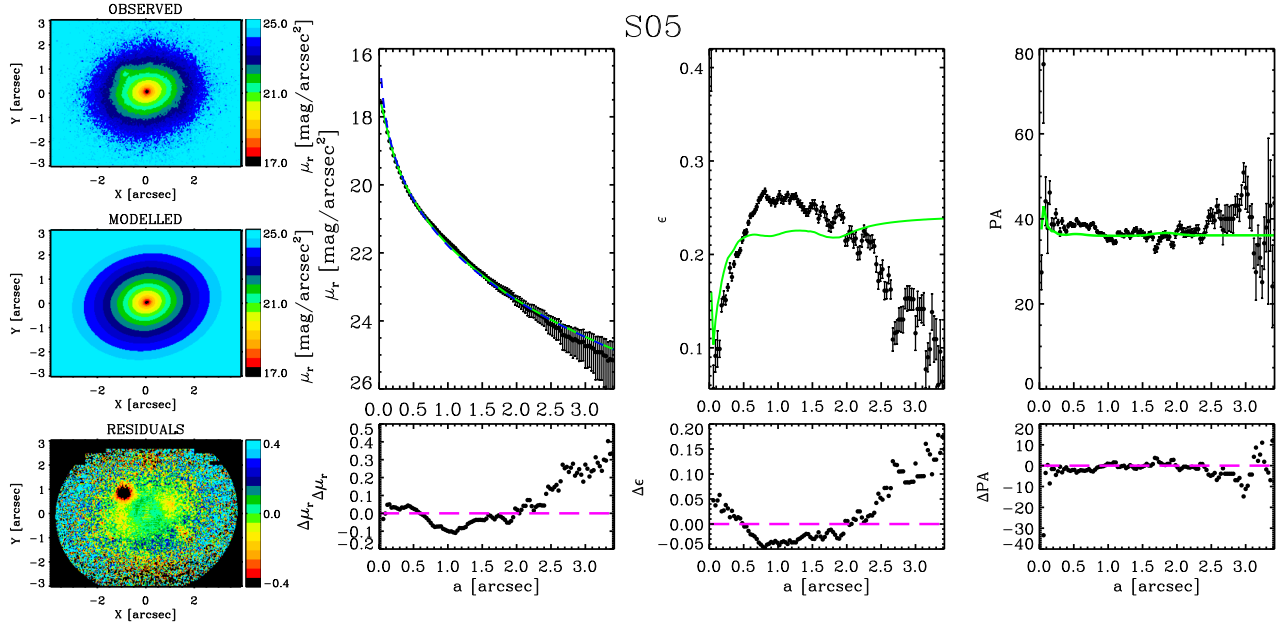**Figure A4.** As in Fig. A1 but for galaxy S04 fitted with a Sérsic model.

S05

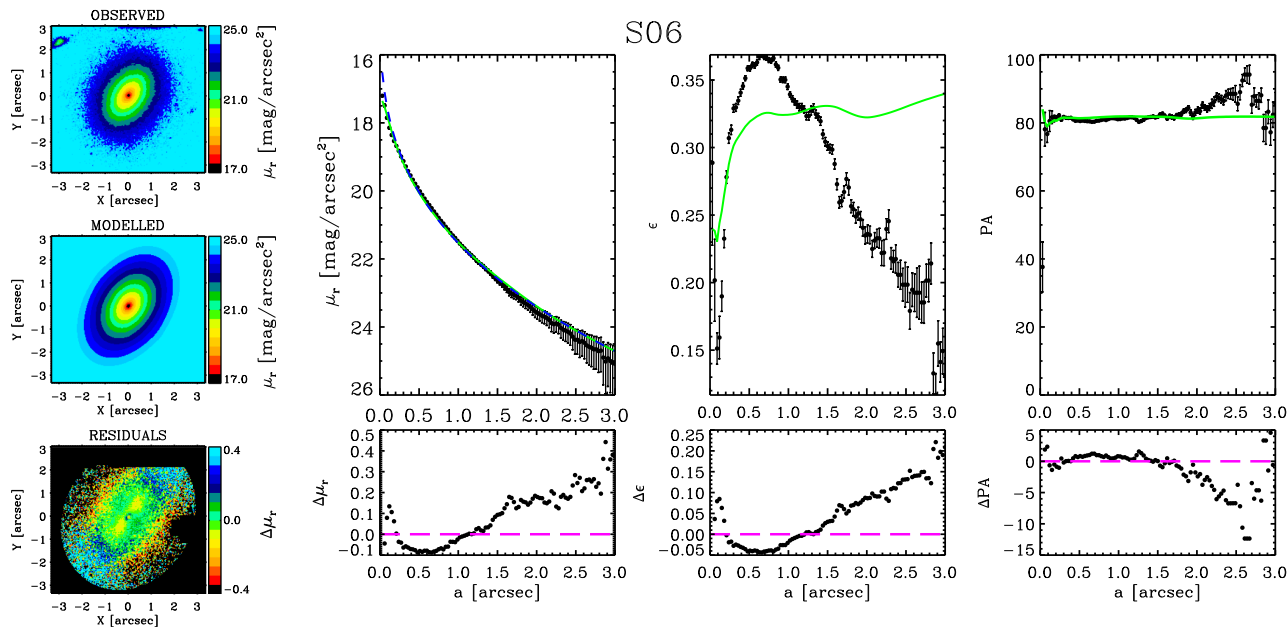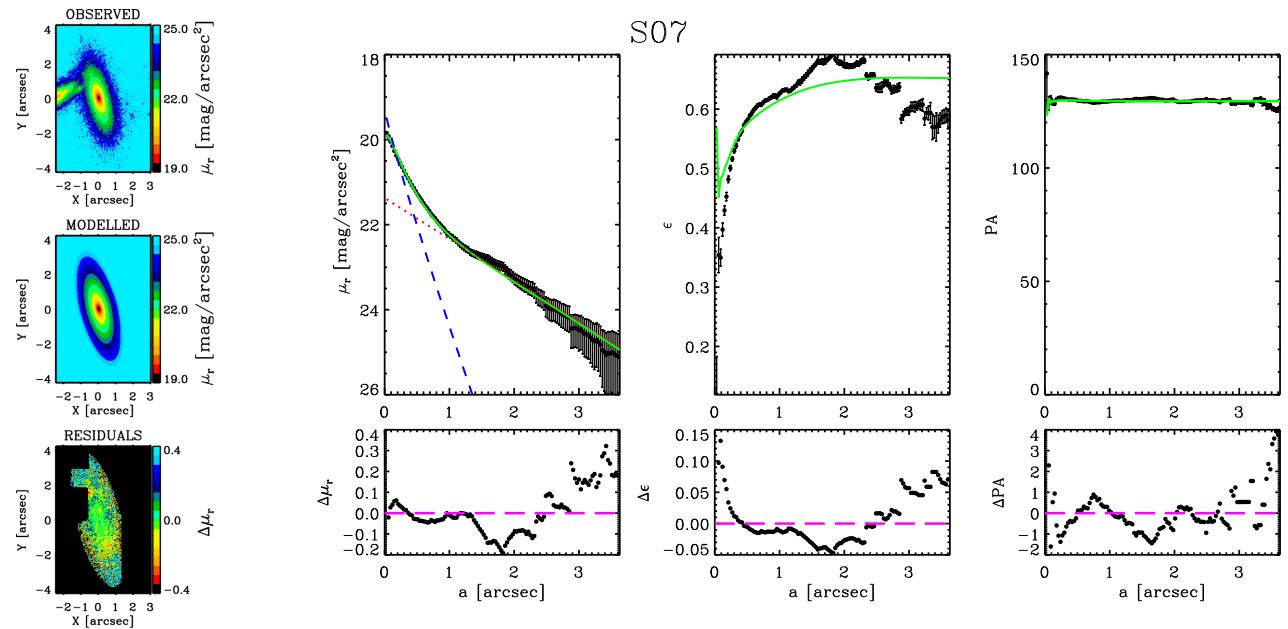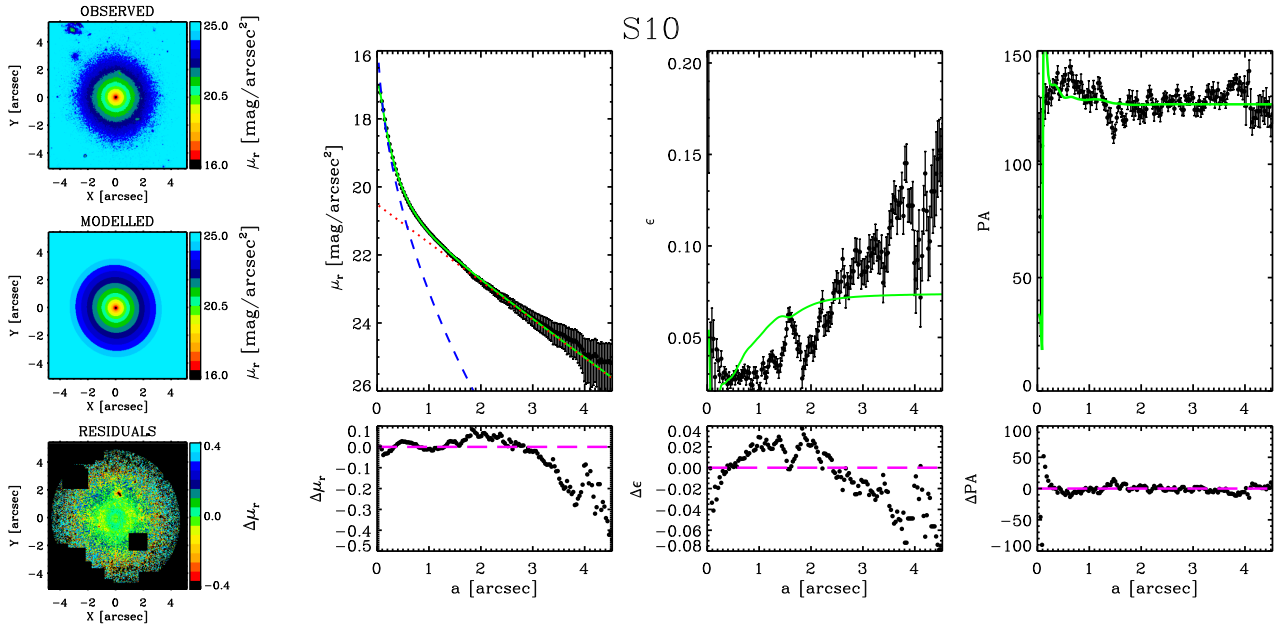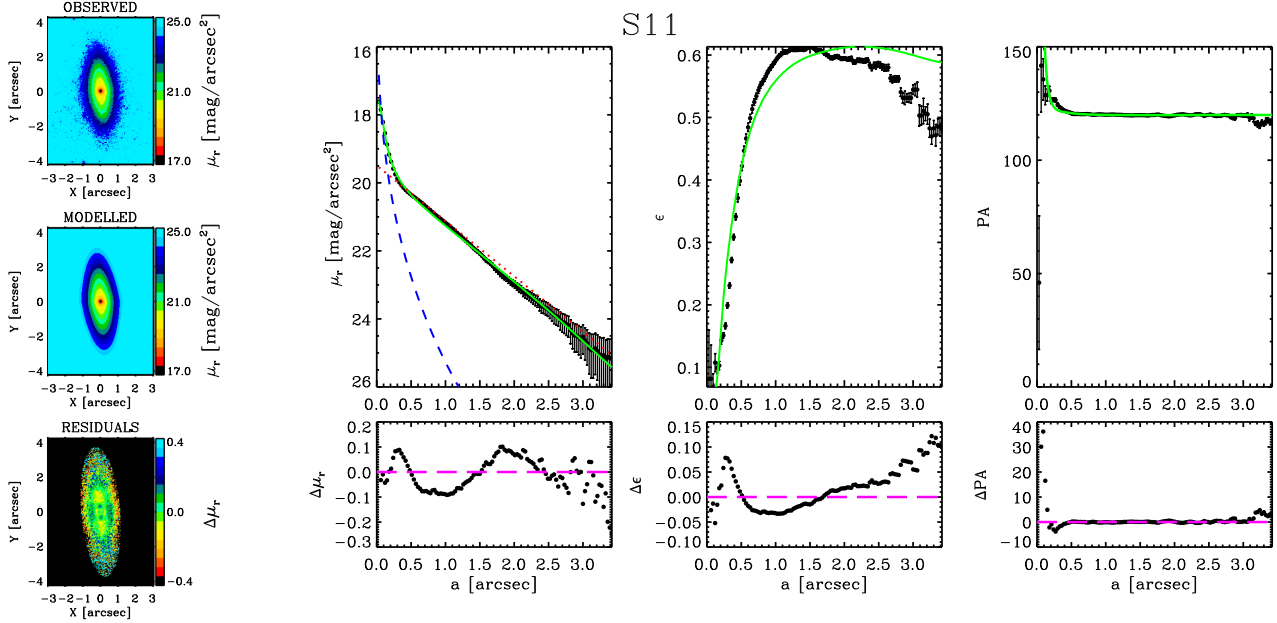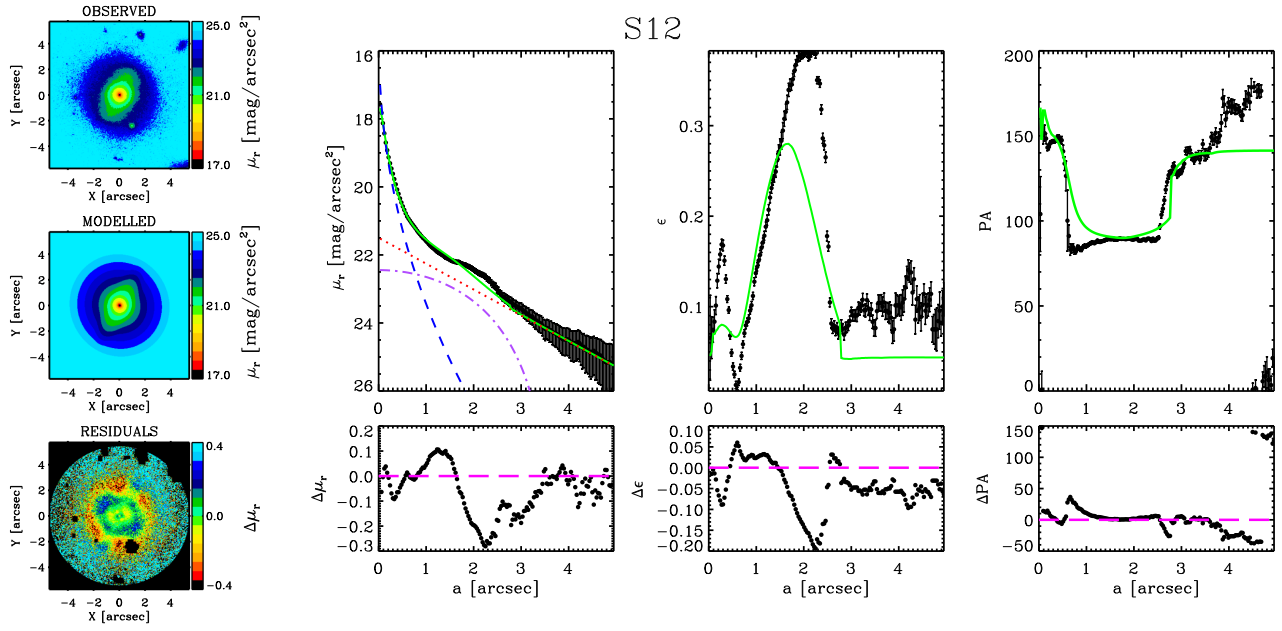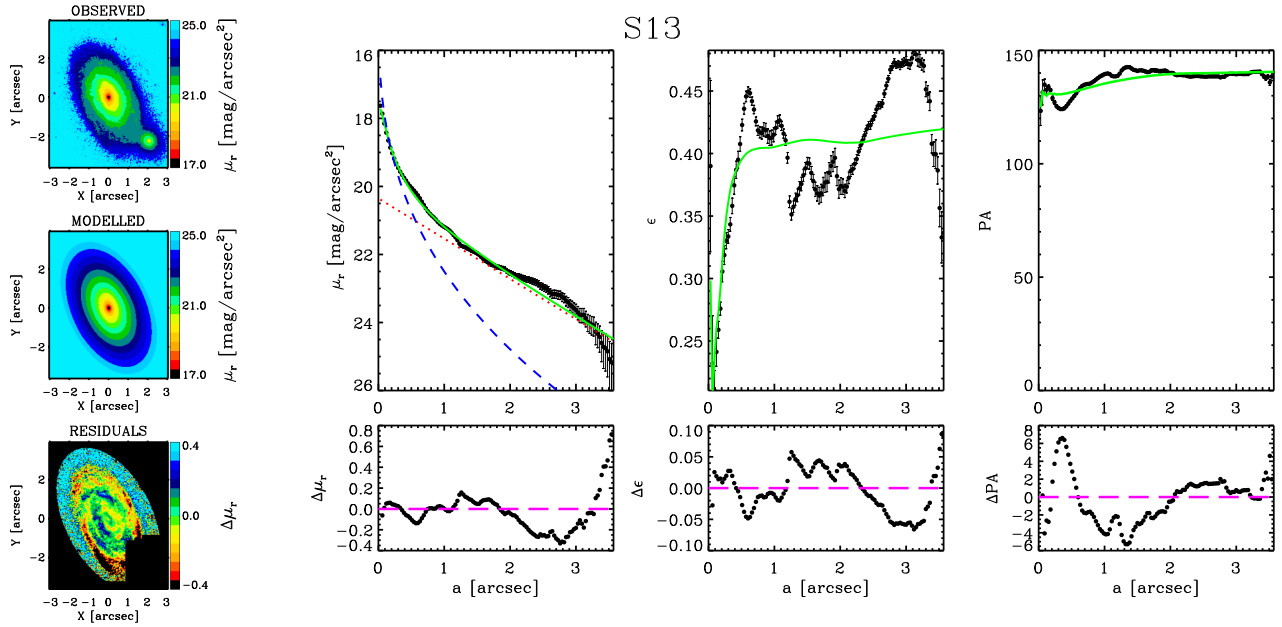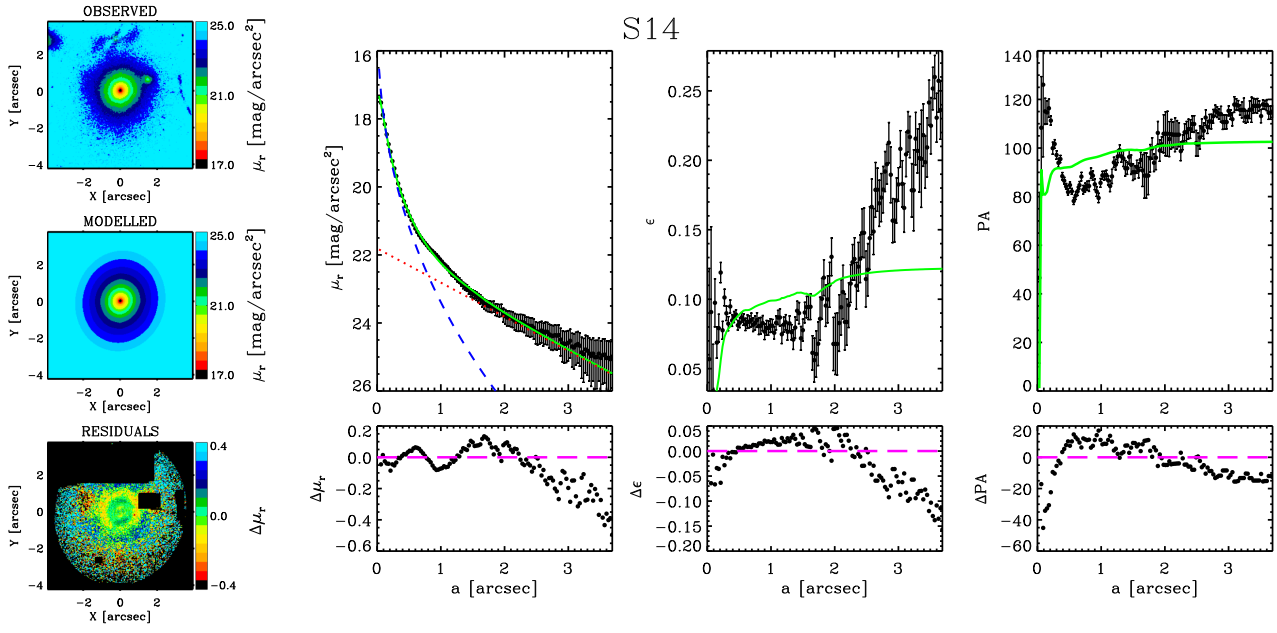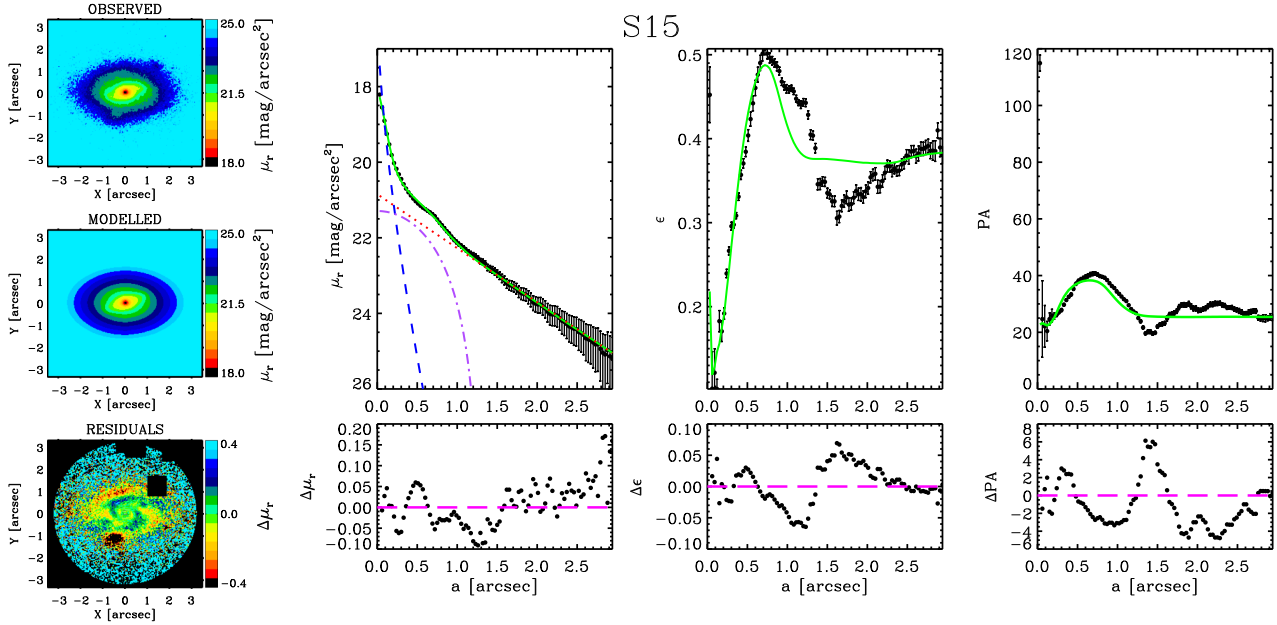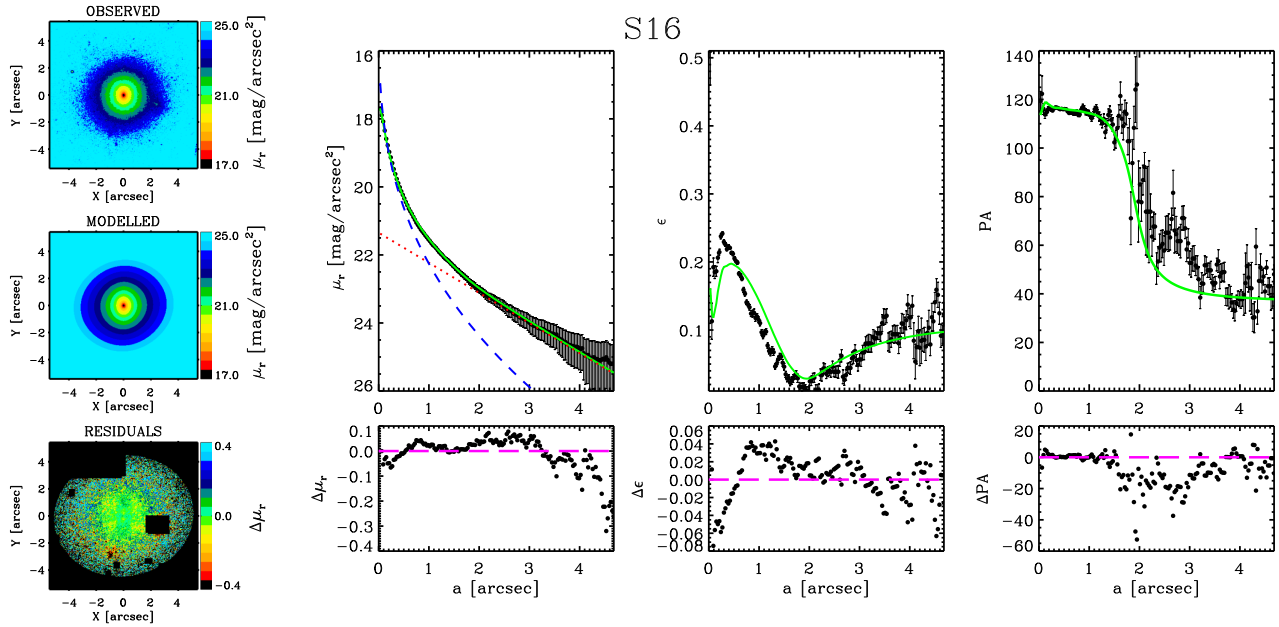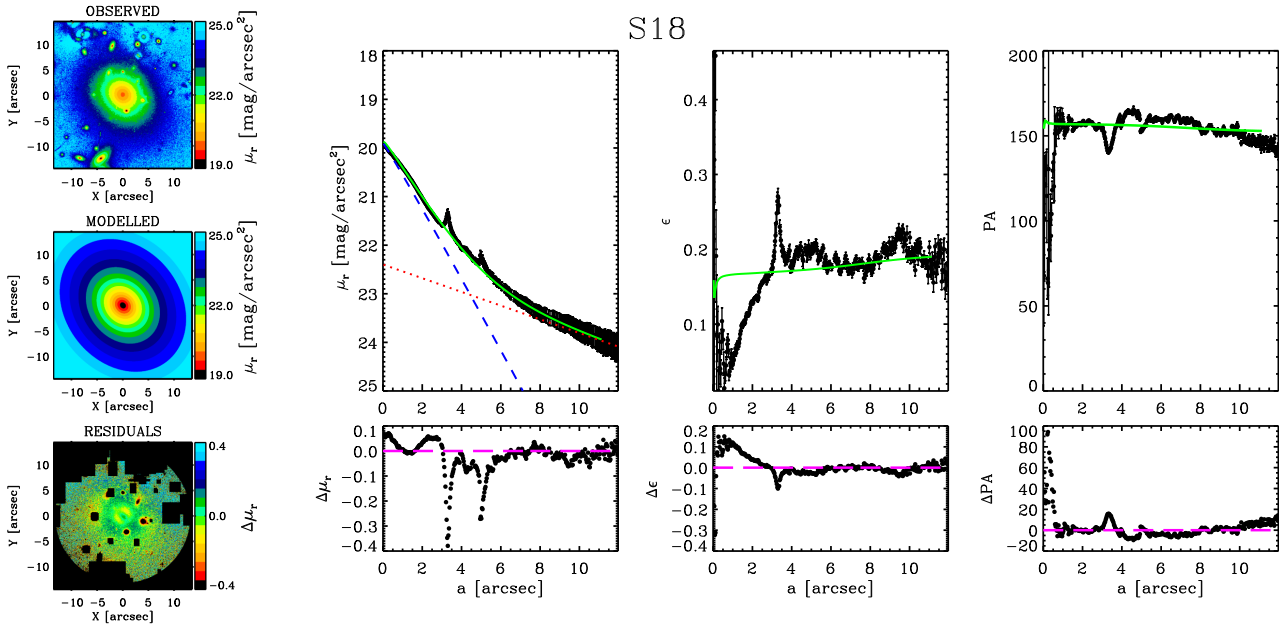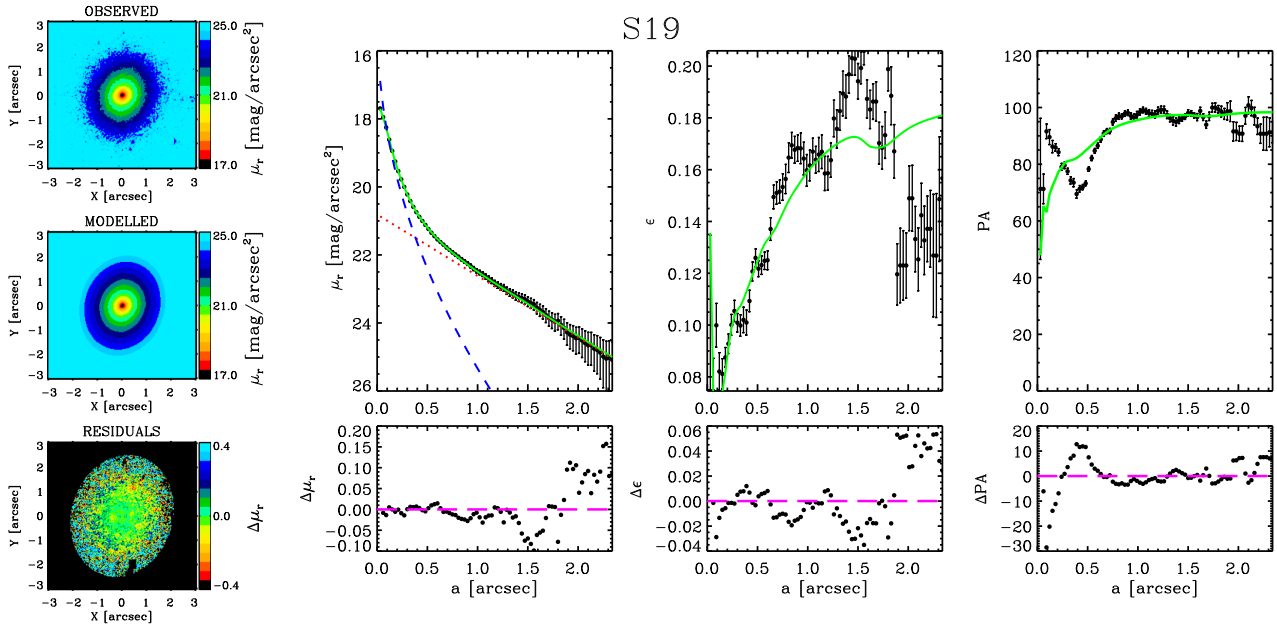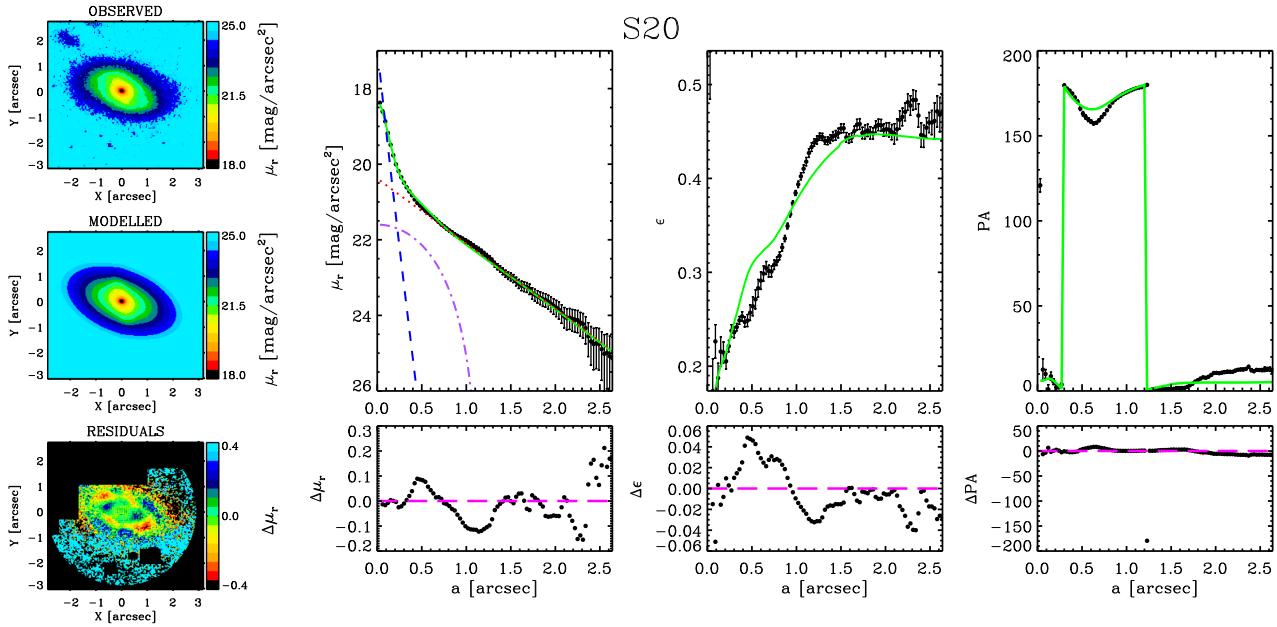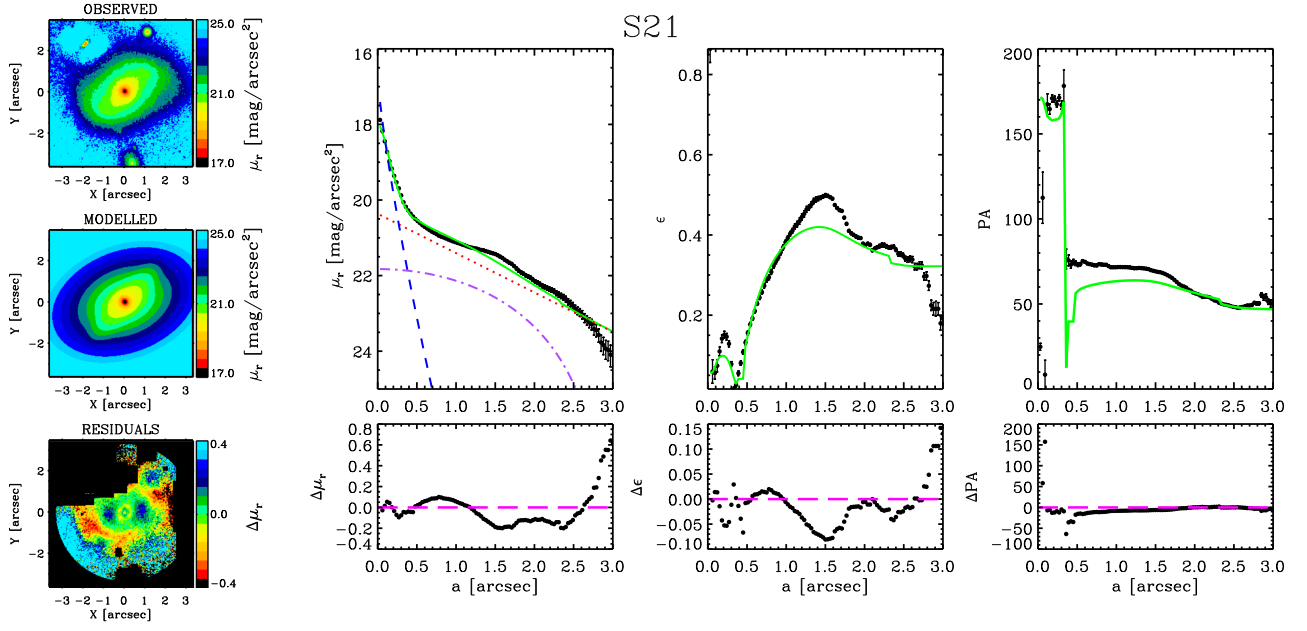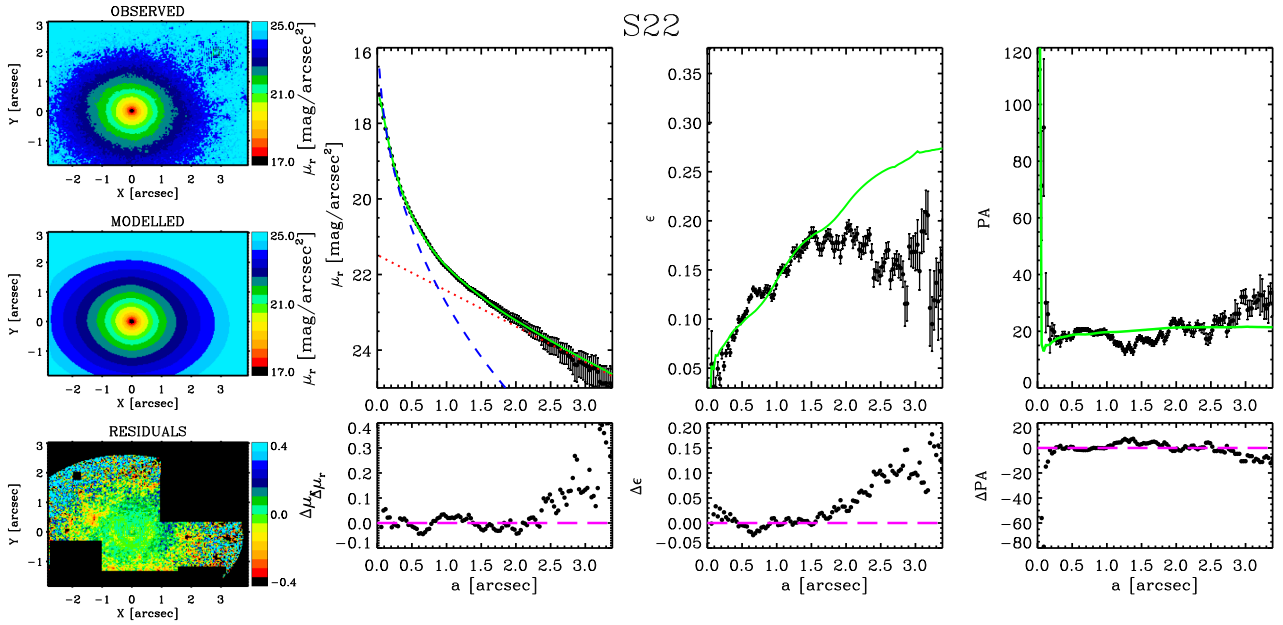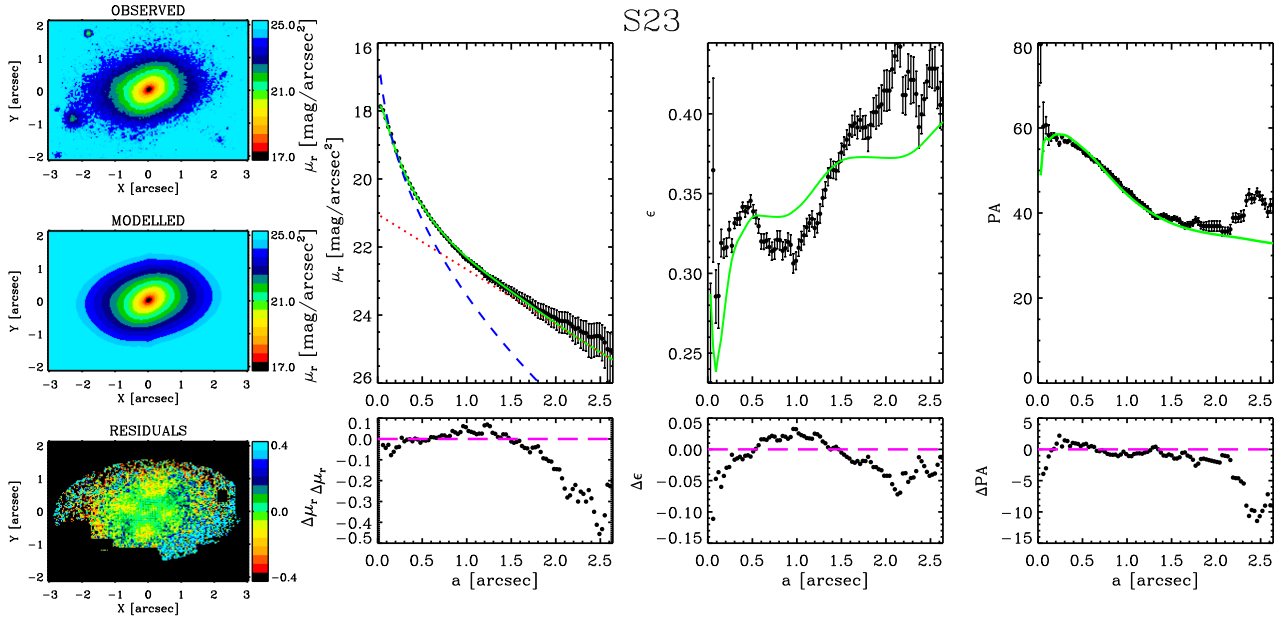**Figure A5.** As in Fig. A1 but for galaxy S05 fitted with a Sérsic model.

Figure A6. As in Fig. A1 but for galaxy S06 fitted with a Sérsic model.

Figure A7. As in Fig. A1 but for galaxy S07 (SeDisc model).

S08
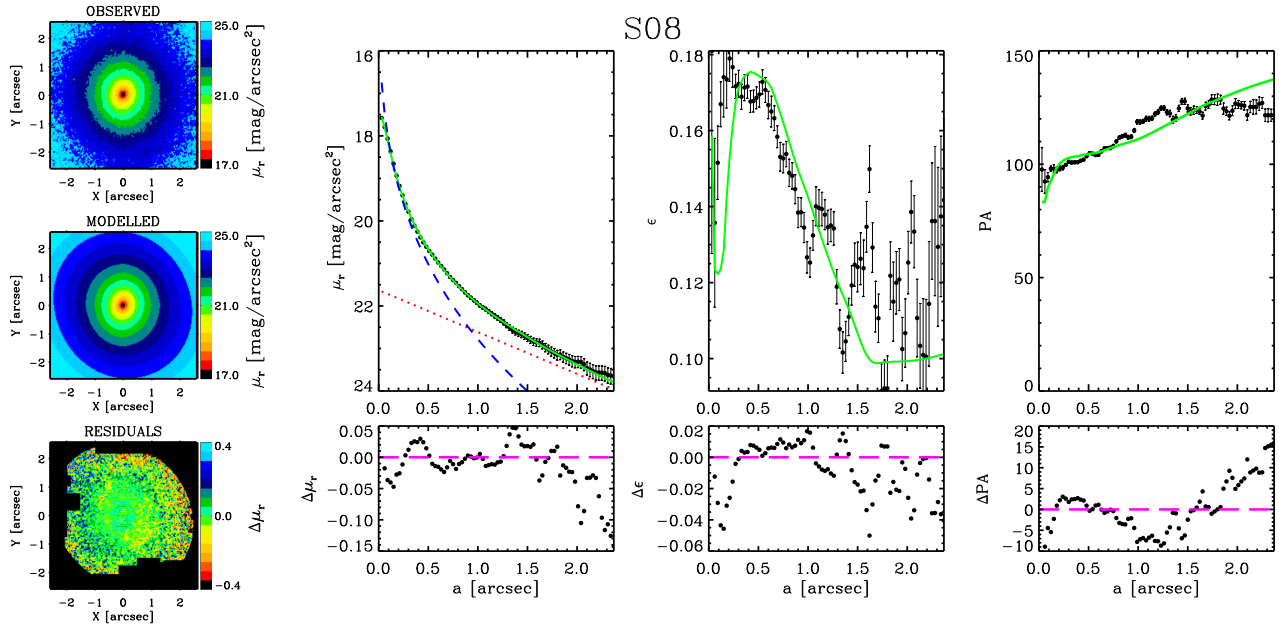
Figure A8. As in Fig. A1 but for galaxy S08 (SeDisc model).

S09
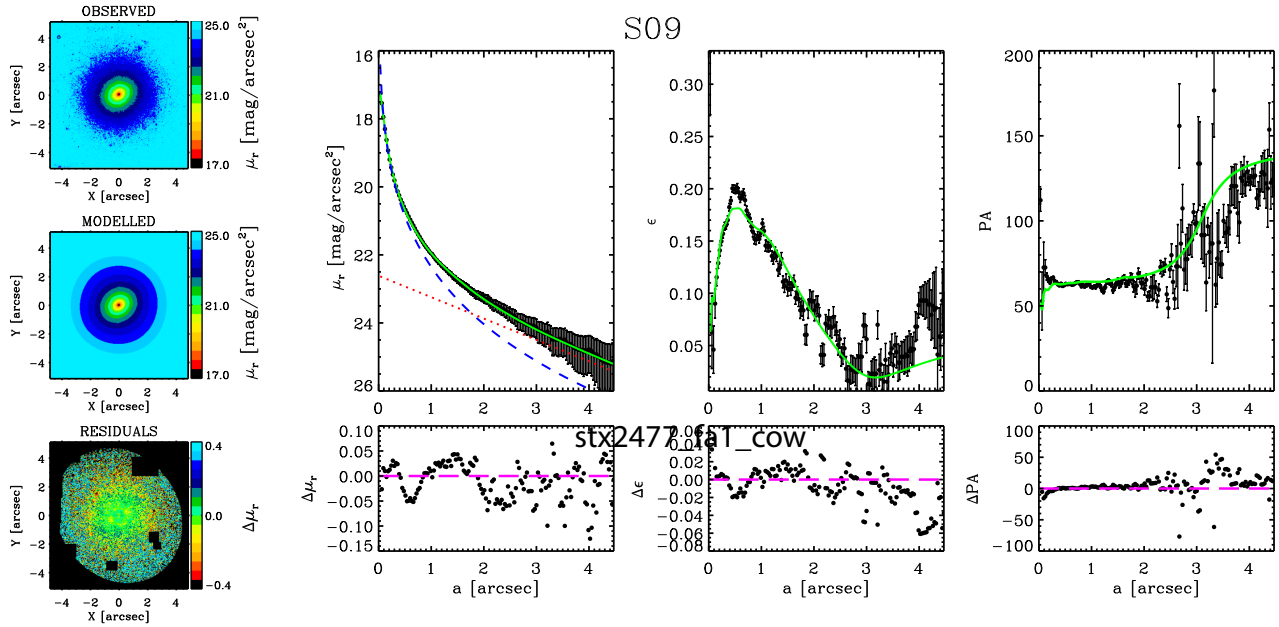
Figure A9. As in Fig. A1 but for galaxy S09 (SeDisc model).

Figure A10. As in Fig. A1 but for galaxy S10 (`SeDisc` model).

Figure A11. As in Fig. A1 but for galaxy S11 fitted with a `SeDisc` model.

Figure A12. As in Fig. A1 but for galaxy S12 fitted with a `SeDiBar` model. The dash-dotted purple line represents the intrinsic surface-brightness radial profile of the bar along its semi major axis.

Figure A13. As in Fig. A1 but for galaxy S13 (`SeDisc` model).

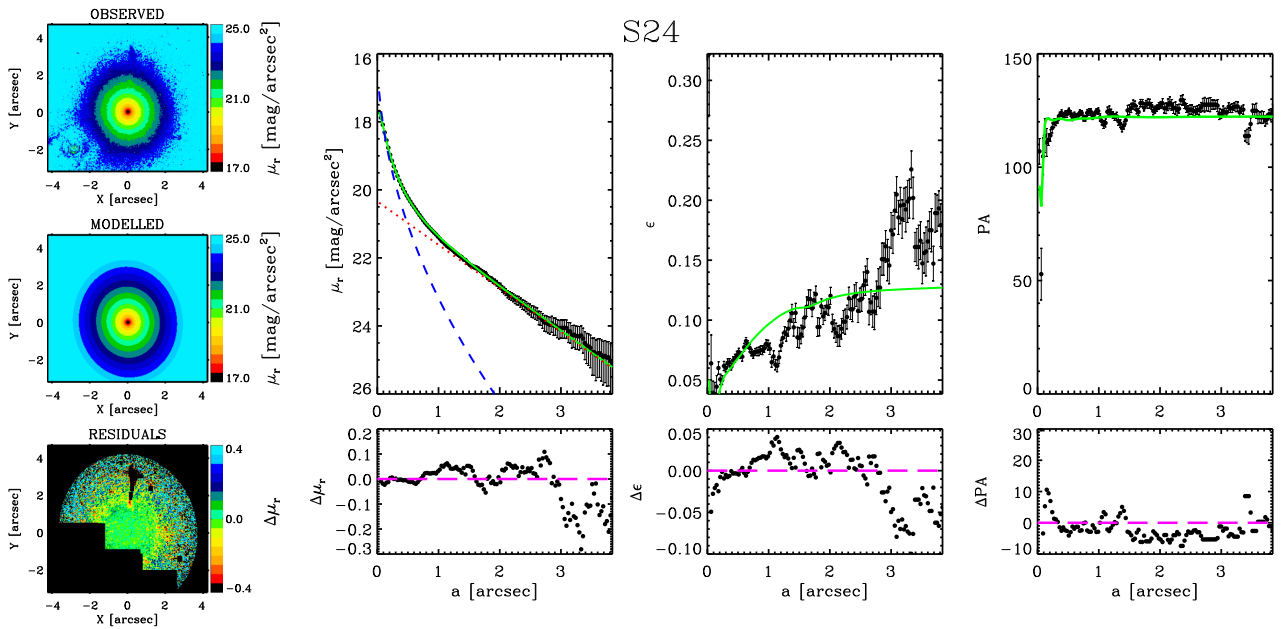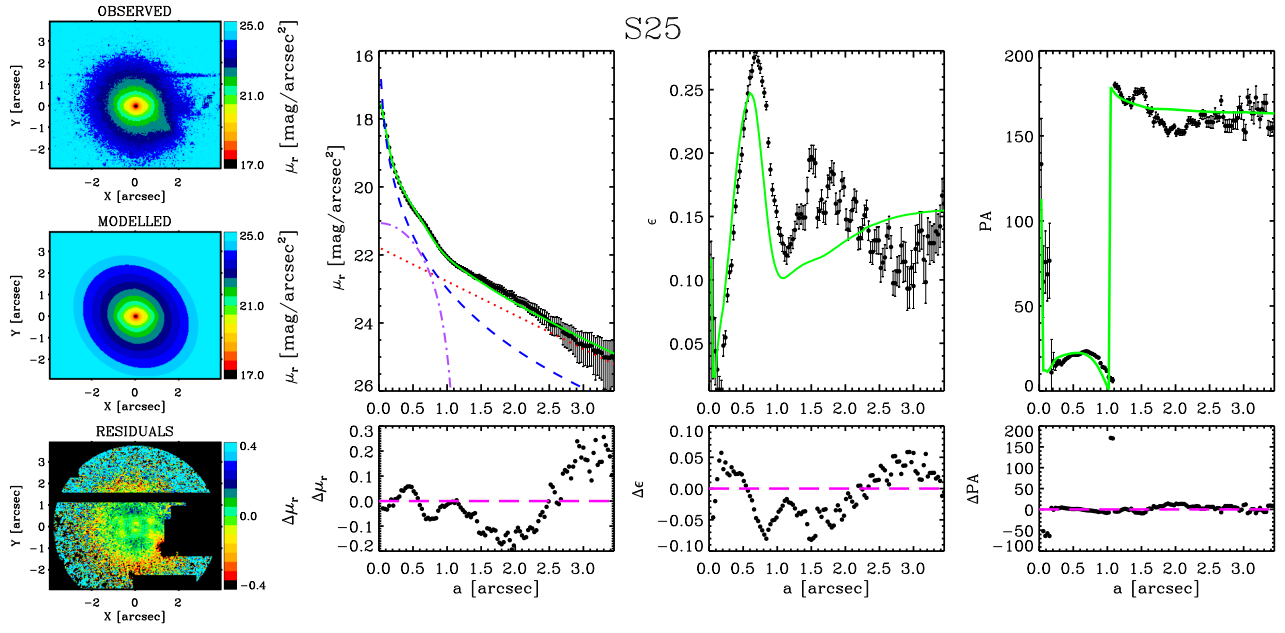**Figure A14.** As in Fig. A1 but for galaxy S14 (`SeDisc` model).

Figure A15. As in Fig. A1 but for galaxy S15 (`SeDiBar` model). The dash-dotted purple line represents the instrinsic surface-brightness radial profile of the bar along its semi major axis.

Figure A16. As in Fig. A1 but for galaxy S16 (SeDisc model).

Figure A17. As in Fig. A1 but for galaxy S18 (SeDisc model).

Figure A18. As in Fig. A1 but for galaxy S19 (`SeDisc` model).

Figure A19. As in Fig. A1 but for galaxy S20 fitted with a `SeDiBar` model. The dash-dotted purple line represents the intrinsic surface-brightness radial profile of the bar along its semi major axis.
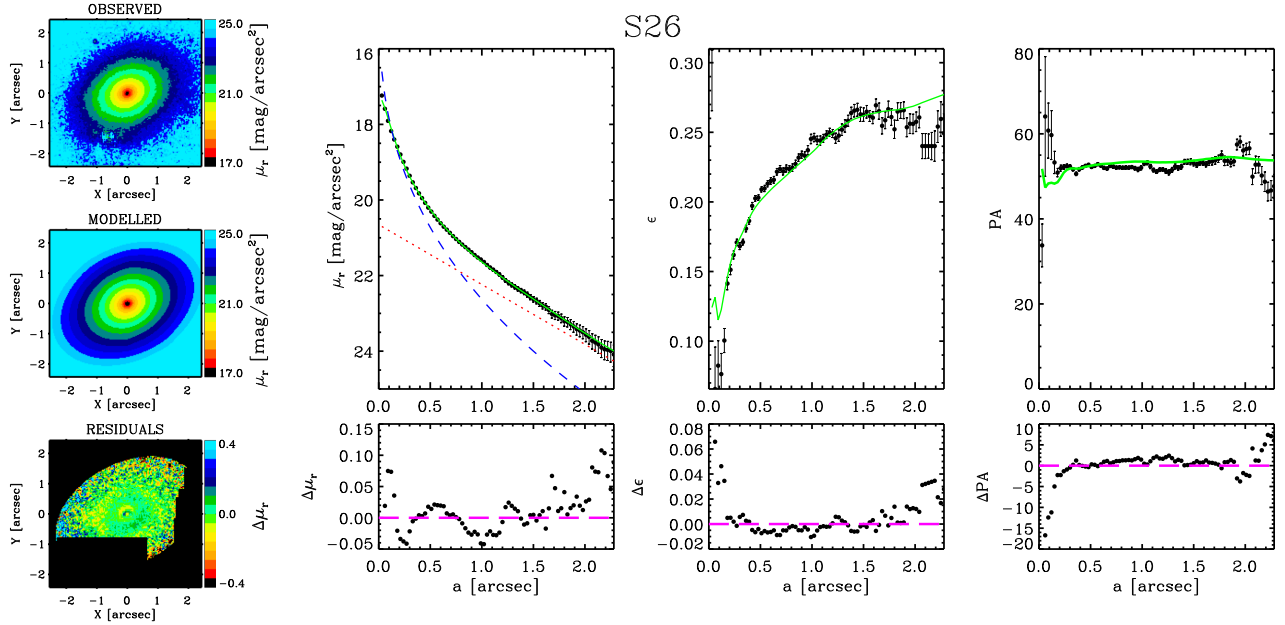
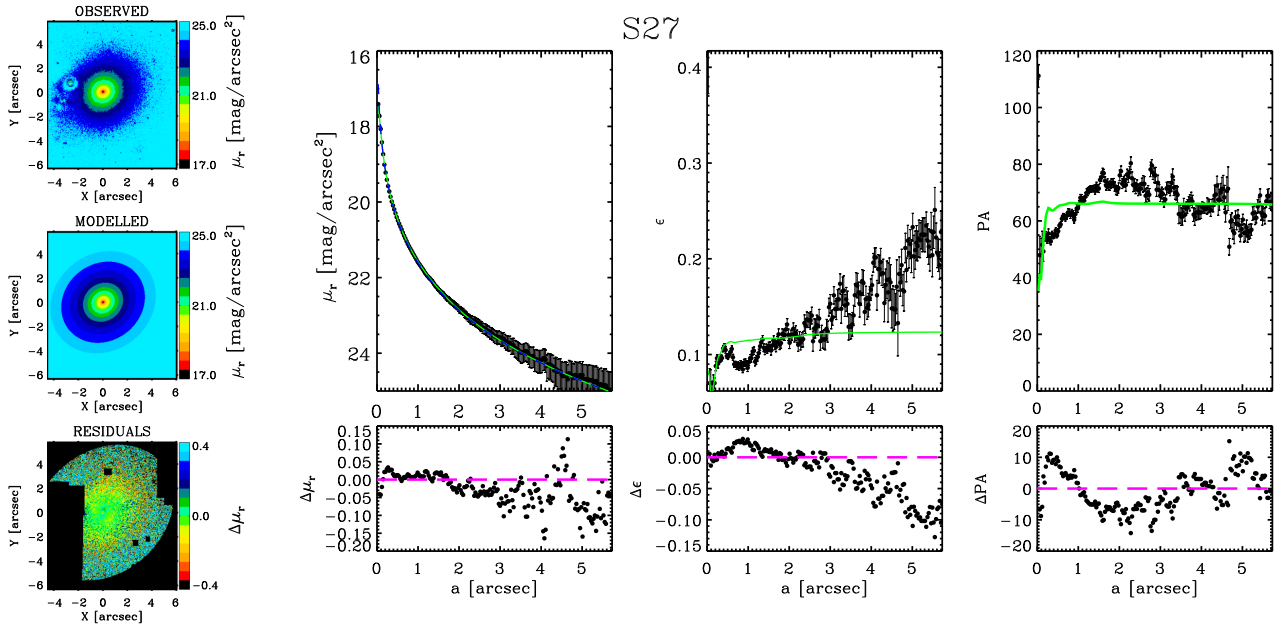**Figure A20.** As in Fig. A1 but for galaxy S21 fitted with a `SeDiBar` model. The dash-dotted purple line represents the intrinsic surface-brightness radial profile of the bar along its semi major axis.

Figure A21. As in Fig. A1 but for galaxy S22 (`SeDisc` model).
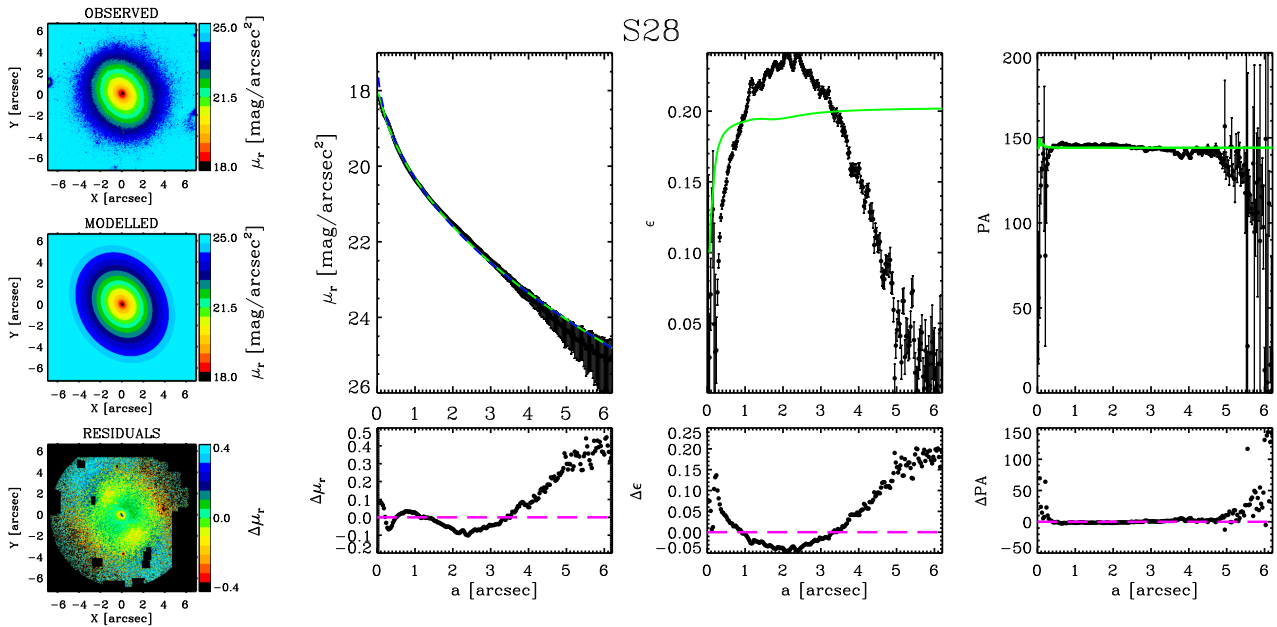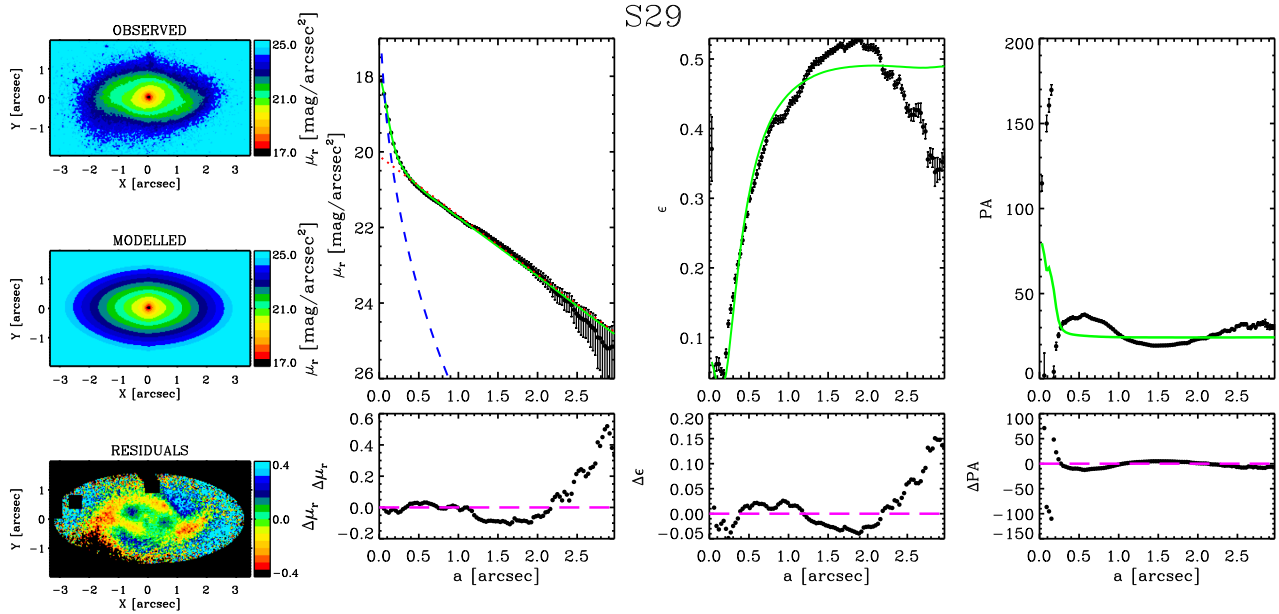
Figure A22. As in Fig. A1 but for galaxy S23 (SeDisc model).

Figure A23. As in Fig. A1 but for galaxy S24 (SeDisc model).

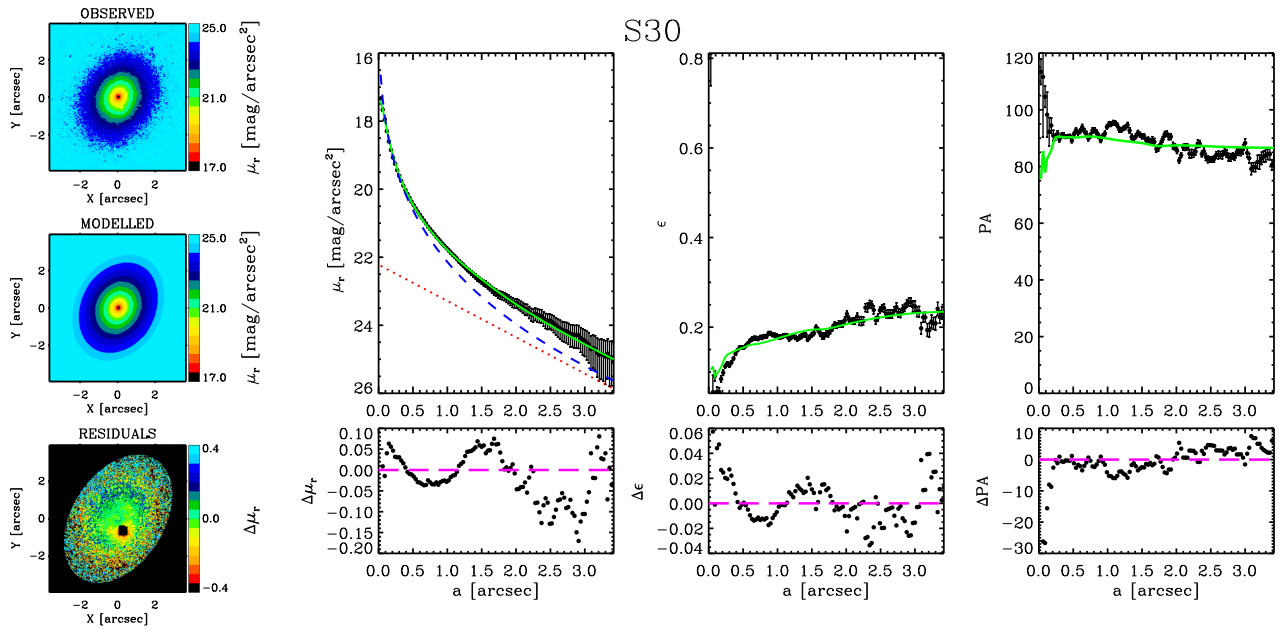**Figure A24.** As in Fig. A1 but for galaxy S25 fitted with a `SeDiBar` model. The dash-dotted purple line represents the intrinsic surface-brightness radial profile of the bar along its semi major axis.

Figure A25. As in Fig. A1 but for galaxy S26 (`SeDisc` model).

Figure A26. As in Fig. A1 but for galaxy S27 (Sérsic model).

Figure A27. As in Fig. A1 but for galaxy S28 fitted with a Sérsic model.

Figure A28. As in Fig. A1 but for galaxy S29 (`SeDisc` model).

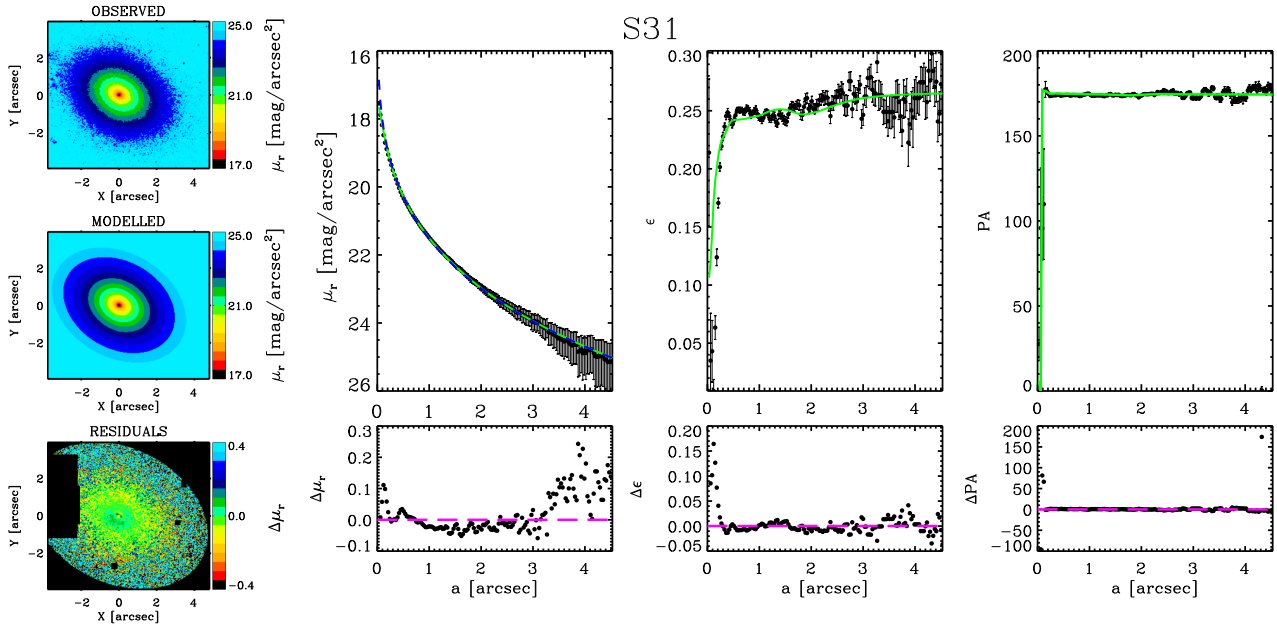**Figure A29.** As in Fig. A1 but for galaxy S30 (`SeDisc` model).

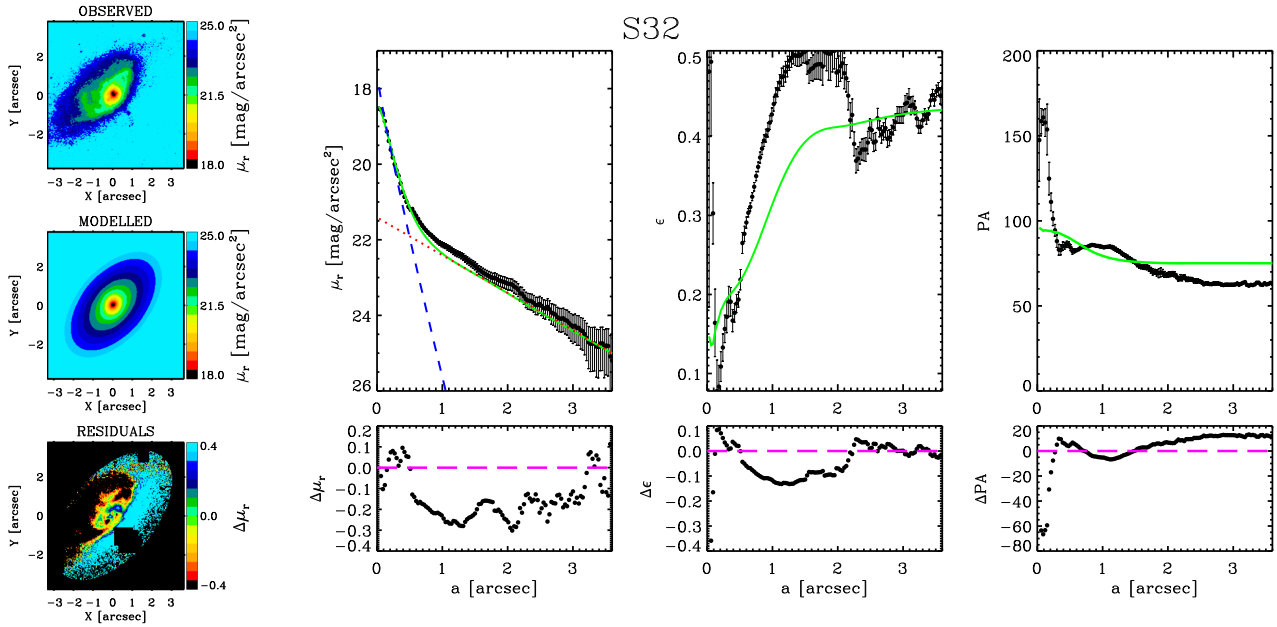**Figure A30.** As in Fig. A1 but for galaxy S31 fitted with a Sérsic model.

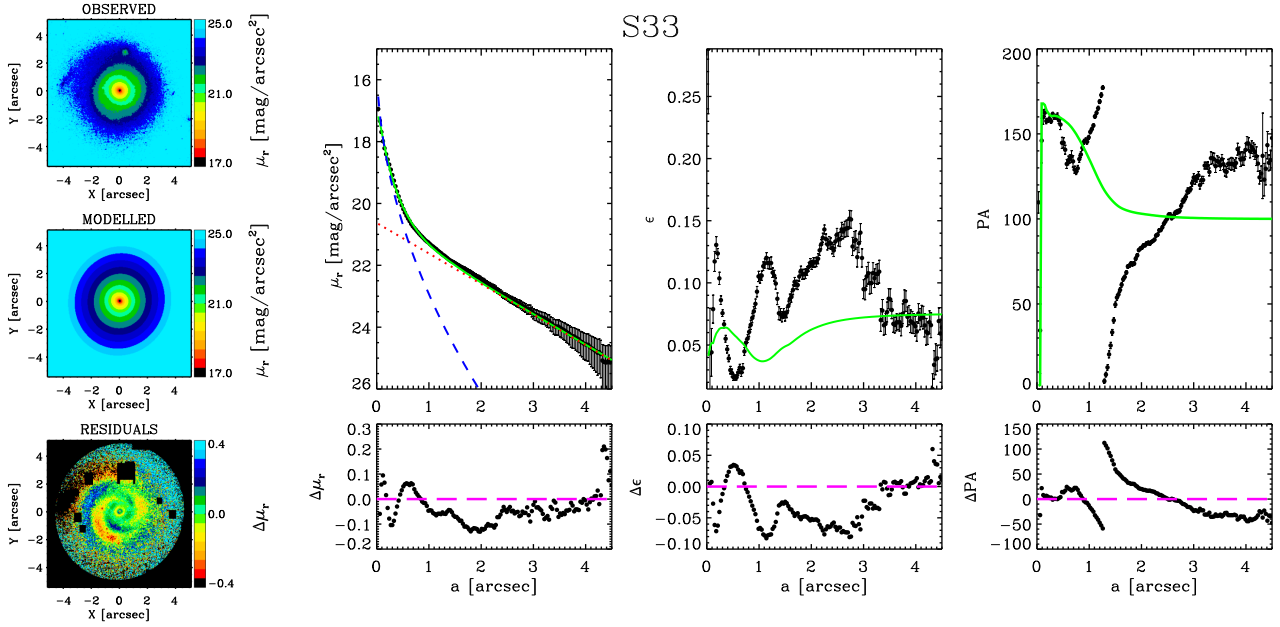**Figure A31.** As in Fig. A1 but for galaxy S32 (SeDisc model).

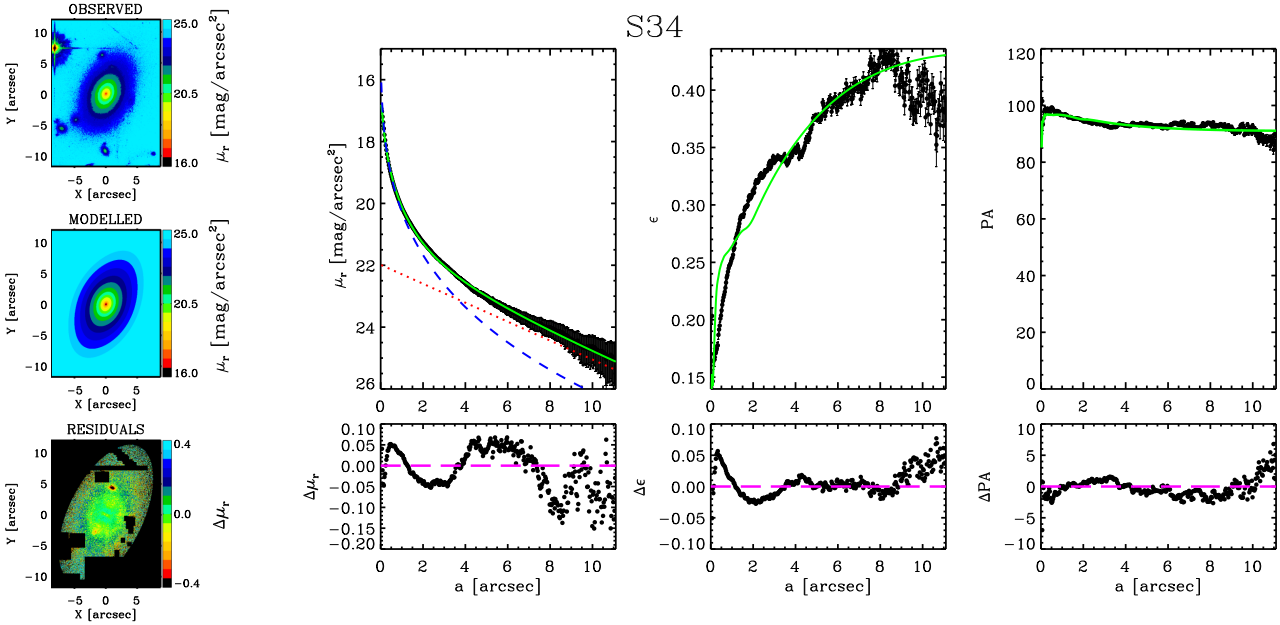**Figure A32.** As in Fig. A1 but for galaxy S33 (SeDisc model).

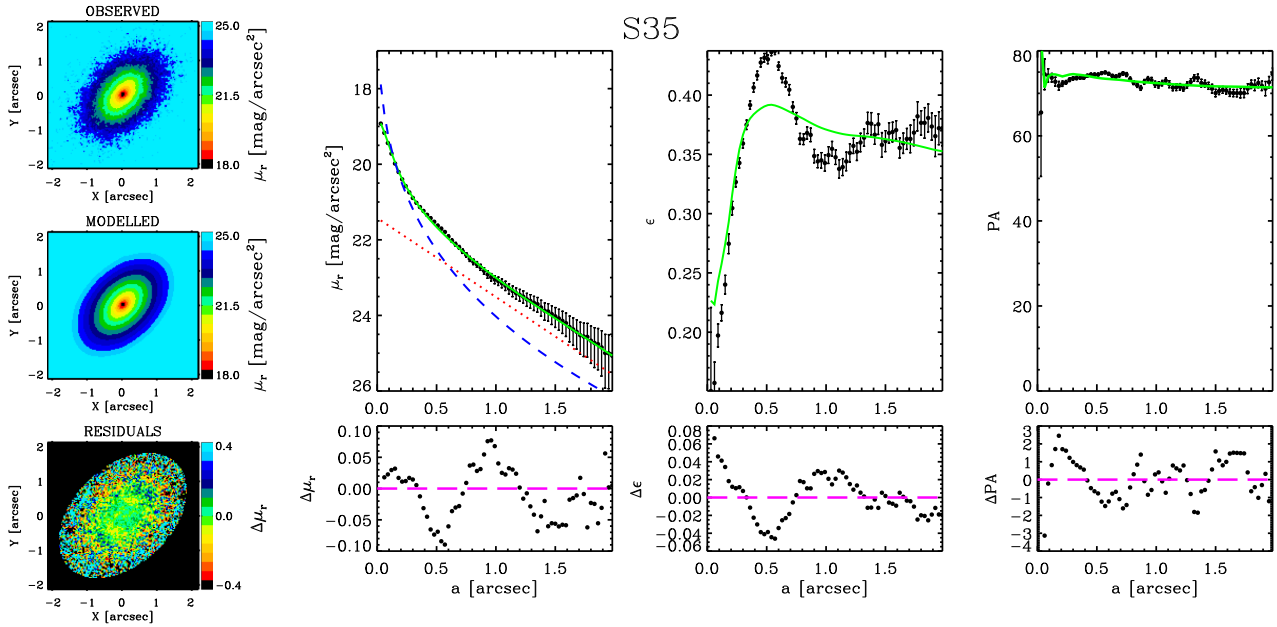**Figure A33.** As in Fig. A1 but for galaxy S34 (SeDisc model).

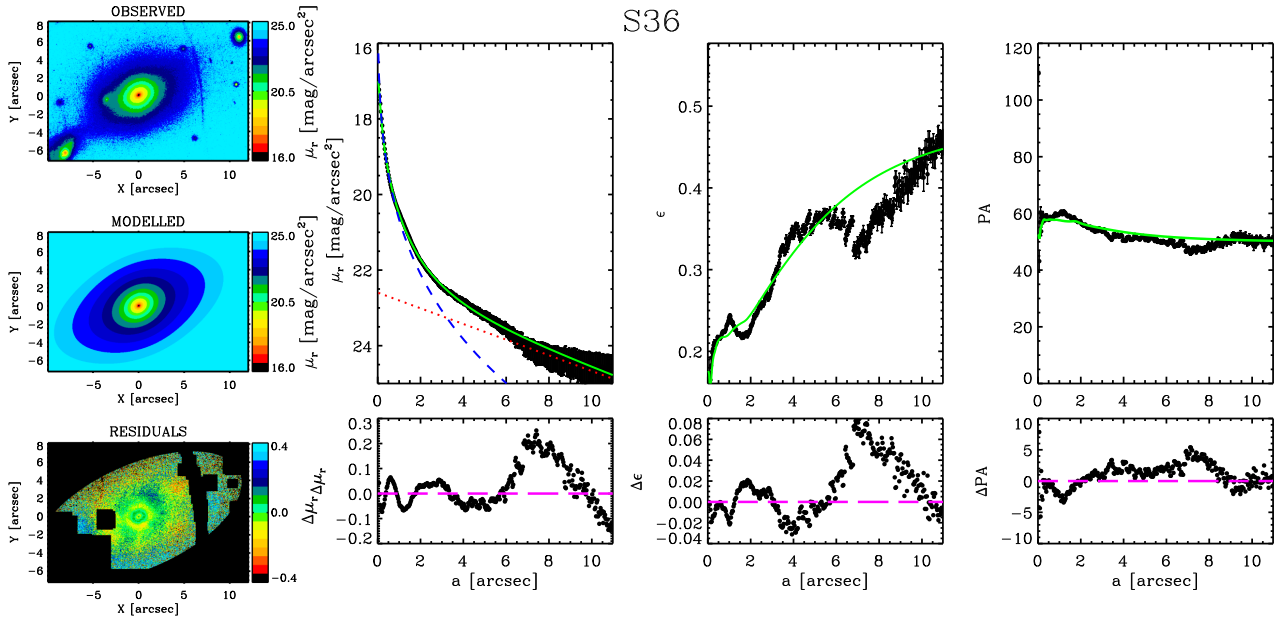**Figure A34.** As in Fig. A1 but for galaxy S35 (`SeDisc` model).

Figure A35. As in Fig. A1 but for galaxy S36 (`SeDisc` model).

Figure A36. As in Fig. A1 but for galaxy S37 (`SeDiBar` model). The dash-dotted purple line represents the intrinsic surface-brightness radial profile of the bar along its semi major axis.

Figure A37. As in Fig. A1 but for galaxy S38 (`SeDisc` model).

Figure A38. As in Fig. A1 but for galaxy S39 fitted with a `SeDiBar` model. The dash-dotted purple line represents the intrinsic surface-brightness radial profile of the bar along its semi major axis.

Figure A39. As in Fig. A1 but for galaxy S40 (`SeDisc` model).

Figure A40. As in Fig. A1 but for galaxy S41 (SeDisc model).

Figure A41. As in Fig. A1 but for galaxy S42 (SeDisc model).
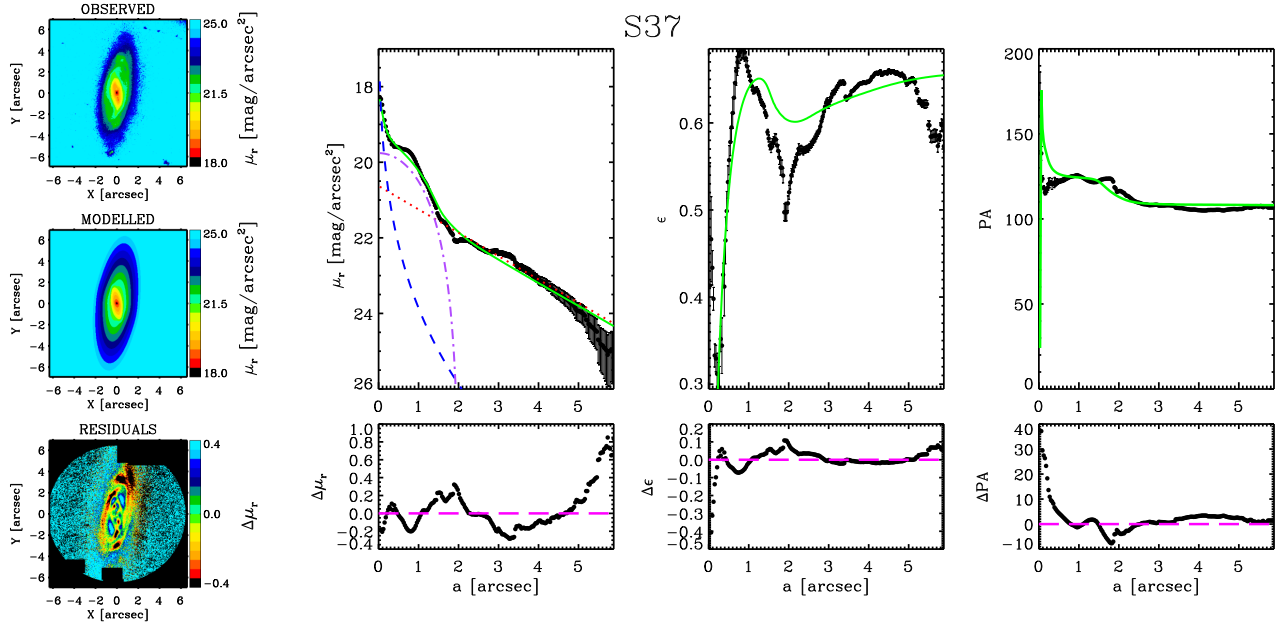
Figure A42. As in Fig. A1 but for galaxy S43 fitted with a `SeDiBar` model. The dash-dotted purple line represents the intrinsic surface-brightness radial profile of the bar along its semi major axis.

Figure A43. As in Fig. A1 but for galaxy S44 (`SeDisc` model).

S45

Figure A44. As in Fig. A1 but for galaxy S45 (`SeDisc` model).

S46

Figure A45. As in Fig. A1 but for galaxy S46 (`SeDisc` model).

Figure A46. As in Fig. A1 but for galaxy S47 (`SeDisc` model).

Figure A47. As in Fig. A1 but for galaxy S48 fitted with a `SeDiBar` model. The dash-dotted purple line represents the intrinsic surface-brightness radial profile of the bar along its semi major axis.
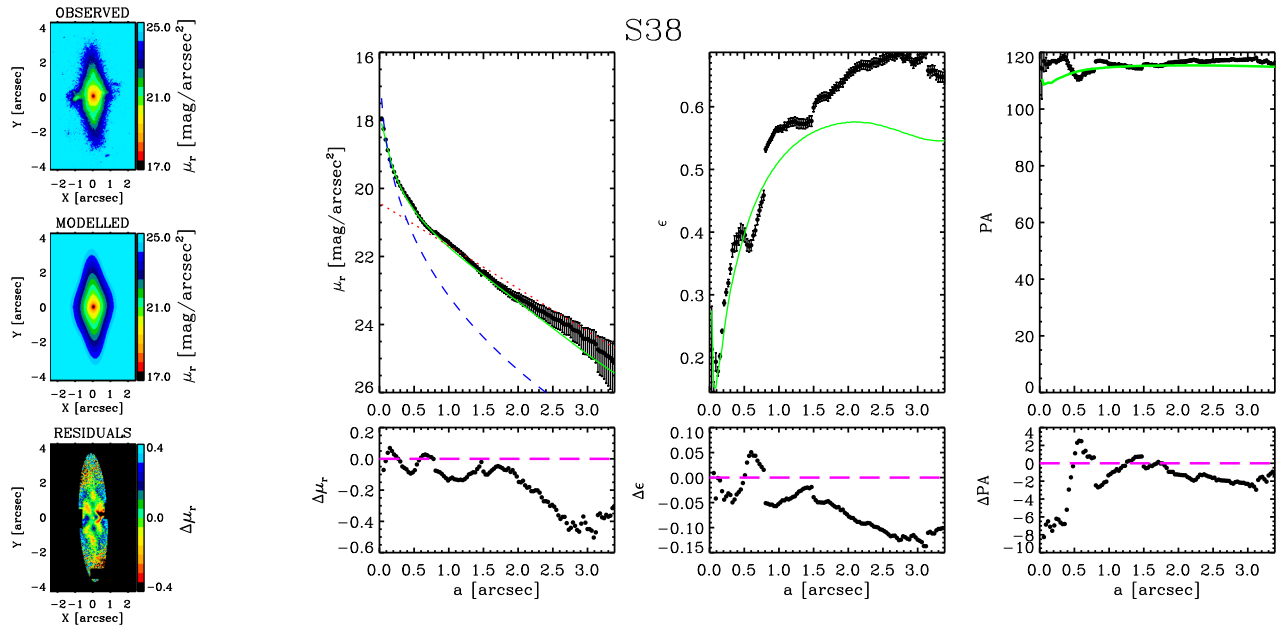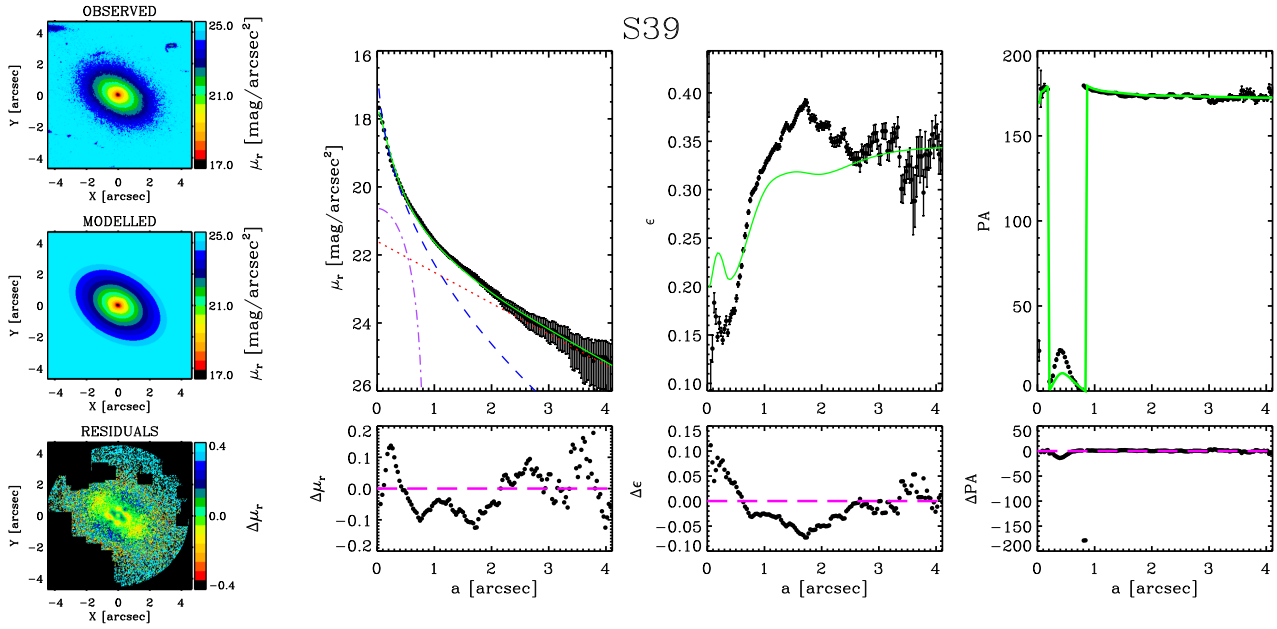
S49
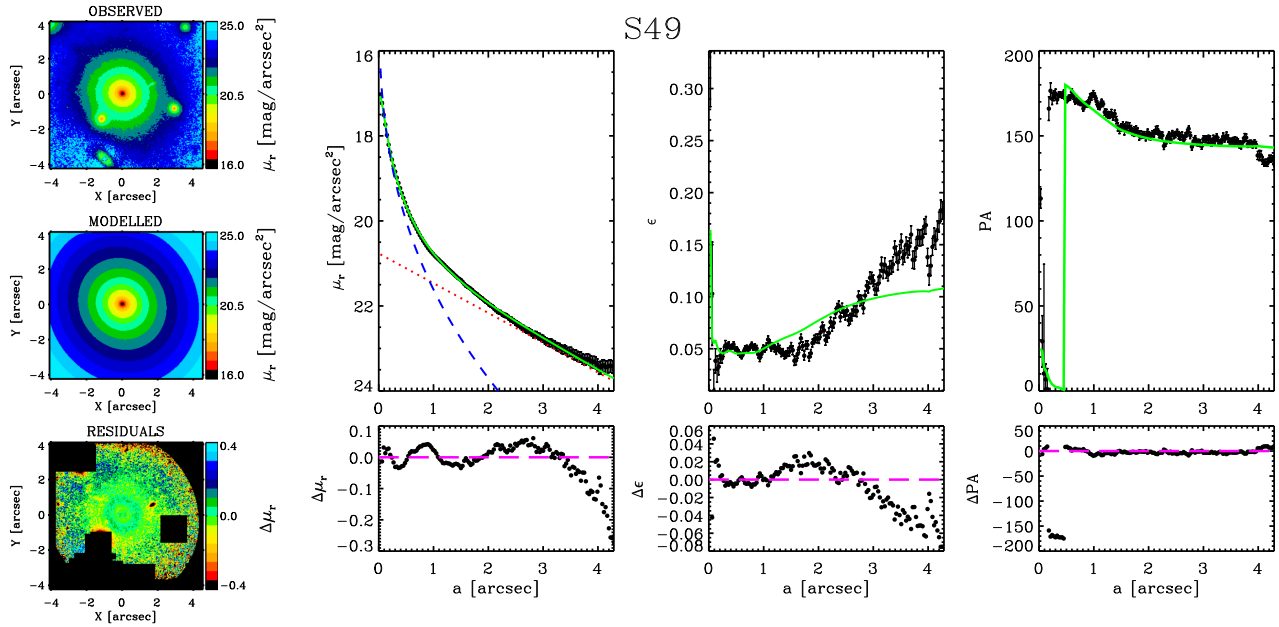
Figure A48. As in Fig. A1 but for galaxy S49 (`SeDisc` model).

S50
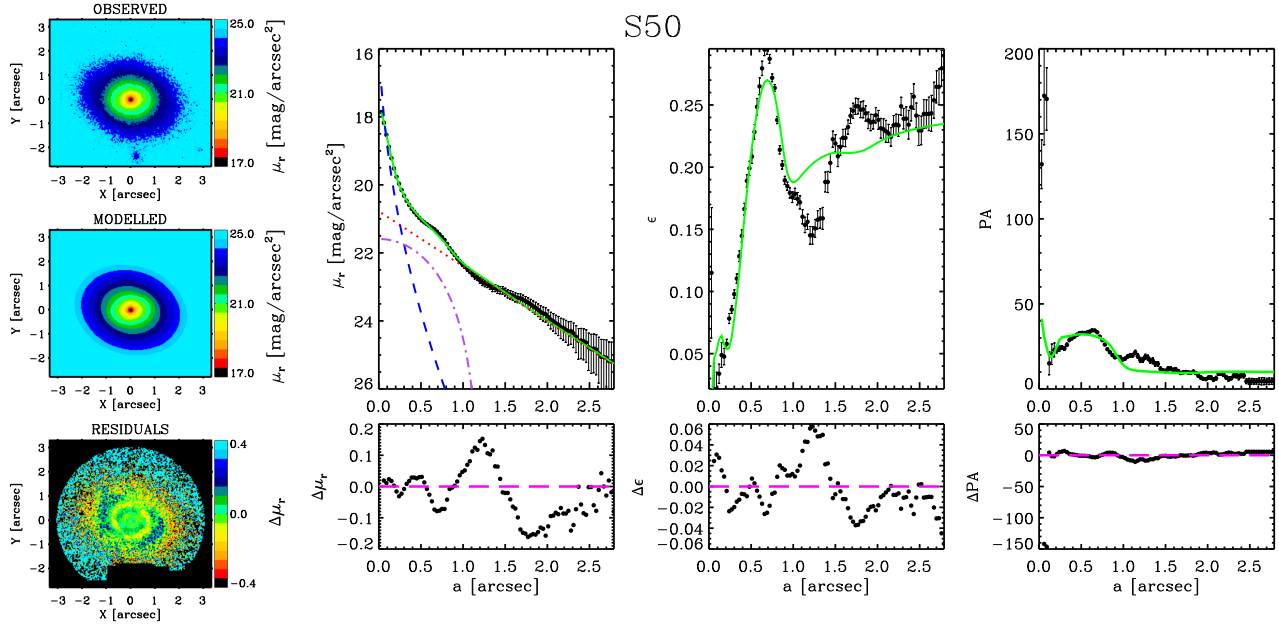
Figure A49. As in Fig. A1 but for galaxy S50 fitted with a `SeDiBar` model. The dash-dotted purple line represents the intrinsic surface-brightness radial profile of the bar along its semi major axis.
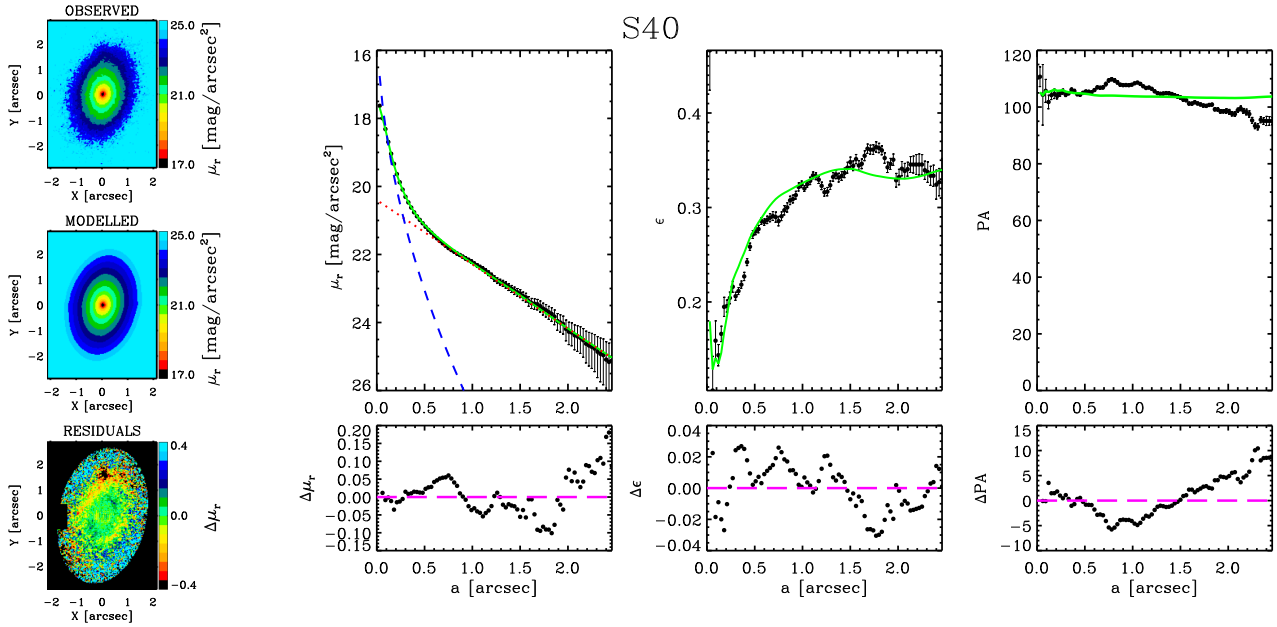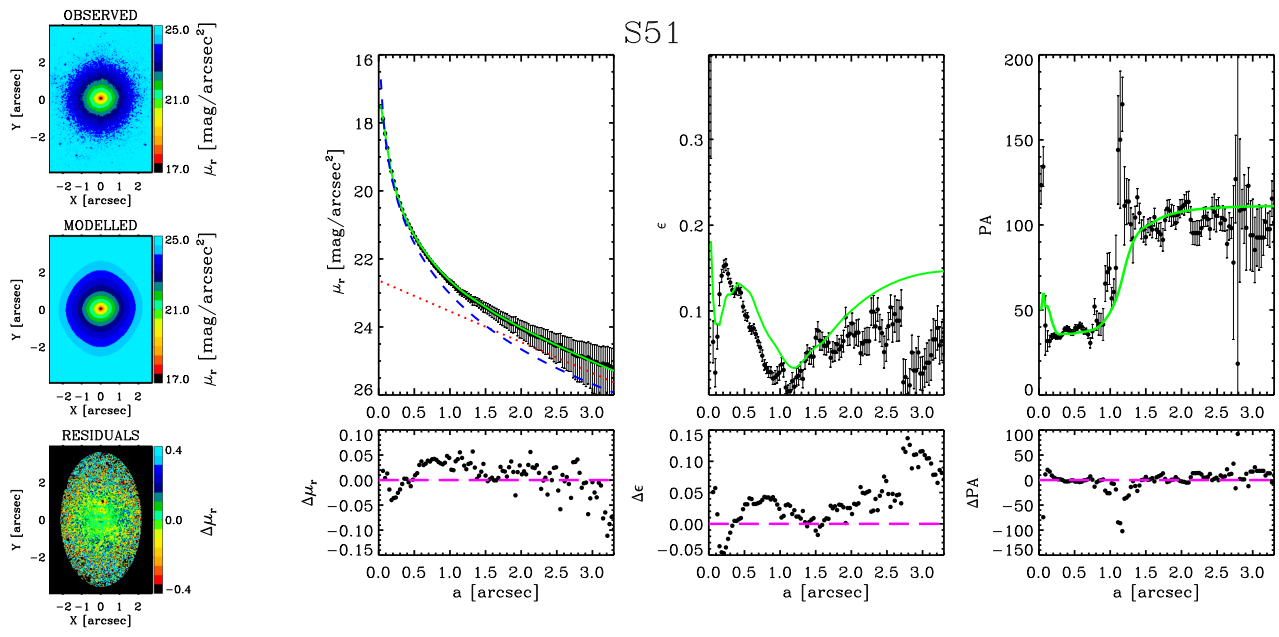
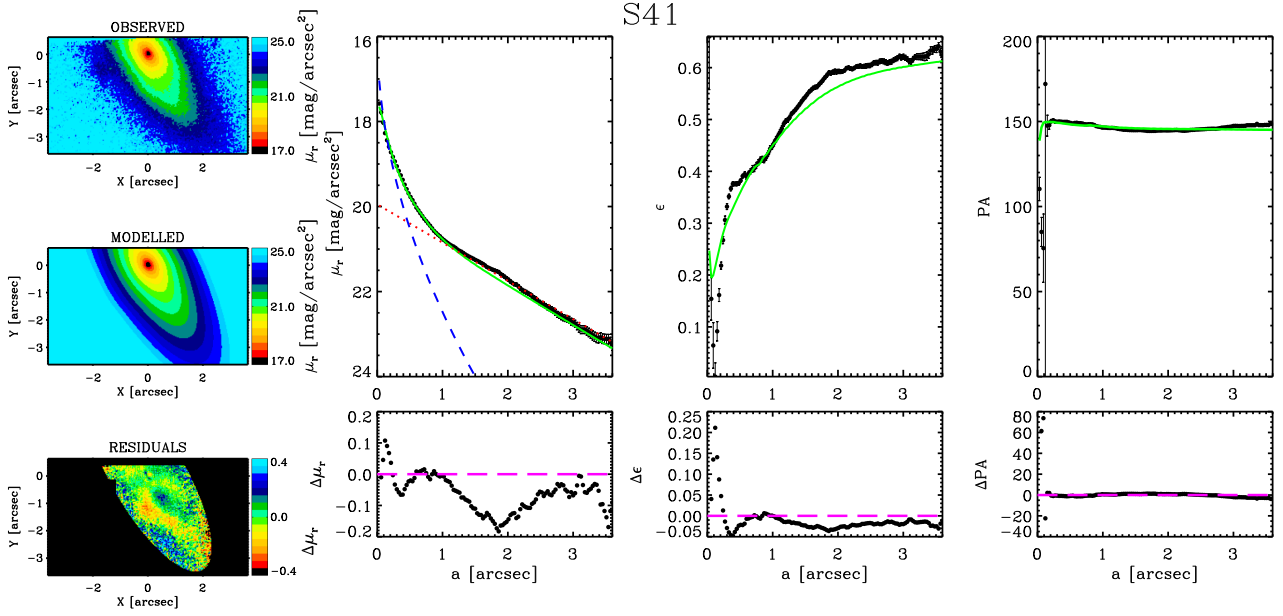**Figure A50.** As in Fig. A1 but for galaxy S51 (SeDisc model).
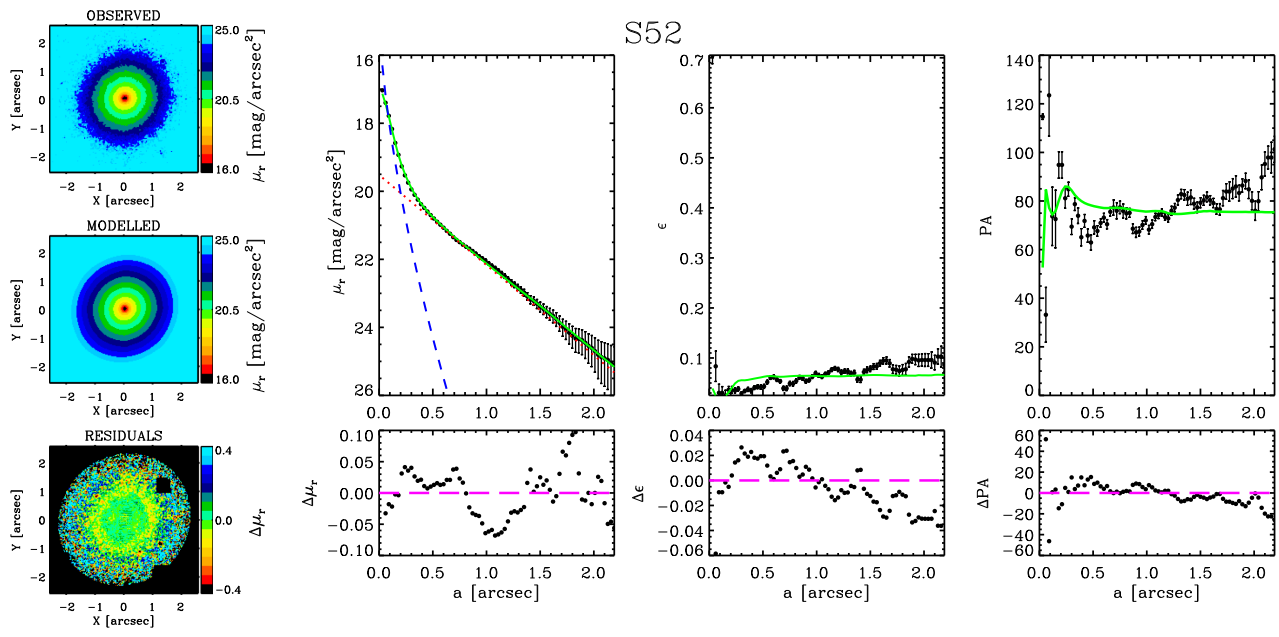
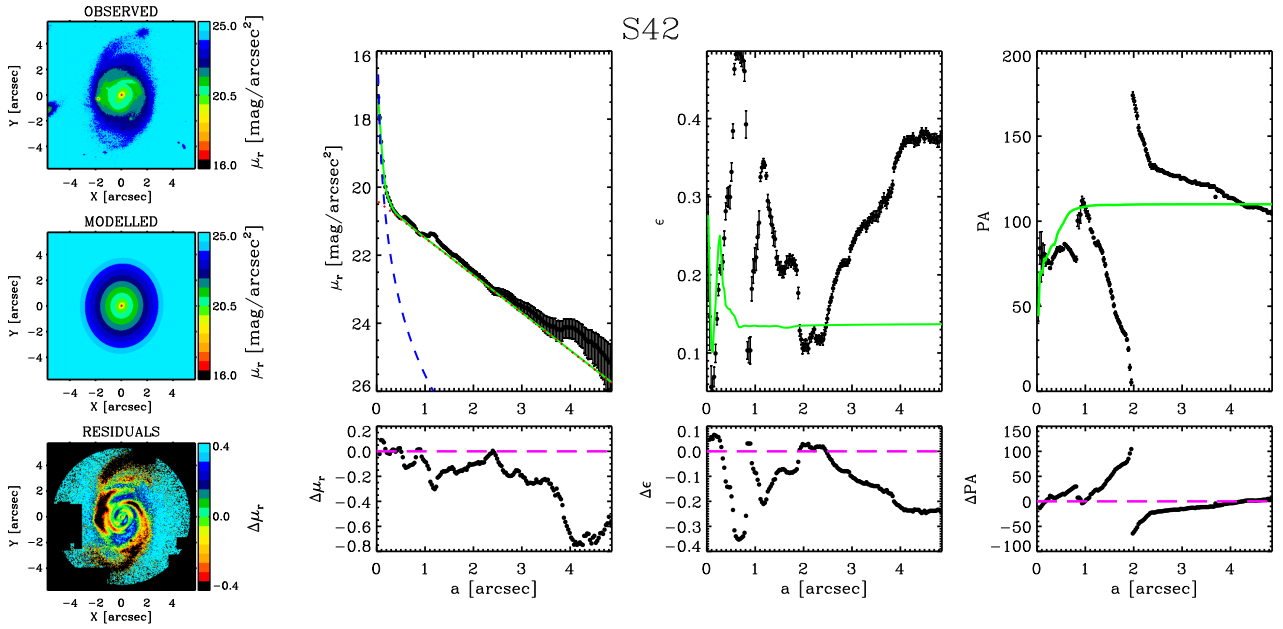**Figure A51.** As in Fig. A1 but for galaxy S52 (SeDisc model).
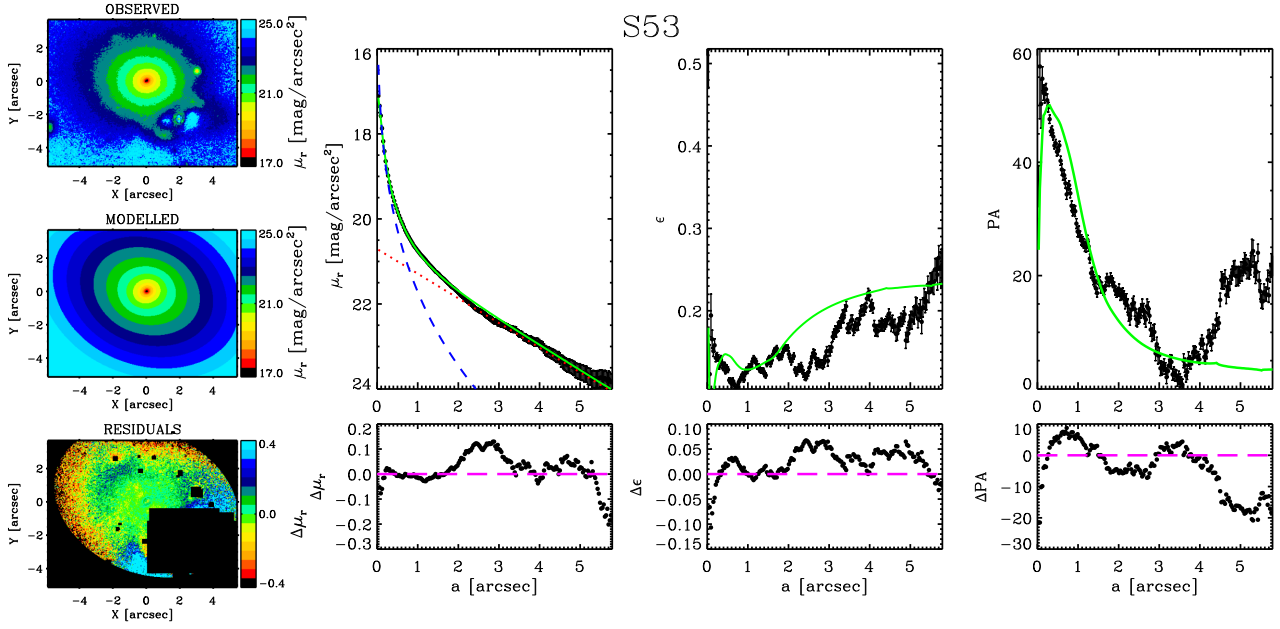
Figure A52. As in Fig. A1 but for galaxy S53 (SeDisc model).
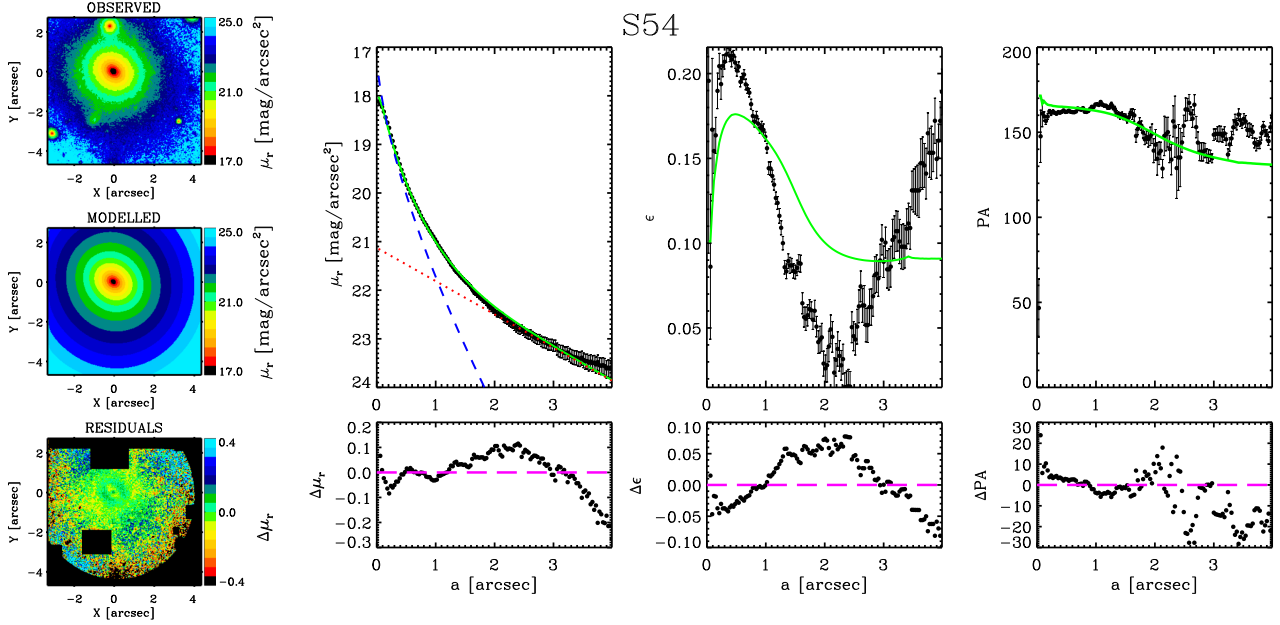
Figure A53. As in Fig. A1 but for galaxy S54 (SeDisc model).
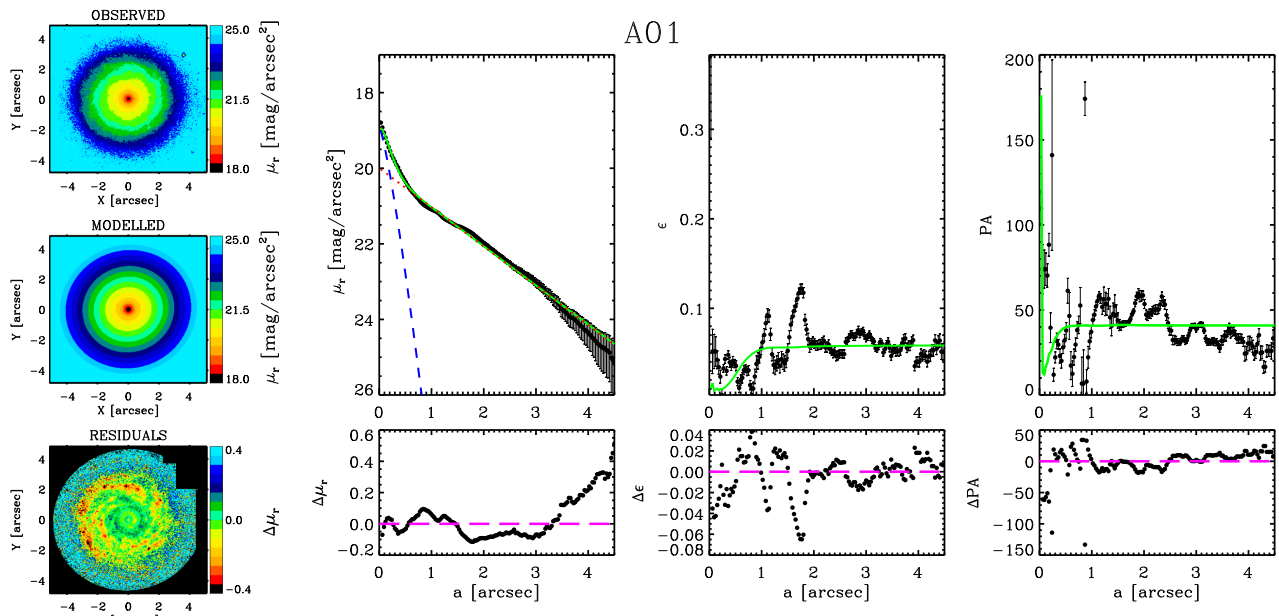
Figure A54. As in Fig. A1 but for galaxy A01 (`SeDisc` model).
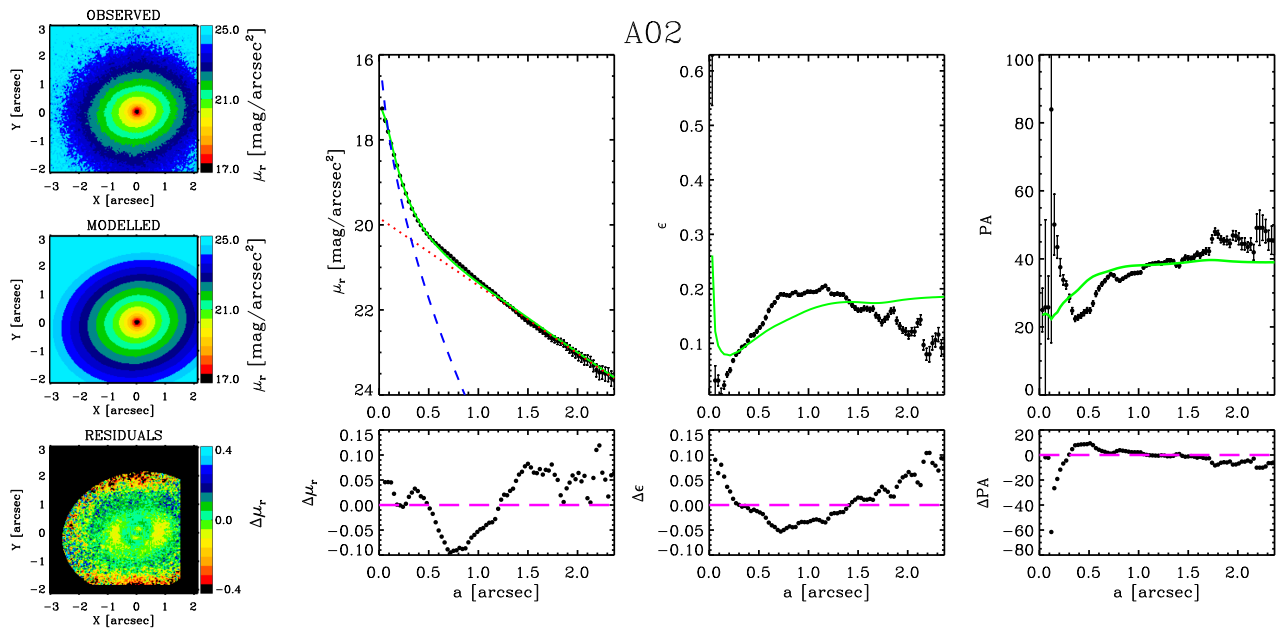
Figure A55. As in Fig. A1 but for galaxy A02 (`SeDisc` model).

A03
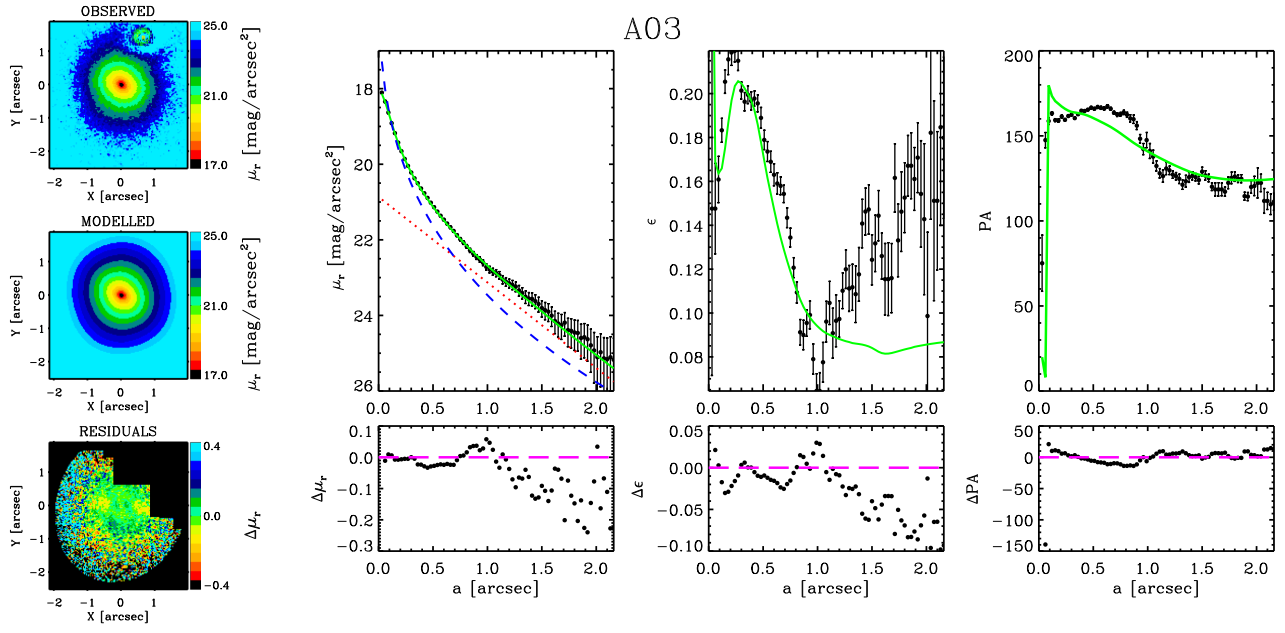
Figure A56. As in Fig. A1 but for galaxy A03 (SeDisc model).

A04
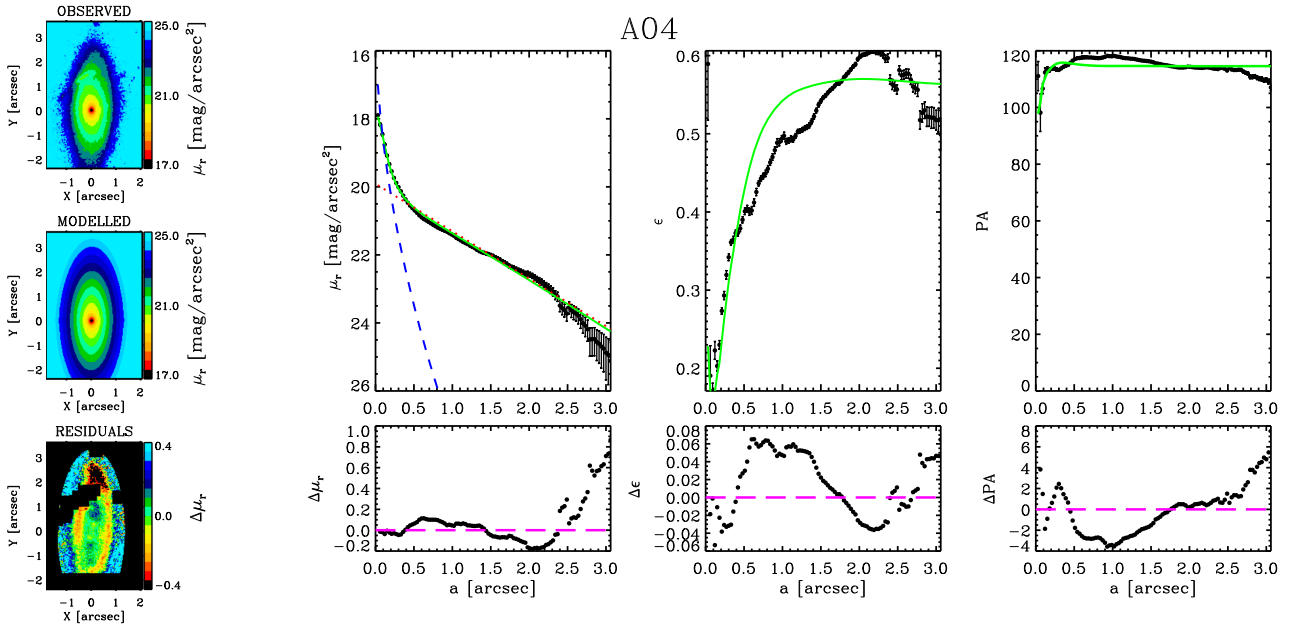
Figure A57. As in Fig. A1 but for galaxy A04 (SeDisc model).
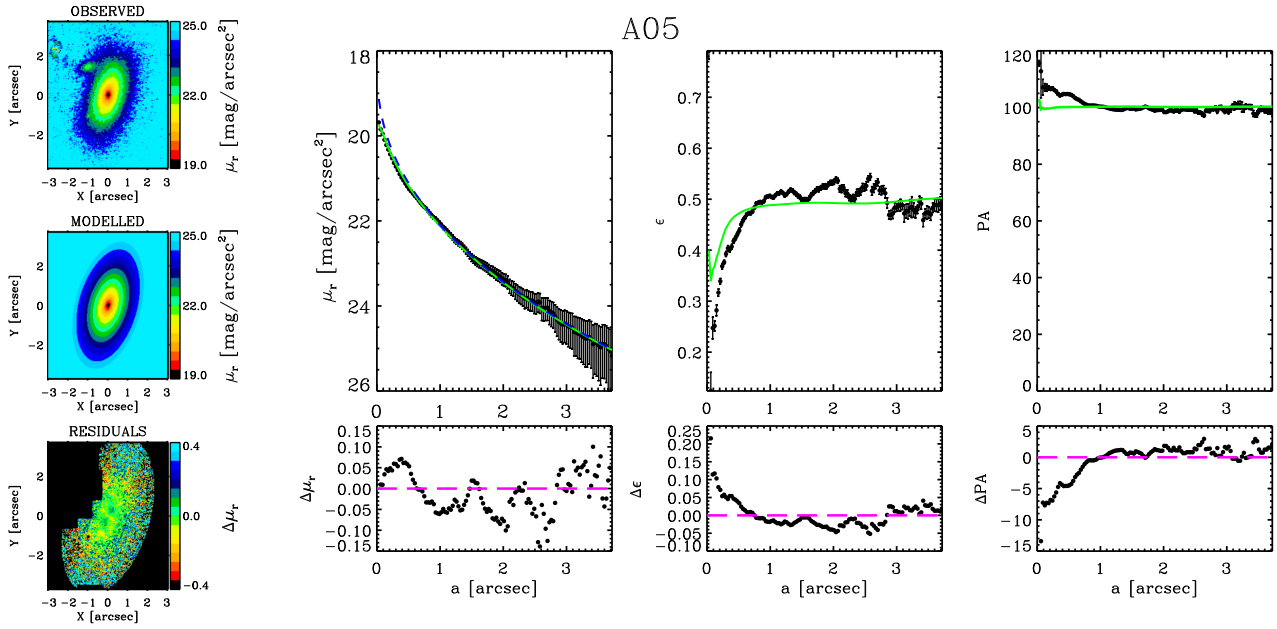
Figure A58. As in Fig. A1 but for galaxy A05 fitted with a Sérsic model.
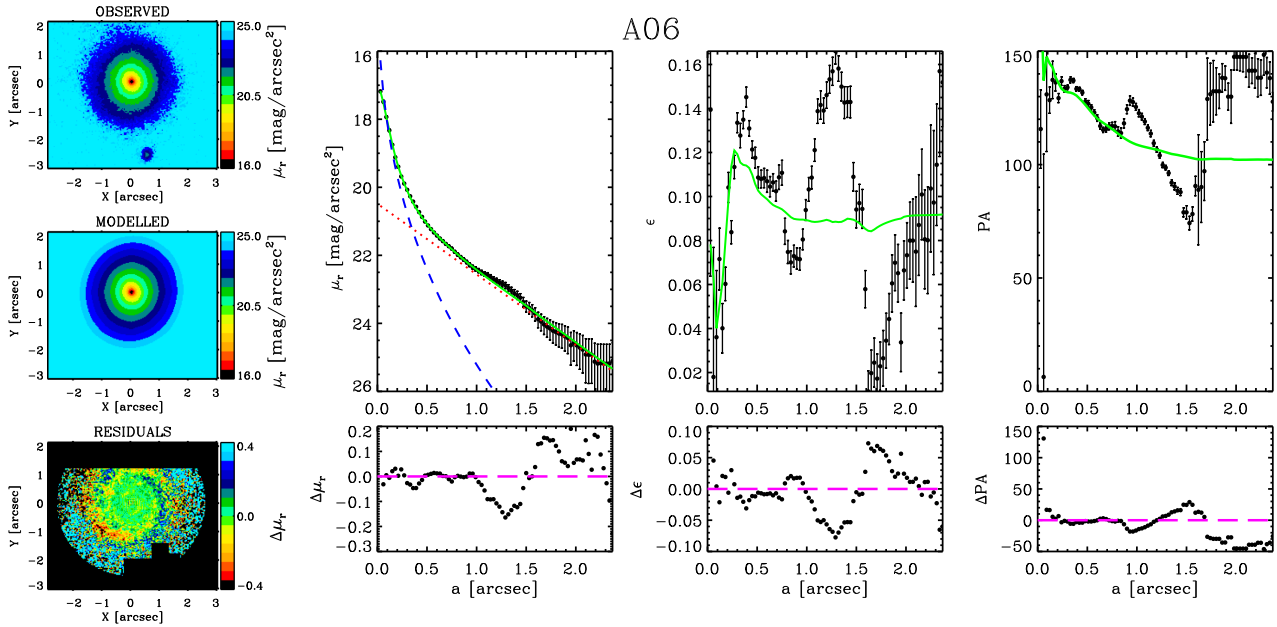
Figure A59. As in Fig. A1 but for galaxy A06 (SeDisc model).

Figure A60. As in Fig. A1 but for galaxy A07 (`SeDisc` model).

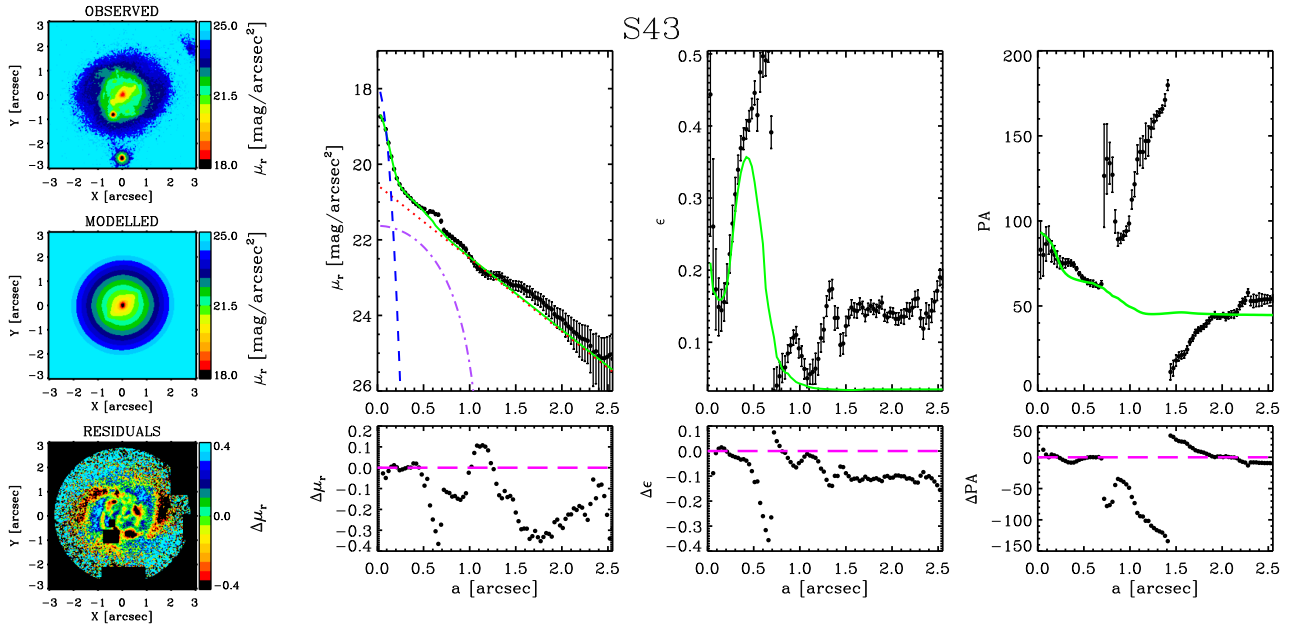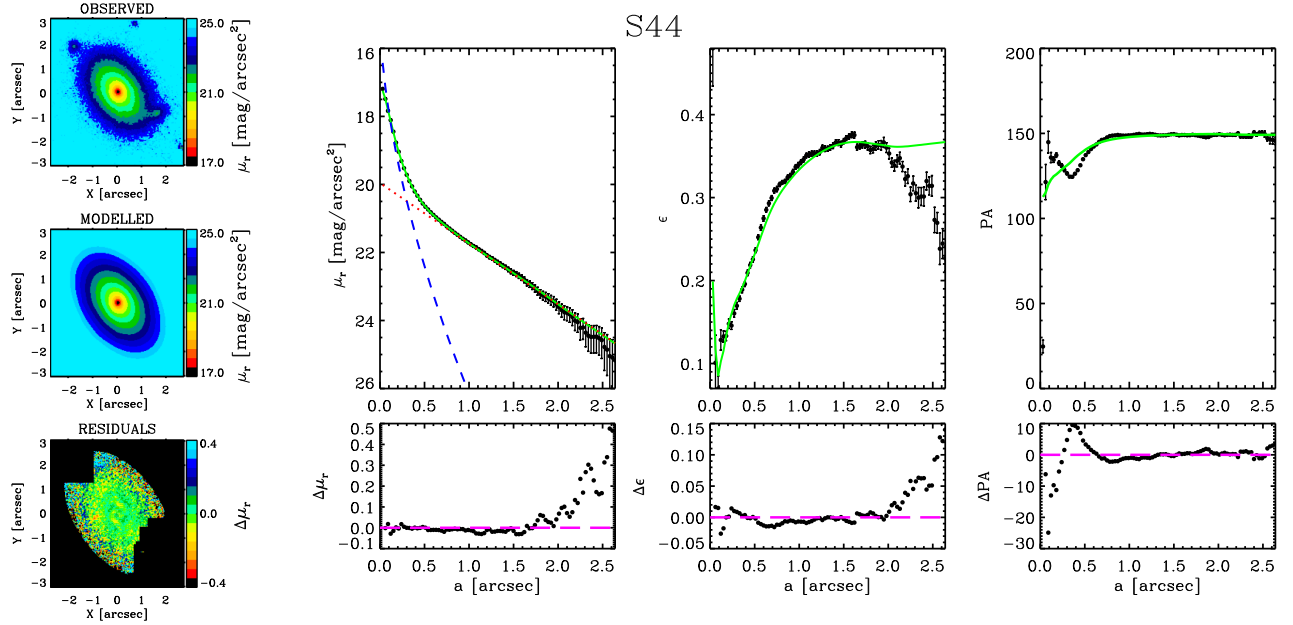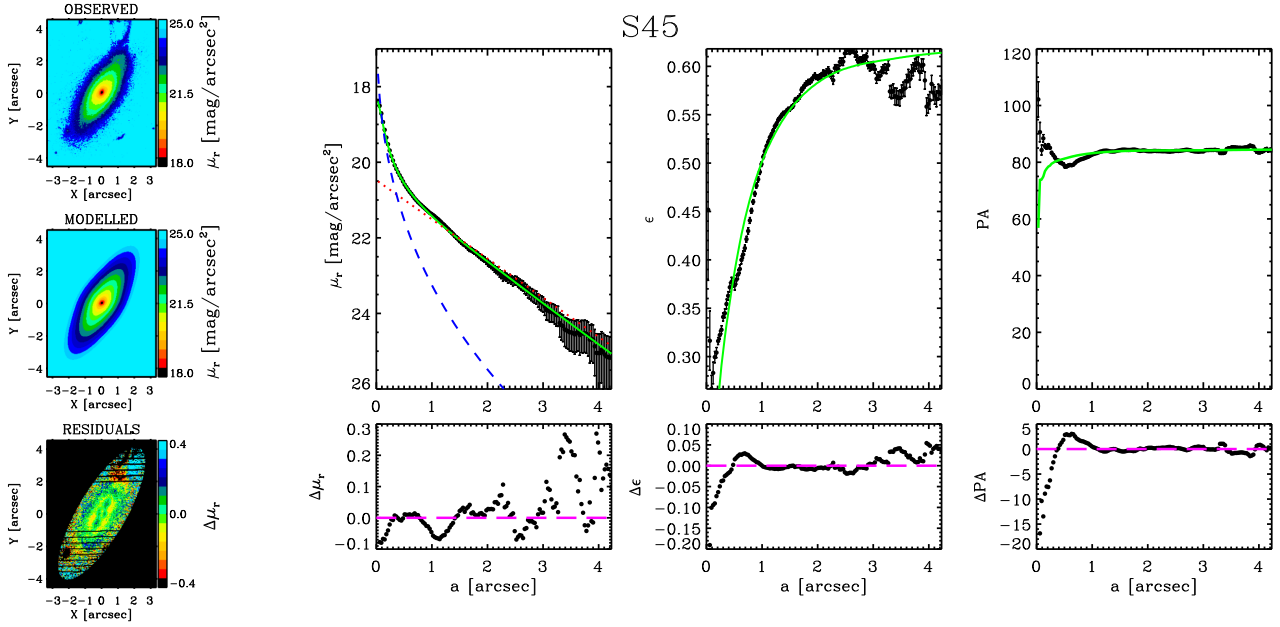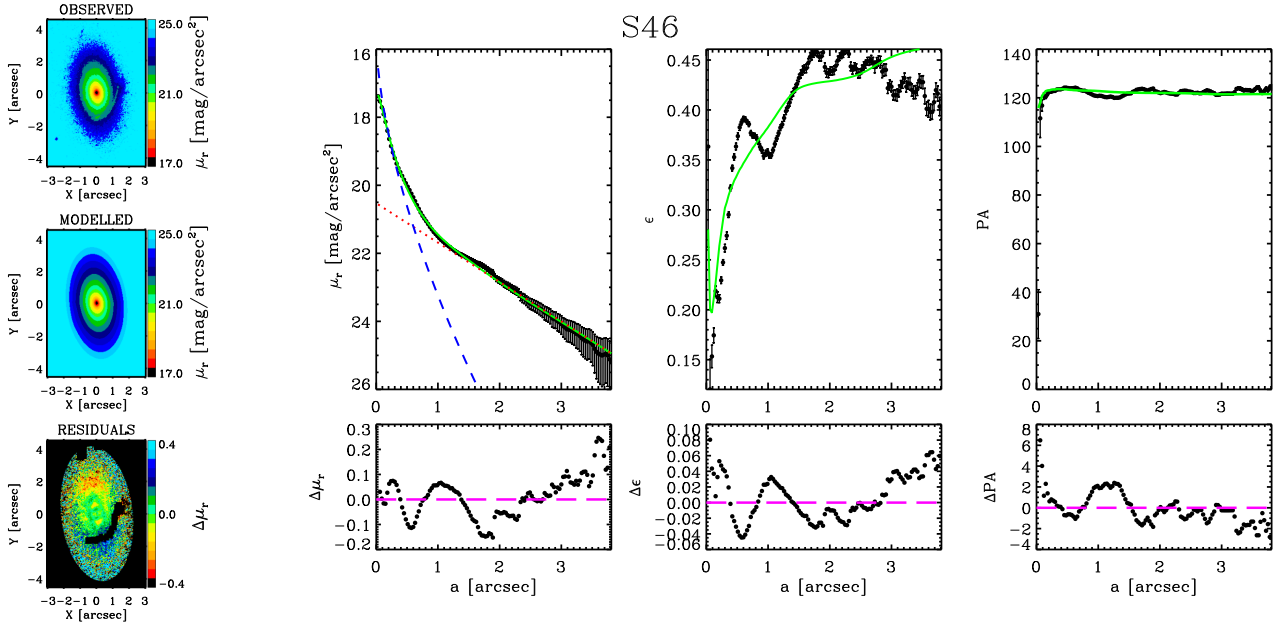**Figure A61.** As in Fig. A1 but for galaxy A08 (`SeDisc` model).

Figure A62. As in Fig. A1 but for galaxy A09 fitted with a Sérsic model.

Figure A63. As in Fig. A1 but for galaxy A10 (SeDisc model).

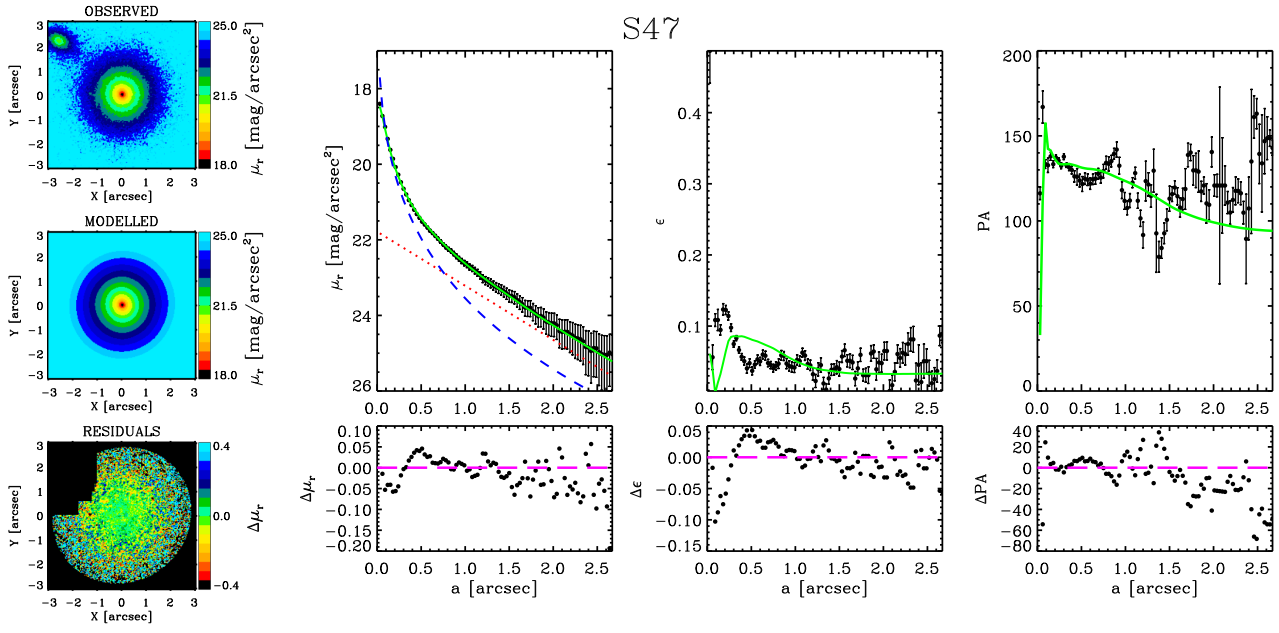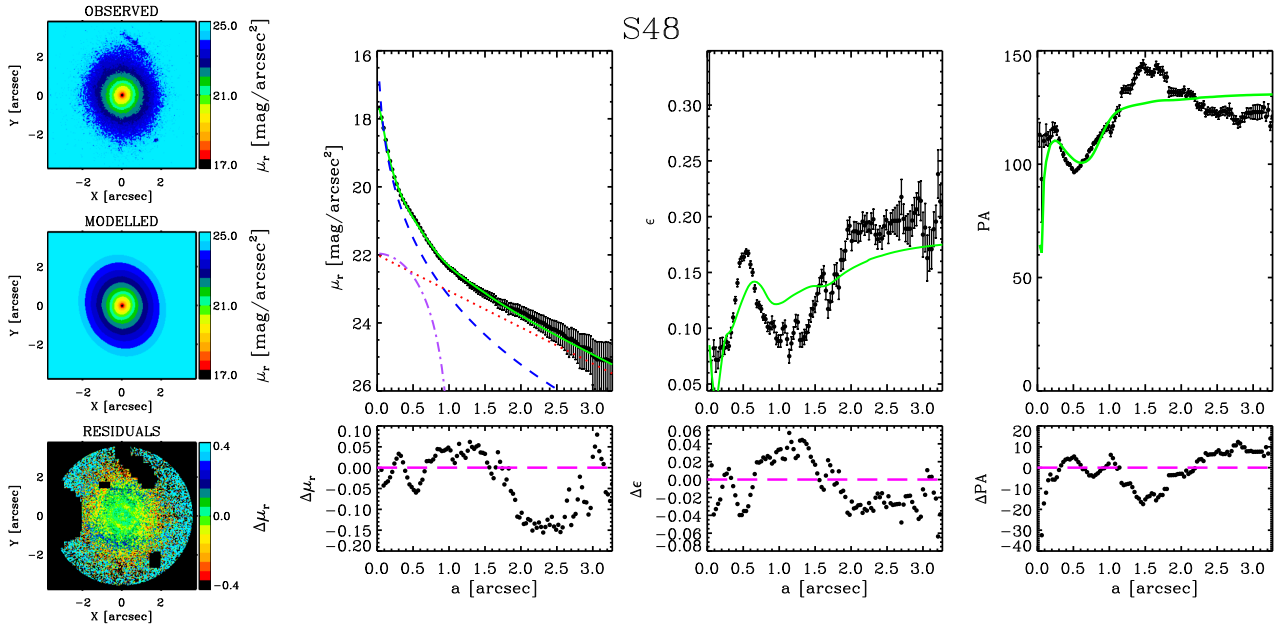**Figure A64.** As in Fig. A1 but for galaxy A11 (SeDisc model).

Table A1. Structural photometric parameters of the sample galaxies.

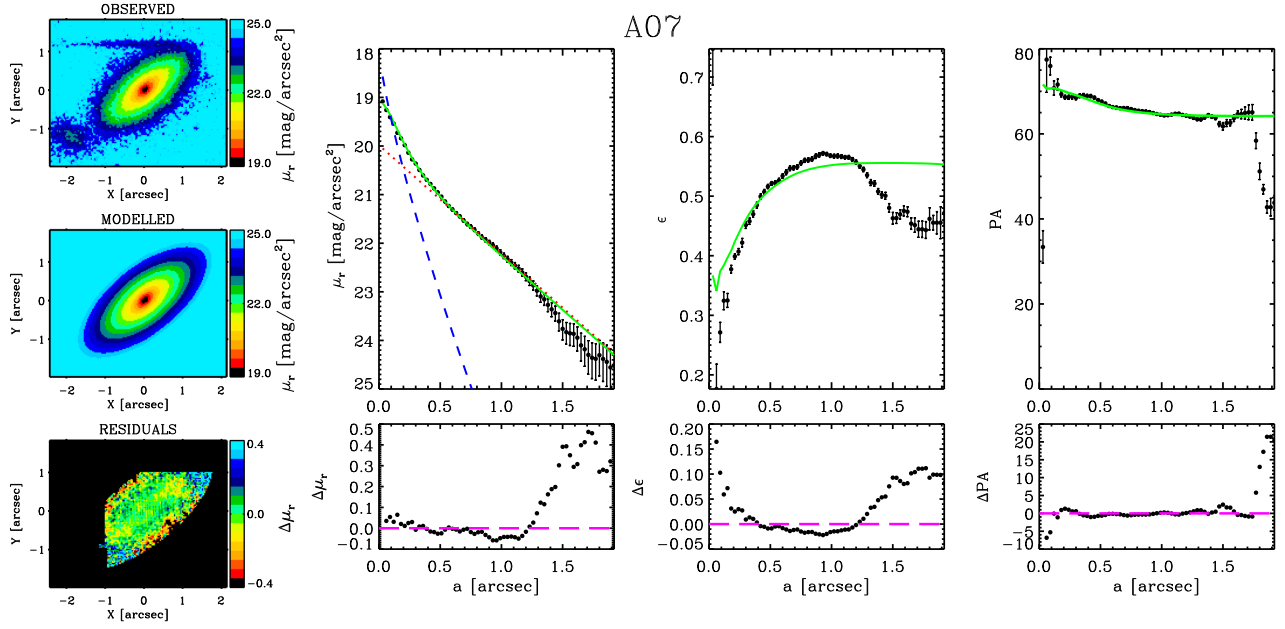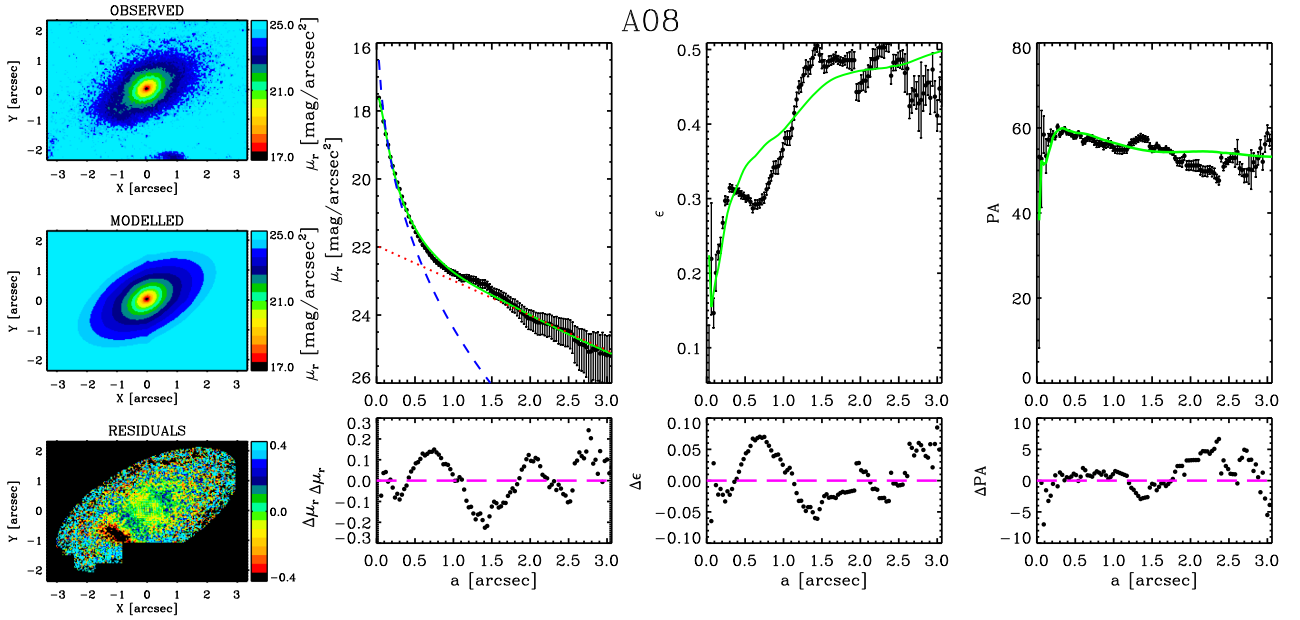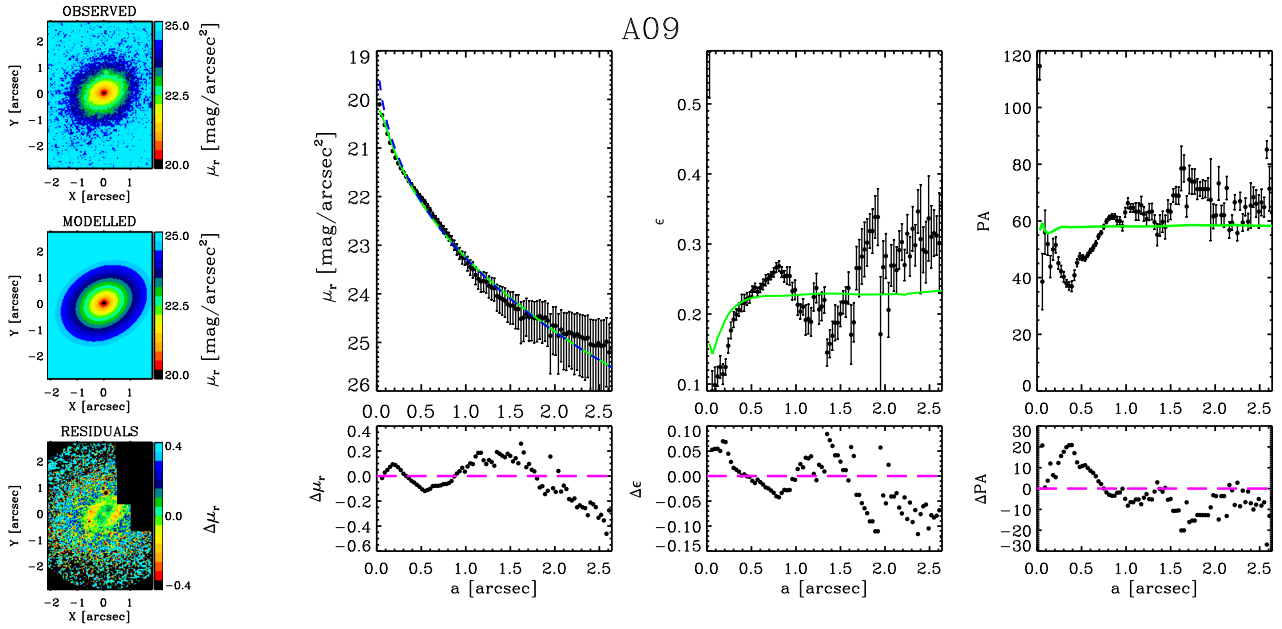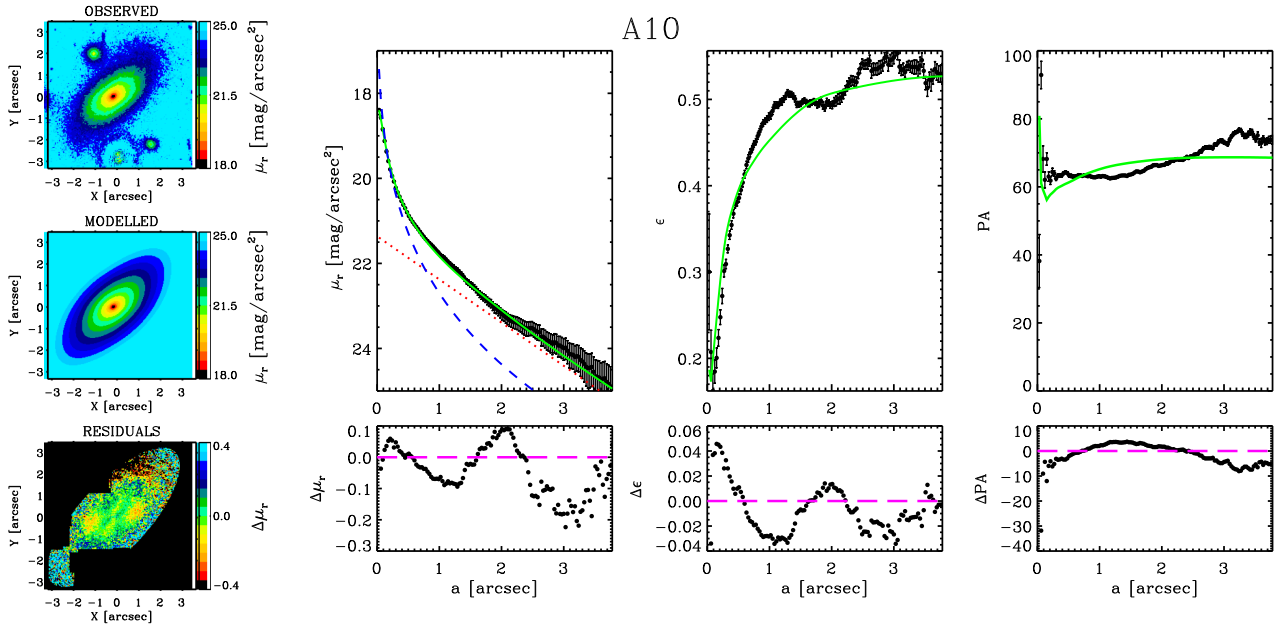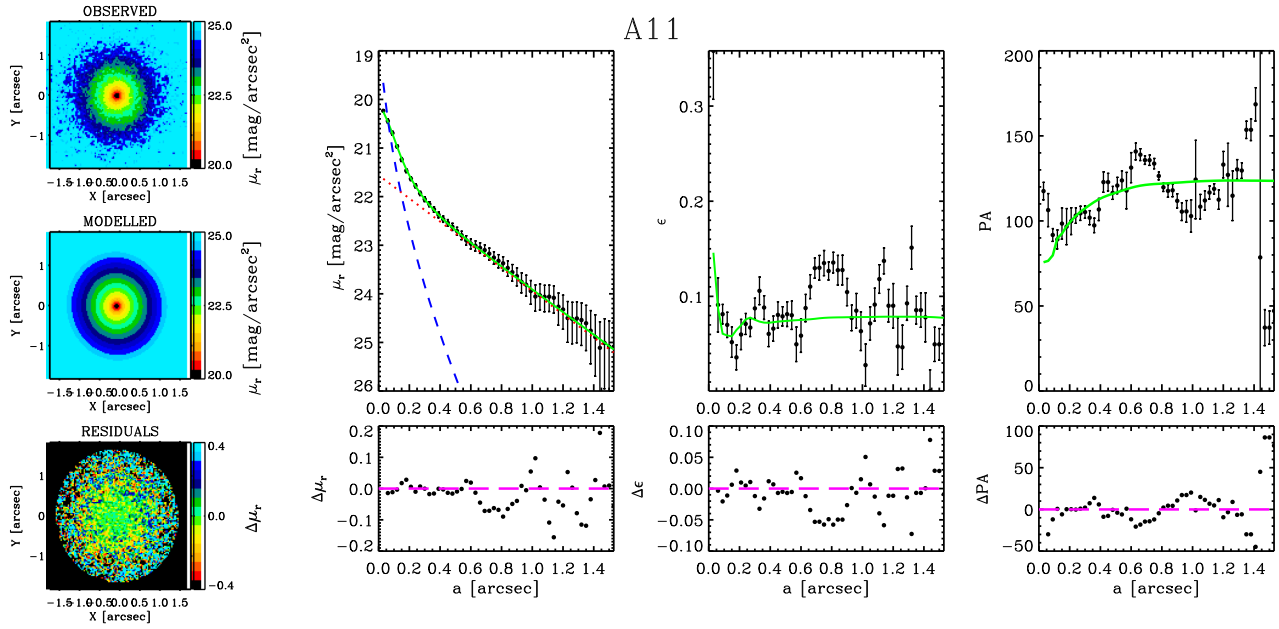| ID (1)	Model (2)	mag (mag) (3)	μ_e $\left(\frac{mag}{arcsec^2}\right)$ (4)	r_e (arcsec) (5)	n (6)	q_{bulge} (7)	PA_{bulge} (°) (8)	$\mu_{0,disc}$ $\left(\frac{mag}{arcsec^2}\right)$ (9)	h (arcsec) (10)	q_{disc} (11)	PA_{disc} (°) (12)	$\mu_{0,bar}$ $\left(\frac{mag}{arcsec^2}\right)$ (13)	r_{bar} (arcsec) (14)	q_{bar} (15)	PA_{bar} (°) (16)
								Spectroscopic sample							
S01	SeDisc	19.01	19.83 ± 0.12	0.22 ± 0.017	3.59 ± 0.12	0.71 ± 0.003	5.45 ± 0.38	20.10 ± 0.06	0.90 ± 0.019	0.34 ± 0.009	3.18 ± 0.27	–	–	–	–
S02	SeDisc	18.77	18.22 ± 0.12	0.13 ± 0.010	1.28 ± 0.04	0.76 ± 0.003	147.28 ± 0.38	19.36 ± 0.06	0.73 ± 0.015	0.37 ± 0.009	160.10 ± 0.27	–	–	–	–
S03	SeDiBar	17.54	20.55 ± 0.12	0.50 ± 0.037	1.45 ± 0.07	0.73 ± 0.002	117.68 ± 0.38	21.59 ± 0.05	2.26 ± 0.033	0.95 ± 0.006	135.12 ± 0.47	21.59 ± 0.05	4.62 ± 0.069	0.26 ± 0.006	101.82 ± 0.47
S04	Sérsic	18.88	24.92 ± 0.05	2.94 ± 0.069	10.21 ± 0.11	0.85 ± 0.001	20.64 ± 0.12	–	–	–	–	–	–	–	–
S05	Sérsic	18.71	21.62 ± 0.05	0.92 ± 0.022	3.93 ± 0.04	0.76 ± 0.001	36.11 ± 0.12	–	–	–	–	–	–	–	–
S06	Sérsic	18.74	20.46 ± 0.05	0.62 ± 0.015	3.06 ± 0.03	0.64 ± 0.001	81.61 ± 0.12	–	–	–	–	–	–	–	–
S07	SeDisc	20.10	21.33 ± 0.09	0.36 ± 0.020	1.11 ± 0.04	0.38 ± 0.004	129.93 ± 0.47	21.37 ± 0.05	1.13 ± 0.021	0.32 ± 0.008	129.38 ± 0.51	–	–	–	–
S08	SeDisc	18.79	20.31 ± 0.12	0.36 ± 0.027	3.21 ± 0.11	0.78 ± 0.003	104.17 ± 0.38	21.63 ± 0.06	1.10 ± 0.023	0.88 ± 0.009	153.04 ± 0.27	–	–	–	–
S09	SeDisc	18.53	21.37 ± 0.12	0.64 ± 0.049	5.62 ± 0.19	0.79 ± 0.003	63.50 ± 0.38	22.61 ± 0.06	1.73 ± 0.036	0.86 ± 0.009	147.45 ± 0.27	–	–	–	–
S10	SeDisc	18.11	18.95 ± 0.10	0.24 ± 0.013	2.05 ± 0.06	0.97 ± 0.002	132.62 ± 0.28	20.52 ± 0.05	0.96 ± 0.014	0.93 ± 0.006	126.46 ± 0.47	–	–	–	–
S11	SeDisc	19.23	19.17 ± 0.07	0.13 ± 0.004	3.05 ± 0.12	0.87 ± 0.004	129.27 ± 0.57	19.49 ± 0.01	0.67 ± 0.002	0.33 ± 0.001	119.78 ± 0.12	–	–	–	–
S12	SeDiBar	18.28	19.76 ± 0.12	0.26 ± 0.020	2.18 ± 0.11	0.91 ± 0.002	146.62 ± 0.28	21.50 ± 0.05	1.43 ± 0.021	0.96 ± 0.006	141.21 ± 0.47	22.45 ± 0.05	3.78 ± 0.056	0.35 ± 0.006	87.04 ± 0.47
S13	SeDisc	18.65	20.18 ± 0.12	0.39 ± 0.029	2.71 ± 0.09	0.54 ± 0.003	129.33 ± 0.38	20.35 ± 0.06	0.92 ± 0.019	0.57 ± 0.009	141.66 ± 0.27	–	–	–	–
S14	SeDisc	18.88	19.33 ± 0.12	0.23 ± 0.018	2.44 ± 0.08	0.89 ± 0.003	93.02 ± 0.38	21.81 ± 0.06	1.08 ± 0.023	0.88 ± 0.009	102.83 ± 0.27	–	–	–	–
S15	SeDiBar	19.65	18.95 ± 0.11	0.09 ± 0.007	1.52 ± 0.09	0.76 ± 0.004	15.53 ± 0.47	20.85 ± 0.05	0.76 ± 0.014	0.60 ± 0.008	25.32 ± 0.52	21.29 ± 0.05	1.32 ± 0.025	0.32 ± 0.008	43.58 ± 0.52
S16	SeDisc	18.39	20.50 ± 0.10	0.47 ± 0.026	2.74 ± 0.08	0.75 ± 0.002	116.49 ± 0.28	21.35 ± 0.05	1.23 ± 0.018	0.87 ± 0.006	35.48 ± 0.47	–	–	–	–
S18	SeDisc	15.82	21.63 ± 0.00	2.52 ± 0.014	0.96 ± 0.01	0.83 ± 0.001	157.06 ± 0.17	22.40 ± 0.03	7.70 ± 0.169	0.81 ± 0.002	152.35 ± 0.26	–	–	–	–
S19	SeDisc	19.50	19.12 ± 0.12	0.15 ± 0.011	2.08 ± 0.07	0.87 ± 0.003	79.39 ± 0.38	20.81 ± 0.06	0.60 ± 0.013	0.81 ± 0.009	98.27 ± 0.27	–	–	–	–
S20	SeDiBar	19.75	18.80 ± 0.11	0.09 ± 0.006	1.07 ± 0.06	0.70 ± 0.004	7.80 ± 0.47	20.38 ± 0.05	0.63 ± 0.012	0.52 ± 0.008	5.31 ± 0.52	21.60 ± 0.05	1.20 ± 0.023	0.50 ± 0.008	136.78 ± 0.52
S21	SeDiBar	18.42	19.11 ± 0.12	0.14 ± 0.011	1.27 ± 0.06	0.82 ± 0.002	154.07 ± 0.28	20.36 ± 0.05	1.04 ± 0.015	0.67 ± 0.006	46.45 ± 0.47	21.83 ± 0.05	3.09 ± 0.046	0.31 ± 0.006	74.02 ± 0.47
S22	SeDisc	18.63	19.66 ± 0.12	0.30 ± 0.023	2.61 ± 0.09	0.91 ± 0.003	16.50 ± 0.38	21.48 ± 0.06	1.15 ± 0.024	0.69 ± 0.009	21.69 ± 0.27	–	–	–	–
S23	SeDisc	19.55	19.66 ± 0.09	0.26 ± 0.014	2.15 ± 0.07	0.60 ± 0.004	60.44 ± 0.47	21.04 ± 0.05	0.67 ± 0.013	0.54 ± 0.008	29.34 ± 0.51	–	–	–	–
S24	SeDisc	18.38	19.82 ± 0.10	0.29 ± 0.016	2.01 ± 0.06	0.93 ± 0.002	121.71 ± 0.28	20.34 ± 0.05	0.85 ± 0.013	0.87 ± 0.006	122.38 ± 0.47	–	–	–	–
S25	SeDiBar	18.82	21.42 ± 0.15	0.50 ± 0.051	5.32 ± 0.31	0.92 ± 0.003	13.49 ± 0.38	21.78 ± 0.06	1.09 ± 0.023	0.80 ± 0.009	159.84 ± 0.27	21.06 ± 0.06	1.17 ± 0.025	0.44 ± 0.009	25.24 ± 0.27
S26	SeDisc	18.81	19.78 ± 0.12	0.33 ± 0.025	2.61 ± 0.09	0.80 ± 0.003	52.62 ± 0.38	20.65 ± 0.06	0.69 ± 0.014	0.66 ± 0.009	54.01 ± 0.27	–	–	–	–
S27	Sérsic	17.72	24.27 ± 0.04	4.03 ± 0.092	6.79 ± 0.06	0.88 ± 0.001	66.02 ± 0.09	–	–	–	–	–	–	–	–
S28	Sérsic	17.29	21.28 ± 0.03	1.72 ± 0.026	2.13 ± 0.01	0.80 ± 0.000	144.20 ± 0.06	–	–	–	–	–	–	–	–
S29	SeDisc	19.48	19.46 ± 0.12	0.11 ± 0.008	2.57 ± 0.09	0.86 ± 0.003	106.13 ± 0.38	20.11 ± 0.06	0.69 ± 0.015	0.48 ± 0.009	24.19 ± 0.27	–	–	–	–
S30	SeDisc	18.74	20.90 ± 0.12	0.58 ± 0.044	3.81 ± 0.13	0.83 ± 0.003	91.84 ± 0.38	22.22 ± 0.06	1.02 ± 0.021	0.65 ± 0.009	82.89 ± 0.27	–	–	–	–
S31	Sérsic	18.38	22.17 ± 0.04	1.38 ± 0.032	4.36 ± 0.04	0.73 ± 0.001	174.35 ± 0.09	–	–	–	–	–	–	–	–
S32	SeDisc	19.39	19.70 ± 0.12	0.22 ± 0.017	1.13 ± 0.04	0.77 ± 0.003	94.29 ± 0.38	21.41 ± 0.06	1.09 ± 0.023	0.56 ± 0.009	75.04 ± 0.27	–	–	–	–
S33	SeDisc	18.03	19.20 ± 0.10	0.27 ± 0.015	2.01 ± 0.06	0.92 ± 0.002	160.54 ± 0.28	20.63 ± 0.05	1.10 ± 0.016	0.92 ± 0.006	99.91 ± 0.47	–	–	–	–
S34	SeDisc	16.77	21.15 ± 0.06	1.57 ± 0.057	3.73 ± 0.06	0.73 ± 0.001	97.05 ± 0.19	21.98 ± 0.05	3.54 ± 0.082	0.47 ± 0.009	89.18 ± 0.36	–	–	–	–
S35	SeDisc	20.50	21.52 ± 0.09	0.35 ± 0.019	3.41 ± 0.12	0.51 ± 0.004	75.34 ± 0.47	21.42 ± 0.05	0.52 ± 0.010	0.66 ± 0.008	69.32 ± 0.51	–	–	–	–

Table A1 – *continued*

ID (1)	Model (2)	mag (mag) (3)	μ_e ($\frac{mag}{arcsec^2}$) (4)	r_e (arcsec) (5)	n (6)	q_{bulge} (7)	PA_{bulge} (°) (8)	$\mu_{0,disc}$ ($\frac{mag}{arcsec^2}$) (9)	h (arcsec) (10)	q_{disc} (11)	PA_{disc} (°) (12)	$\mu_{0,bar}$ ($\frac{mag}{arcsec^2}$) (13)	r_{bar} (arcsec) (14)	q_{bar} (15)	PA_{bar} (°) (16)
S36	SeDisc	16.90	21.35 ± 0.06	1.41 ± 0.051	3.89 ± 0.07	0.77 ± 0.001	58.05 ± 0.19	22.60 ± 0.06	5.23 ± 0.122	0.47 ± 0.009	49.10 ± 0.36	...	—	—	—
S37	SeDiBar	18.19	21.74 ± 0.12	0.41 ± 0.030	3.71 ± 0.18	0.70 ± 0.002	152.99 ± 0.28	20.63 ± 0.05	1.76 ± 0.026	0.32 ± 0.006	107.62 ± 0.47	19.76 ± 0.05	2.06 ± 0.031	0.28 ± 0.006	125.65 ± 0.47
S38	SeDisc	19.47	20.91 ± 0.12	0.39 ± 0.030	3.05 ± 0.11	0.72 ± 0.003	107.05 ± 0.38	20.43 ± 0.06	0.86 ± 0.018	0.21 ± 0.009	117.22 ± 0.27	...	—	—	—
S39	SeDiBar	18.74	20.26 ± 0.15	0.44 ± 0.045	2.25 ± 0.13	0.66 ± 0.003	177.61 ± 0.38	21.60 ± 0.06	1.19 ± 0.025	0.65 ± 0.009	171.71 ± 0.27	20.63 ± 0.06	0.86 ± 0.018	0.44 ± 0.009	63.01 ± 0.27
S40	SeDisc	19.62	18.69 ± 0.02	0.11 ± 0.001	1.97 ± 0.03	0.70 ± 0.003	106.99 ± 0.47	20.40 ± 0.01	0.58 ± 0.003	0.64 ± 0.002	103.54 ± 0.24	...	—	—	—
S41	SeDisc	18.27	19.81 ± 0.10	0.36 ± 0.020	1.93 ± 0.06	0.68 ± 0.002	150.16 ± 0.28	19.95 ± 0.05	1.21 ± 0.018	0.34 ± 0.006	145.07 ± 0.47	...	—	—	—
S42	SeDisc	18.52	17.01 ± 0.07	0.04 ± 0.001	9.93 ± 0.39	0.35 ± 0.004	78.42 ± 0.57	20.39 ± 0.01	0.98 ± 0.003	0.86 ± 0.001	110.87 ± 0.12	...	—	—	—
S43	SeDiBar	19.68	18.70 ± 0.11	0.08 ± 0.006	0.50 ± 0.03	0.75 ± 0.004	99.52 ± 0.47	20.55 ± 0.05	0.56 ± 0.011	0.96 ± 0.008	43.90 ± 0.52	21.63 ± 0.05	1.18 ± 0.022	0.25 ± 0.008	65.39 ± 0.52
S44	SeDisc	19.06	18.34 ± 0.12	0.13 ± 0.010	1.69 ± 0.06	0.78 ± 0.003	126.51 ± 0.38	19.96 ± 0.06	0.61 ± 0.013	0.61 ± 0.009	149.46 ± 0.27	...	—	—	—
S45	SeDisc	19.14	21.10 ± 0.12	0.41 ± 0.031	2.74 ± 0.09	0.69 ± 0.003	77.11 ± 0.38	20.47 ± 0.06	1.05 ± 0.022	0.32 ± 0.009	84.92 ± 0.27	...	—	—	—
S46	SeDisc	18.68	18.86 ± 0.12	0.24 ± 0.019	1.63 ± 0.06	0.62 ± 0.003	123.56 ± 0.38	20.53 ± 0.06	0.94 ± 0.020	0.53 ± 0.009	121.53 ± 0.27	...	—	—	—
S47	SeDisc	19.58	21.90 ± 0.09	0.49 ± 0.026	4.07 ± 0.14	0.87 ± 0.004	134.40 ± 0.47	21.79 ± 0.05	0.76 ± 0.014	0.94 ± 0.008	67.34 ± 0.51	...	—	—	—
S48	SeDiBar	19.14	20.79 ± 0.15	0.36 ± 0.037	4.12 ± 0.24	0.89 ± 0.003	114.25 ± 0.38	22.00 ± 0.06	1.02 ± 0.021	0.79 ± 0.009	133.57 ± 0.27	21.96 ± 0.06	1.09 ± 0.023	0.64 ± 0.009	85.30 ± 0.27
S49	SeDisc	17.39	19.98 ± 0.06	0.50 ± 0.018	2.72 ± 0.05	0.95 ± 0.001	0.73 ± 0.19	20.77 ± 0.06	1.55 ± 0.036	0.88 ± 0.009	141.83 ± 0.36	...	—	—	—
S50	SeDiBar	19.43	18.92 ± 0.15	0.10 ± 0.011	1.98 ± 0.12	0.93 ± 0.003	60.03 ± 0.38	20.78 ± 0.06	0.67 ± 0.014	0.77 ± 0.009	9.30 ± 0.27	21.59 ± 0.06	1.26 ± 0.026	0.61 ± 0.009	38.02 ± 0.27
S51	SeDisc	19.21	22.11 ± 0.12	0.66 ± 0.050	7.62 ± 0.26	0.82 ± 0.003	33.77 ± 0.38	22.63 ± 0.06	1.20 ± 0.025	0.62 ± 0.009	115.75 ± 0.27	...	—	—	—
S52	SeDisc	19.11	17.75 ± 0.07	0.08 ± 0.003	1.57 ± 0.06	0.93 ± 0.004	93.39 ± 0.57	19.52 ± 0.01	0.41 ± 0.001	0.93 ± 0.001	75.64 ± 0.12	...	—	—	—
S53	SeDisc	17.27	20.87 ± 0.06	0.68 ± 0.025	3.97 ± 0.07	0.82 ± 0.001	51.20 ± 0.19	20.71 ± 0.06	1.87 ± 0.044	0.74 ± 0.009	1.38 ± 0.36	...	—	—	—
S54	SeDisc	17.76	20.03 ± 0.10	0.50 ± 0.028	1.49 ± 0.04	0.80 ± 0.002	164.95 ± 0.28	21.13 ± 0.05	1.59 ± 0.024	0.91 ± 0.006	130.19 ± 0.47	...	—	—	—
							Ancillary sample								
A01	SeDisc	17.90	20.28 ± 0.10	0.22 ± 0.012	0.80 ± 0.02	1.00 ± 0.002	115.12 ± 0.28	20.00 ± 0.05	1.05 ± 0.016	0.94 ± 0.006	40.83 ± 0.47	...	...	...	...
A02	SeDisc	18.51	18.82 ± 0.12	0.17 ± 0.013	1.84 ± 0.06	0.91 ± 0.003	25.88 ± 0.38	19.84 ± 0.06	0.68 ± 0.014	0.81 ± 0.009	39.06 ± 0.27	...	...	...	...
A03	SeDisc	19.70	20.69 ± 0.09	0.33 ± 0.018	3.06 ± 0.11	0.70 ± 0.004	164.59 ± 0.47	20.87 ± 0.05	0.48 ± 0.009	0.82 ± 0.008	96.97 ± 0.51	...	...	...	...
A04	SeDisc	19.22	18.84 ± 0.07	0.11 ± 0.003	1.84 ± 0.07	0.67 ± 0.004	119.12 ± 0.57	19.91 ± 0.01	0.78 ± 0.003	0.40 ± 0.001	114.58 ± 0.12	...	...	...	...
A05	Sérsic	19.62	22.92 ± 0.02	1.57 ± 0.013	2.29 ± 0.02	0.49 ± 0.001	100.25 ± 0.15	—	—	—	—	...	...	...	...
A06	SeDisc	19.33	18.41 ± 0.07	0.12 ± 0.004	2.66 ± 0.10	0.81 ± 0.004	133.35 ± 0.57	20.48 ± 0.01	0.52 ± 0.002	0.90 ± 0.001	101.06 ± 0.12	...	...	...	...
A07	SeDisc	20.28	20.44 ± 0.09	0.20 ± 0.011	1.29 ± 0.04	0.46 ± 0.004	72.81 ± 0.47	19.98 ± 0.05	0.49 ± 0.009	0.41 ± 0.008	64.09 ± 0.51	...	...	...	...
A08	SeDisc	19.80	19.10 ± 0.09	0.16 ± 0.009	2.96 ± 0.10	0.61 ± 0.004	60.99 ± 0.47	21.96 ± 0.05	1.06 ± 0.020	0.46 ± 0.008	53.08 ± 0.51	...	...	...	...
A09	Sérsic	20.37	23.58 ± 0.02	1.18 ± 0.010	2.58 ± 0.02	0.76 ± 0.001	58.05 ± 0.15	—	—	—	—	...	...	...	...
A10	SeDisc	19.31	22.14 ± 0.12	0.77 ± 0.059	4.19 ± 0.14	0.58 ± 0.003	58.38 ± 0.38	21.36 ± 0.06	1.07 ± 0.023	0.38 ± 0.009	72.36 ± 0.27	...	...	...	...
A11	SeDisc	21.19	21.62 ± 0.19	0.13 ± 0.017	1.84 ± 0.22	0.88 ± 0.013	99.74 ± 3.63	21.56 ± 0.06	0.46 ± 0.010	0.92 ± 0.006	124.17 ± 1.80	...	...	...	...

Note. Best-fitting observed parameters of the sample galaxies resulting from the photometric decomposition. Column (1): galaxy ID. Column (2): fit-type according to morphological classification (see Table 3). Column (3): total magnitude. Columns (4)–(8): bulge parameters, i.e. effective surface brightness μ_e and radius r_e, Sérsic index n, axis ratio q_{bulge}, and position angle PA_{bulge}. Columns (9)–(12): disc parameters, i.e. central surface brightness μ_0, scalelength h, axis ratio q_{disc}, and position angle PA_{disc}. Columns (13)–(16): bar parameters, i.e. central surface brightness $\mu_{0,bar}$, bar radius r_{bar}, axis ratio q_{bar}, and position angle PA_{bar}. The PA are measured counterclockwise from north to east.

Table A2. Structural photometric parameters of the ETGs spectroscopic sample fitted with a `deVauc` model.

Galaxy ID (1)	mag (mag) (2)	μ_e (mag/arcsec^2) (3)	r_e (arcsec) (4)	q_{bulge} (5)	PA$_{bulge}$ ($°$) (6)
S02	18.59	21.04 ± 0.01	0.98 ± 0.007	0.44 ± 0.001	159.34 ± 0.11
S04	19.57	21.79 ± 0.01	0.63 ± 0.005	0.86 ± 0.002	19.01 ± 0.14
S05	18.71	21.65 ± 0.01	0.94 ± 0.006	0.76 ± 0.001	36.11 ± 0.11
S06	18.65	20.85 ± 0.01	0.72 ± 0.005	0.64 ± 0.001	81.89 ± 0.11
S07	19.59	24.24 ± 0.01	3.10 ± 0.027	0.33 ± 0.002	129.97 ± 0.14
S08	18.76	21.80 ± 0.01	0.92 ± 0.006	0.85 ± 0.001	109.79 ± 0.11
S09	18.69	21.88 ± 0.01	0.99 ± 0.007	0.85 ± 0.001	63.68 ± 0.11
S10	18.02	21.16 ± 0.01	0.92 ± 0.005	0.95 ± 0.001	125.60 ± 0.06
S11	19.02	21.44 ± 0.01	0.99 ± 0.007	0.41 ± 0.001	119.99 ± 0.11
S14	18.95	20.79 ± 0.01	0.52 ± 0.003	0.90 ± 0.001	93.01 ± 0.11
S16	18.24	22.27 ± 0.01	1.42 ± 0.008	0.89 ± 0.001	111.74 ± 0.06
S17	19.12	20.12 ± 0.01	0.51 ± 0.003	0.43 ± 0.001	59.14 ± 0.11
S18	15.23	24.92 ± 0.19	20.05 ± 2.033	0.82 ± 0.001	153.36 ± 0.08
S19	19.43	21.17 ± 0.01	0.51 ± 0.003	0.85 ± 0.001	90.00 ± 0.11
S20	19.42	22.64 ± 0.01	1.17 ± 0.008	0.62 ± 0.001	178.19 ± 0.11
S22	18.61	21.03 ± 0.01	0.70 ± 0.005	0.84 ± 0.001	17.20 ± 0.11
S23	19.42	21.07 ± 0.01	0.57 ± 0.004	0.63 ± 0.001	49.23 ± 0.11
S24	18.14	21.99 ± 0.01	1.30 ± 0.008	0.90 ± 0.001	115.12 ± 0.06
S25	18.83	21.80 ± 0.01	0.90 ± 0.006	0.84 ± 0.001	12.57 ± 0.11
S26	18.64	20.98 ± 0.01	0.71 ± 0.005	0.75 ± 0.001	53.86 ± 0.11
S27	18.17	22.55 ± 0.01	1.68 ± 0.010	0.89 ± 0.001	69.72 ± 0.06
S28	17.00	22.50 ± 0.01	2.97 ± 0.020	0.79 ± 0.001	143.86 ± 0.05
S30	18.68	21.31 ± 0.01	0.78 ± 0.005	0.80 ± 0.001	89.05 ± 0.11
S31	18.43	21.99 ± 0.01	1.26 ± 0.008	0.73 ± 0.001	174.21 ± 0.06
S34	16.69	21.91 ± 0.01	2.83 ± 0.019	0.67 ± 0.001	94.05 ± 0.05
S35	20.26	22.73 ± 0.01	0.86 ± 0.007	0.57 ± 0.002	73.32 ± 0.14
S36	17.00	22.24 ± 0.01	2.73 ± 0.018	0.73 ± 0.001	54.81 ± 0.05
S38	19.29	21.79 ± 0.01	1.00 ± 0.007	0.44 ± 0.001	115.63 ± 0.11
S39	18.64	21.56 ± 0.01	0.98 ± 0.007	0.68 ± 0.001	177.53 ± 0.11
S40	19.54	21.34 ± 0.01	0.59 ± 0.005	0.67 ± 0.002	104.43 ± 0.14
S41	17.92	22.01 ± 0.01	2.03 ± 0.012	0.47 ± 0.001	145.60 ± 0.06
S44	18.98	20.74 ± 0.01	0.57 ± 0.004	0.69 ± 0.001	143.60 ± 0.11
S45	18.83	22.66 ± 0.01	1.89 ± 0.013	0.43 ± 0.001	83.90 ± 0.11
S46	18.60	20.86 ± 0.01	0.78 ± 0.005	0.57 ± 0.001	122.33 ± 0.11
S47	19.40	22.87 ± 0.01	1.07 ± 0.007	0.94 ± 0.001	127.17 ± 0.11
S48	19.11	21.66 ± 0.01	0.73 ± 0.005	0.87 ± 0.001	114.89 ± 0.11
S49	17.21	21.98 ± 0.01	1.95 ± 0.013	0.93 ± 0.001	157.07 ± 0.05
S51	19.40	21.74 ± 0.01	0.62 ± 0.004	1.00 ± 0.001	41.66 ± 0.11
S52	19.01	20.62 ± 0.01	0.46 ± 0.003	0.94 ± 0.001	79.36 ± 0.11
S53	16.95	22.90 ± 0.01	3.55 ± 0.024	0.83 ± 0.001	17.19 ± 0.05
S54	17.55	22.54 ± 0.01	2.25 ± 0.013	0.87 ± 0.001	158.90 ± 0.06

Note. Best-fitting observed `deVauc` parameters. Column (1): galaxy ID. Column (2): total magnitude. Column (3): effective surface brightness. Column (4): effective radius. Column (5): axis ratio. Column (6): PA, measured counterclockwise from north to east.

Table A3. Structural photometric parameters of the ETGs spectroscopic sample fitted with a Sérsic model.

Galaxy ID (1)	mag (mag) (2)	μ_e (mag/arcsec^2) (3)	r_e (arcsec) (4)	n (5)	q_{bulge} (6)	PA$_{bulge}$ (°) (7)
S02	18.56	21.16 ± 0.05	1.03 ± 0.024	4.27 ± 0.04	0.44 ± 0.001	159.35 ± 0.12
S04	18.88	24.92 ± 0.05	2.94 ± 0.069	10.21 ± 0.11	0.85 ± 0.001	20.64 ± 0.12
S05	18.71	21.62 ± 0.05	0.92 ± 0.022	3.93 ± 0.04	0.76 ± 0.001	36.11 ± 0.12
S06	18.74	20.46 ± 0.05	0.62 ± 0.015	3.06 ± 0.03	0.64 ± 0.001	81.61 ± 0.12
S07	19.87	23.33 ± 0.02	1.94 ± 0.016	2.78 ± 0.02	0.34 ± 0.001	129.57 ± 0.15
S08	18.38	23.32 ± 0.04	1.96 ± 0.045	6.73 ± 0.06	0.84 ± 0.001	110.97 ± 0.09
S09	17.86	25.56 ± 0.04	6.09 ± 0.140	11.57 ± 0.11	0.85 ± 0.001	64.64 ± 0.09
S10	17.92	21.60 ± 0.04	1.12 ± 0.026	4.97 ± 0.05	0.95 ± 0.001	126.45 ± 0.09
S11	19.00	21.59 ± 0.05	1.07 ± 0.025	4.16 ± 0.04	0.41 ± 0.001	119.98 ± 0.12
S14	18.80	21.44 ± 0.05	0.69 ± 0.016	5.51 ± 0.06	0.90 ± 0.001	93.80 ± 0.12
S16	18.14	22.65 ± 0.04	1.71 ± 0.039	4.71 ± 0.04	0.89 ± 0.001	112.26 ± 0.09
S17	19.16	19.89 ± 0.05	0.47 ± 0.011	3.31 ± 0.03	0.43 ± 0.001	59.16 ± 0.12
S18	16.06	22.74 ± 0.02	6.01 ± 0.083	1.86 ± 0.02	0.83 ± 0.001	157.18 ± 0.07
S19	19.30	21.71 ± 0.05	0.65 ± 0.015	5.26 ± 0.05	0.84 ± 0.001	90.62 ± 0.12
S20	19.44	22.58 ± 0.05	1.14 ± 0.027	3.91 ± 0.04	0.62 ± 0.001	178.20 ± 0.12
S22	18.52	21.39 ± 0.05	0.82 ± 0.019	4.72 ± 0.05	0.84 ± 0.001	18.18 ± 0.12
S23	19.48	20.78 ± 0.05	0.50 ± 0.012	3.33 ± 0.03	0.63 ± 0.001	49.26 ± 0.12
S24	18.23	21.65 ± 0.04	1.11 ± 0.025	3.41 ± 0.03	0.90 ± 0.001	123.29 ± 0.09
S25	18.53	23.02 ± 0.05	1.62 ± 0.038	6.31 ± 0.06	0.84 ± 0.001	11.51 ± 0.12
S26	18.72	20.64 ± 0.05	0.61 ± 0.014	3.30 ± 0.03	0.75 ± 0.001	53.24 ± 0.12
S27	17.72	24.27 ± 0.04	4.03 ± 0.092	6.79 ± 0.06	0.88 ± 0.001	66.02 ± 0.09
S28	17.29	21.28 ± 0.03	1.72 ± 0.026	2.13 ± 0.01	0.80 ± 0.001	144.20 ± 0.06
S30	18.65	21.47 ± 0.05	0.84 ± 0.020	4.29 ± 0.04	0.80 ± 0.001	89.22 ± 0.12
S31	18.38	22.17 ± 0.04	1.38 ± 0.032	4.36 ± 0.04	0.73 ± 0.001	174.35 ± 0.09
S34	16.58	22.37 ± 0.03	3.54 ± 0.053	4.86 ± 0.03	0.67 ± 0.001	94.19 ± 0.06
S35	20.30	22.57 ± 0.02	0.80 ± 0.007	3.72 ± 0.03	0.58 ± 0.001	73.32 ± 0.15
S36	16.62	23.71 ± 0.03	5.76 ± 0.087	6.53 ± 0.04	0.72 ± 0.000	54.64 ± 0.06
S38	19.42	21.27 ± 0.05	0.80 ± 0.019	2.93 ± 0.03	0.44 ± 0.001	115.59 ± 0.12
S39	18.70	21.27 ± 0.05	0.86 ± 0.020	3.41 ± 0.04	0.68 ± 0.001	177.77 ± 0.12
S40	19.35	22.23 ± 0.05	0.89 ± 0.021	5.65 ± 0.06	0.66 ± 0.001	104.85 ± 0.12
S41	18.05	21.51 ± 0.04	1.59 ± 0.036	3.25 ± 0.03	0.46 ± 0.001	145.57 ± 0.09
S44	18.87	21.20 ± 0.05	0.70 ± 0.017	5.07 ± 0.05	0.68 ± 0.001	144.44 ± 0.12
S45	19.02	21.95 ± 0.05	1.35 ± 0.032	2.76 ± 0.03	0.43 ± 0.001	83.73 ± 0.12
S46	18.60	20.87 ± 0.05	0.79 ± 0.019	4.03 ± 0.04	0.57 ± 0.001	122.33 ± 0.12
S47	19.21	23.63 ± 0.05	1.57 ± 0.037	5.19 ± 0.05	0.94 ± 0.001	129.38 ± 0.12
S48	18.93	22.45 ± 0.05	1.05 ± 0.025	5.65 ± 0.06	0.87 ± 0.001	115.44 ± 0.12
S49	16.94	22.99 ± 0.03	3.25 ± 0.049	5.63 ± 0.04	0.93 ± 0.001	154.97 ± 0.06
S51	18.68	25.12 ± 0.05	3.26 ± 0.077	11.79 ± 0.12	0.92 ± 0.001	42.38 ± 0.12
S52	18.91	21.21 ± 0.05	0.59 ± 0.014	5.11 ± 0.05	0.93 ± 0.001	79.88 ± 0.12
S53	16.55	24.37 ± 0.03	7.58 ± 0.114	6.26 ± 0.04	0.83 ± 0.001	18.11 ± 0.06
S54	17.65	22.17 ± 0.04	1.87 ± 0.043	3.49 ± 0.03	0.87 ± 0.001	160.09 ± 0.09

Note. Best-fitting observed Sérsic parameters. Column (1): galaxy ID. Column (2): total magnitude. Column (3): effective surface brightness. Column (4): effective radius. Column (5): Sérsic index. Column (6): axis ratio. Column (7): PA, measured counterclockwise from north to east.

This paper has been typeset from a TeX/LaTeX file prepared by the author.